Fault Detection of Structures in the Presence of Structural Variability

by

Sabri Karabay

B.S., Middle East Technical University (1992)
Ankara, Turkey

Submitted to the Department of Mechanical Engineering
in partial fulfillment of the requirements for the degree of

Master of Science

at the

MASSACHUSETTS INSTITUTE OF TECHNOLOGY

November 1993

Author .....
Department of Mechanical Engineering
November, 1993

Certified by .....
Richard H. Lyon
Professor of Mechanical Engineering
Thesis Supervisor

Accepted by .....
Professor Ain Sonin
Chairman, Departmental Committee on Graduate Students

Eng.

Fault Detection of Structures in the Presence of Structural Variability

by

Sabri Karabay

Submitted to the Department of Mechanical Engineering
on November, 1993, in partial fulfillment of the
requirements for the degree of
Master of Science

Abstract

The transfer functions have been measured on a set of car body subassemblies in order to study the *structural variability* phenomenon and to develop a robust fault detection technique in the presence of structural variability. An experiment was designed to minimize the structural variability of the car body subassemblies. 20 subassemblies were manufactured in an extraordinarily controlled environment at the River Rouge plant of Ford Co. The 10 of the 20 subassemblies were manufactured to have seven defective spot-welds, whereas the remaining 10 were manufactured to be good.

One of the major constituents of the overall variability of nominally identical subassemblies was found to be *experimental variability.* The experimental variability and its constituents were studied and the adverse effect of the experimental variability on the transfer function measurements were discovered to be significant unless the test set-up is designed properly. Another major constituent of the overall variability was found to be the *structural variability*, which was mainly due to the small structural differences among the nominally identical subassemblies. The overall variability of the good and the bad subassemblies was measured to be fairly high as concluded by some past researchers.

Finite Element Analysis (FEA) of the subassembly was carried out to check the experimental results by comparing the calculated and measured natural modes of the subassembly. The comparison demonstrated satisfactory match between the calculated and measured natural frequencies.

Taking all the findings on experimental and structural variability into consideration, a new fault detection technique was developed to diagnose the spot-weld defect of the subassembly. The proposed recognition matrix technique was tested to differentiate the bad and the good subassemblies. The detection rate of the proposed technique was found to be 99% for the group delay.

Thesis Supervisor: Richard H. Lyon
Title: Professor of Mechanical Engineering

Acknowledgments

Thanks and praises be to the Creator and the Sustainer of the Heavens and the Earth, Allah (CC) for granting me this unique opportunity.

Many thanks to my parents Dogan Karabay and Yucel Karabay and my brother Semih for their invaluable support and patience.

Thanks to my advisor, Professor Lyon, for his helpful criticism, his patience and help throughout this work.

Thanks to Mary Toscano, who helped me a lot at keeping track of my MIT life.

Thanks to my dear friends, Sabbir Rahman, Ibrahim El Sanhouri, Ismail Kutan, Mahboub Majumdar for proof-reading my thesis and debugging the computer programs.

Finally, thanks to the Ford Alpha engineers for their financial and technical support.

Contents

List of Figures

List of Tables

Chapter 1

Introduction

1.1 Concept of Structural Fault Diagnosis

With the development of the signal processing techniques and equipment, vibration analysis has become a major tool for structural fault detection. The transmission throughout a structure of any applied excitation is governed by its structural characteristics. Correspondingly, the form of the output signal at the surface of the structure contains information about the input signal and the structure itself. Quantitatively :

$$Y(w) = H(w)X(w) \tag{1.1}$$

or equivalently,

$$y(t) = h(t) * x(t) \tag{1.2}$$

where,

X(w) : the input spectrum

Y(w) : the output spectrum

H(w) : the transfer function

x(t) : the input waveform

y(t) : the response signal

h(t) : the impulse response of the structure

A sensor mounted on the surface of a structure measures y(t), the response signal. To diagnose changes in the structure, the input waveform has to be known. Knowledge of the input waveform and the response signal allows calculation of the impulse response or the transfer function of the structure. The transfer function then provides information regarding the structure itself, –the vibration transmission path. Most fault diagnosis methods are based on the information obtained from the transfer function, especially its magnitude. Certain structural changes affect the natural frequencies of the structure and monitoring these specific frequencies reveals the type of change [13]. On the other hand, there are problems associated with this method. Transfer function measurements on nominally identical diesel engines [4] and automotive vehicles [6] have shown that the transfer function of even the nominally identical structures suffer from considerable structural variability. Consequently, any fault detection method developed on an individual structure cannot be directly applied to a group of identical structures. Rather, an understanding of the structural variability is essential for monitoring a group of identical structures.

Another research was done on fault detection of railroad wheels [19]. An acoustic signature inspection system for railroad wheels was developed. The research makes use of statistical tools to overcome structural variability and diagnose the railroad wheels. Several indicators were used to diagnose the railroad wheels such as spectral cross correlation, system resonances and modal frequencies, which was reported to give better fault detection results. The fault detection rate was found to be 45% [19].

With the prior knowledge of the transfer function $H(w)$ and the output spectrum $Y(w)$, the input spectrum $X(w)$ can be recovered in an operating structure. This recovery of the input spectrum $X(w)$ is called *inverse filtering.* Misfirings in an internal combustion engine or the leakage in the pistons of a compressor can be monitored by inverse filtering. The inverse filtering technique requires transfer function information. The resulting recovered input waveform will only be as accurate as the transfer function information itself. Thus, the existence of structural variation within a group of nominally identical structures makes the design of the inverse filters complicated. To overcome problems caused by the structural variability, a robust filter is required. A number of investigations [5,7] have been carried out in order to design such a robust inverse filter that minimizes the structural variability

problem .

Both the structural fault detection method and the inverse filtering method require a detailed understanding of the structural variability. Only then can a robust fault diagnosis method be developed.

1.2 Aim and Approach of this Research

This research concentrates mainly on structural fault detection in the presence of structural variability. The key step in our research is to understand the structural variability phenomenon and investigate its effect on structural fault detection of a group of identical structures. Once the structural variability phenomenon is understood, a robust structural fault detection method can be developed. Such robust fault detection methods can be utilized on production lines to monitor the quality of the manufactured parts.

In order to understand structural variability, 20 test pieces were tested. Since the whole Ford Mustang 1992 car body is too complex to analyze, a small portion of the car body was picked as the test piece. The test piece is shown in figures 2.2 and 2.3. The test piece is manufactured from several sheet metal parts spot-welded to each other by 80 spot-welds. In 10 of the 20 test pieces, all spot-welds were manufactured to be *good* according to the criteria of the Ford quality control organization. The other 10 test pieces were purposely manufactured to be faulty, the fault being 7 cold spot-welds. In this manner, 10 *nominally identical good* test pieces and 10 *nominally identical bad* test pieces were obtained. This configuration allowed us to study and assess the structural variability phenomenon and eventually to develop a fault detection method to monitor the spot-weld quality of the test piece.

1.3 Thesis Organization and Contents

Chapter 2 describes the experimentation technique, instrumentation and the design of the key components. Chapter 3 focuses on the structural variability phenomenon. The structural variability is shown to have two major constituents, *experimental variability* and *structural variability.* Chapter 4 elaborates on the information obtained from the examination

of the transfer function of the test piece. Chapter 5 presents the FEA of the test piece and the effects of the simulated fault on the mode shapes and natural frequencies of the test piece. Chapter 6 develops a new method to monitor the spot-weld quality in the presence of structural variability. Finally, in chapter 7 the results and general comments are presented together with suggested further research.

Chapter 2

Experimentation and Design of Test Set-up

The following experiment is designed to study the variability and fault diagnosis of a car body structure. Since the whole car body is too complex to analyze, a small portion of the Ford Mustang 1992 car body is tested.

2.1 Design of Experimentation

One of the aims of this research project is to diagnose faults, taking into consideration the inherent structural variability [1]. So the River Rouge plant of Ford Co. was visited and sample portions of the Ford Mustang car body were selected. The test piece chosen is shown in figures 2.2 and 2.3. The test piece was a front-end driver-side supporter [2] which is essentially three plates spot-welded to each other. It is part of the skeleton of the car body and has a beam-like structure to absorb impacts during a crash. All the spot-welding is done at one station by robots.

In order to calculate variability in the test pieces, 22 test pieces were manufactured. To ensure that the variability was solely due to structural variability, 20 of the 22 test pieces were welded in an extraordinarily controlled environment. Within the group of 20 test pieces, all the controllable parameters were adjusted to minimize variability as much

[1] See chapter 3 for detailed discussion.
[2] From now on, it will be referred to as the test piece.

as possible. As a result, the variability of the 20 test pieces were lower than usual. All the 20 test pieces were manufactured successively on the same day. Meanwhile, the remaining 2 test pieces were not manufactured under controlled conditions. One was manufactured in November 1992 and the other in March 1993, whereas the remaining 20 were manufactured in March 1993. Thus, the developed fault detection technique can be tested on the out-of-population test pieces to examine its effectiveness in practice.

Ten out of the 20 test pieces were manufactured to be *good*, whereas the other 10 were manufactured to be *bad*, the difference being 7 cold welds out of 80 welds done intentionally to simulate a fault. Each spot-weld has to have certain weld diameter to pass the quality test. Occasionally, incompleted spot-welds which are also called *cold welds* come out of the production line due to the fluctuations in the manufacturing parameters. Since cold welds deteriorate the integrity of the car body, they have to be diagnosed. Here, *good* implies that the test pieces passed the quality control scheme of Ford Motor Co.. Having been manufactured, the test pieces were sent to MIT to be tested. However, one of the 10 good pieces and one of the 10 bad pieces were damaged during shipping to MIT. These two test pieces were discarded.

On each test piece, there are 8 measurement points as shown in figure 2.3, *point 1* being the drive-point. Measurement points were picked to be on three major plates, one being right next to a defective weld, others were somewhat away from the defective welds.

2.2 Design of the Test Set-up

It is known that an unsatisfactory design of the test set-up leads to artificial variations in measurements [1]. Since the goal of this thesis is to diagnose structures in the presence of inherent structural variation, particular attention is paid to design elements of experimentation which could introduce further variation. A drawing of the test set-up is shown in figure 2.4. Certain elements such as the shaker and accelerometer attachment, were found to be the major source of *experimental variation* [2].

The testing of sheet metal requires a carefully designed shaker attachment. The ultimate goal is to input energy in only one direction, whilst avoiding applying a moment to the structure. In order to achieve this, a thin rod called a *stinger* is attached between the shaker and the force transducer. The stinger must be soft in the transverse direction to minimize the moment transmission. Another consideration is to carefully design the resonances of the stinger-shaker arrangement as not to interfere with the frequency range of the measurement. The dynamics of the stinger-shaker system are based on the model shown in figure 2.1, where the connection of the stinger to the shaker is at point B. As it is shown in the figure 2.1, the dynamic model takes the shaker suspension properties into account. The ultimate goal is to minimize θ, the angular rotation of the shaker due to the unwanted moment input from the structure, while providing enough strength to the stinger for it to operate. The design parameters of our shaker-stinger system are as follows : [3] .

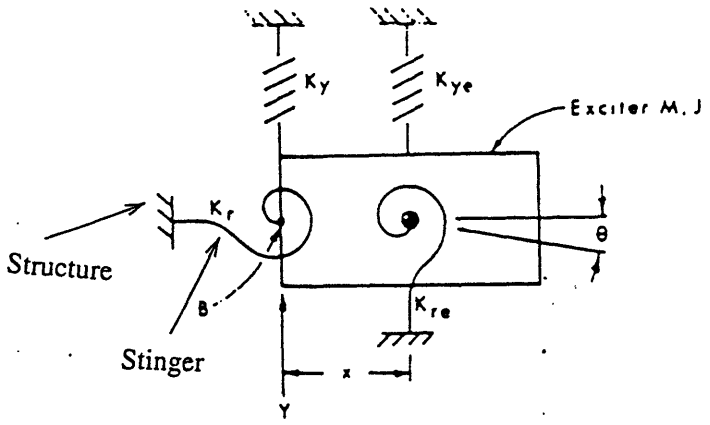

Figure 2.1 Dynamic model of the shaker-stinger system

Maximum shaker force, P = 10 N

Stinger material endurance limit, σ_e = 200 MPa

Shaker mass = 1.1 kg

Frequency range, 5 to 500 Hz

Shaker armature mass, M = 0.018 kg

[3] A detailed derivation is included in [14]

Shaker suspension K_{ye} = 1400 N/m

Modulus of elasticity, E = 200 MPa

Shaker suspension K_{re} = 0.469 Nm/rad

Lowest force to be measured, 0.05 N

Bending sensitivity of force transducer, 4 N/Nm

Stinger diameter, d

Stinger length, l

The design calculations are as follows :

Step 1 Entering the maximum shaker force and the appropriate material endurance limit, solve for the required minimum stinger diameter, d_{min} based on strength requirement.

$$\sigma_e = \frac{P}{A} \qquad A = \frac{\pi d^2}{4} \tag{2.1}$$

$$d_{min} = \sqrt{\frac{4P}{\pi \sigma_e}} \tag{2.2}$$

$$d_{min} = 0.25mm \tag{2.3}$$

Step 2 Entering this minimum stinger diameter and the maximum shaker force, solve for the maximum allowable stinger length, l_{max}. The stinger is modeled as a column with fixed ends and the following buckling equation is solved.

$$l = \sqrt{\frac{2\pi^2 EI}{P}} \qquad I = \frac{\pi d^4}{64} \tag{2.4}$$

$$l = \sqrt{\frac{2\pi^3 E d^4}{64P}} \tag{2.5}$$

$$l_{max} = 273mm \tag{2.6}$$

Step 3 Calculation of the lateral stiffness of the stinger, K_y. Refer to figure 2.1.

$$\delta = \frac{Wl^3}{12EI} \tag{2.7}$$

$$K_y = \frac{W}{\delta} \tag{2.8}$$

$$K_y = \frac{12E\pi d^4}{l^3 64} \tag{2.9}$$

$$K_y = 452500N/m \tag{2.10}$$

Step 4 Calculation of the bending stiffness of the stinger, K_τ. Refer to figure 2.1.

$$\phi = \frac{Ml}{4EI} \tag{2.11}$$

$$K_\tau = \frac{M}{\phi} \tag{2.12}$$

$$K_\tau = \frac{4E\pi d^4}{l64} \tag{2.13}$$

$$K_\tau = 0.26Nm/deg \tag{2.14}$$

$$\theta = \frac{0.0125}{0.26}\frac{Nm}{Nm/deg} = 0.04deg \tag{2.15}$$

So the shaker is allowed to rotate only *0.04* degrees [4], which should be zero for the no moment input condition.

At this point of the stinger design, a stinger diameter of 1.4mm and length of 10mm which satisfy above design requirements is chosen. These dimensions are feasible as far as the availability and machinability of the stinger material are concerned.

Step 5 The resonances of the stinger should not interfere with the frequency range of measurement. So, the first lateral bending mode of stinger, f_b is calculated to check whether it interferes with the frequency range of measurement.

[4]Refer to figure 2.1 for θ

$$K = \frac{192EI}{l^3} \qquad m = 0.39\frac{l\pi d^2\rho_w}{4} \tag{2.16}$$

$$f_b = \frac{1}{2\pi}\sqrt{\frac{K}{m}} \tag{2.17}$$

$$f_b = 61600Hz \tag{2.18}$$

where,

m is the effective mass of the resonating stinger as a clamped-clamped beam

ρ_w is the specific mass of the stinger

Step 6 For the same reasoning stated in *step 5* the axial resonant frequency of the stinger and shaker armature, f_a is calculated by entering cross-sectional area of the stinger, its length and modulus of elasticity.

$$k = \frac{A_w E_w}{l} \tag{2.19}$$

$$f_a = \frac{1}{2\pi}\sqrt{\frac{k}{M}} \tag{2.20}$$

$$f_a = 6575Hz \tag{2.21}$$

f_a and f_b are well above the maximum frequency range of interest and don't interfere with the frequency range of measurement, which is from 5 to 500 Hz. The final design parameters of the stinger are :

$$d = 1.4mm \qquad l = 10mm$$

So there are several considerations in designing the stinger ;

- providing sufficient strength to the stinger,
- minimization of the moment transmission between shaker and the structure, minimum θ requirement, [5]

[5]Refer to figure 2.1

- designing the resonances of the shaker-stinger system out of the frequency range of measurements.

Above considerations have to be taken into account in designing the shaker-stinger system in order to minimize problems initiated from the poor shaker-stinger systems. Actually, poor design is observed to increase *experimental variability* of the TF measurement, which will be demonstrated in the next chapter.

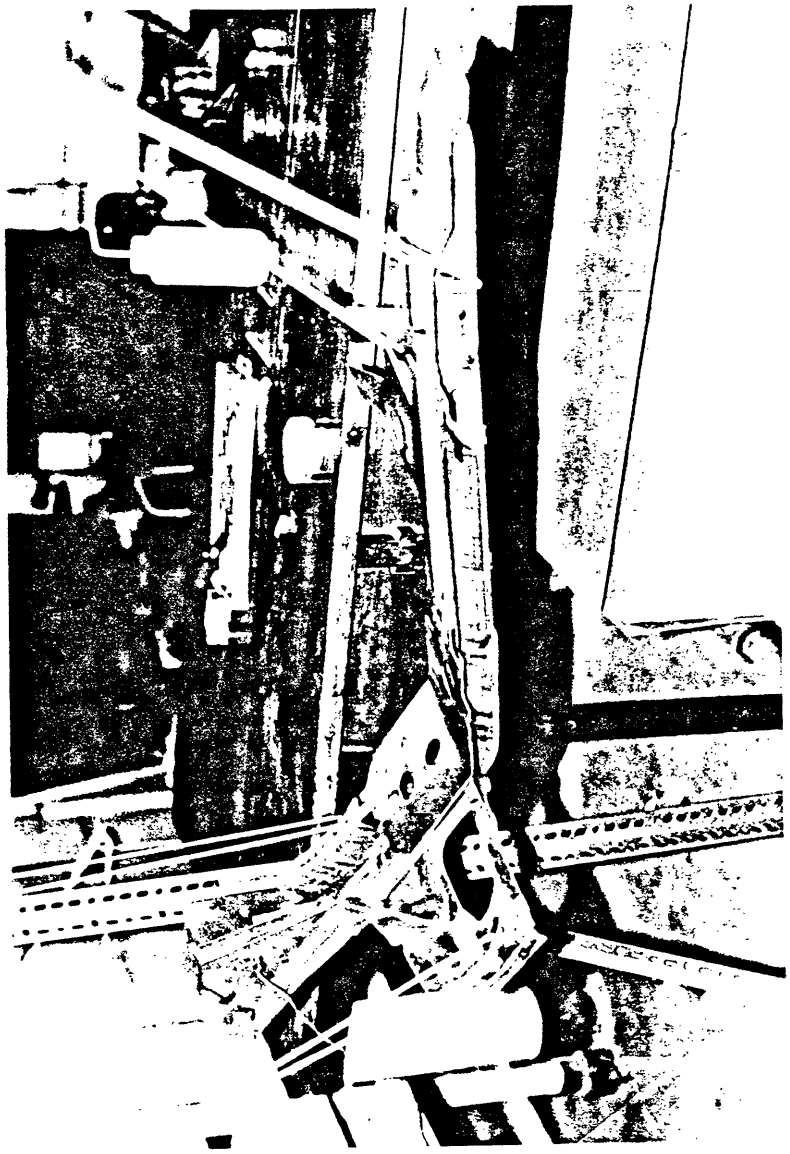

Figure 2.2 Photograph of the test piece

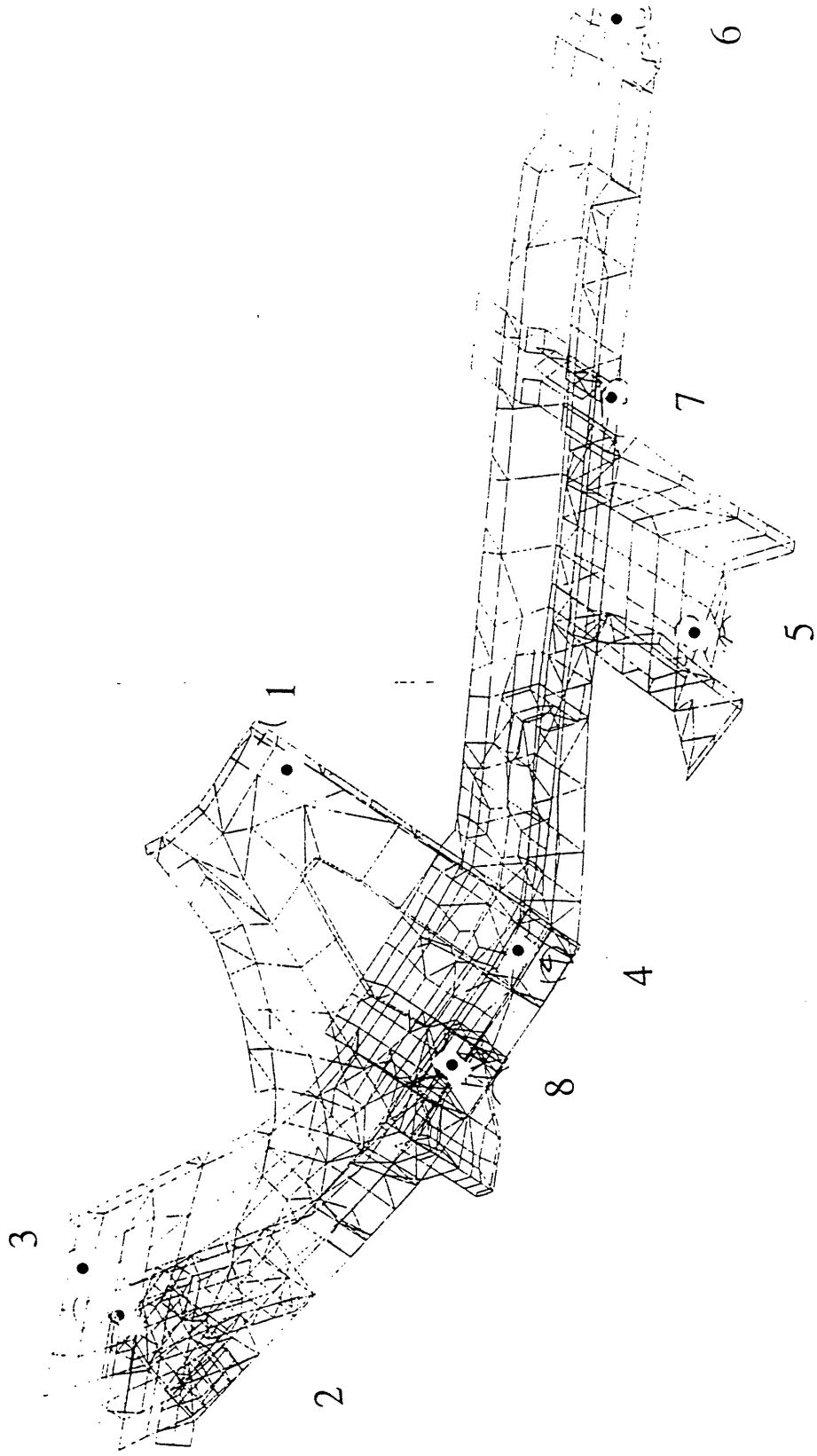

Figure 2.3 Finite Element Meshing of the test piece

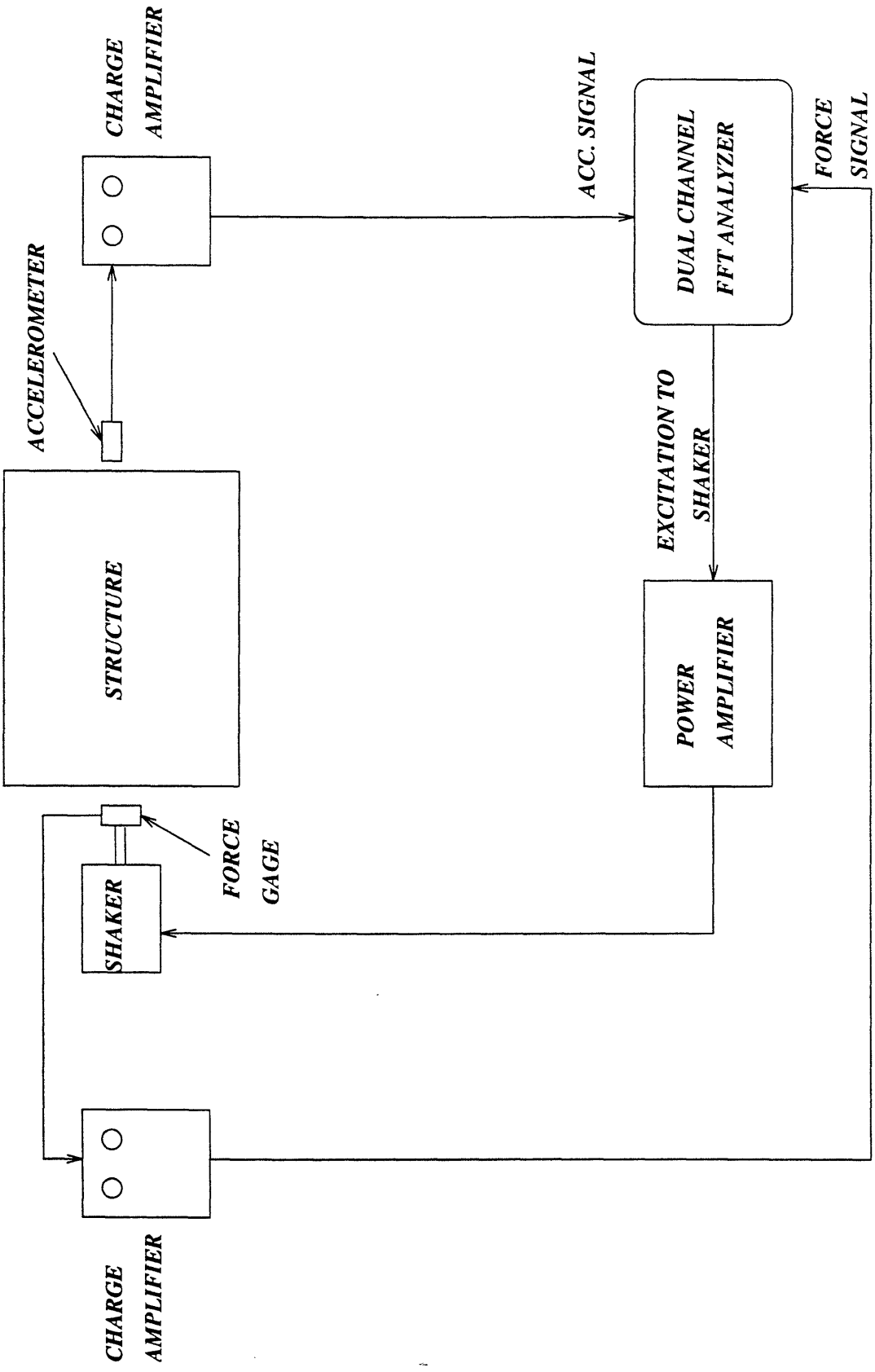

Figure 2.4 Experiment test set-up

Chapter 3

Structural Variability

Research on *inverse filtering* revealed an unexpected phenomenon, *inherent variability of nominally identical structures* [4]. Further research confirmed the same result [5,6]. The structural variability among identical structures poses a significant problem for diagnostics and inverse filtering.

3.1 Past Studies on Variability

One of the first researches on structural variability was done by Gibson [4] in 1986. In this research 50 diesel engines were tested at different stages of assembly in the production plant, as they came out of the production line. At each stage, the TF [1] of about 50 *nominally identical* diesel engines were measured. Furthermore, at each stage, the standard deviations of the TF of 50 *nominally identical* diesel engines were calculated. Figure 3.1 presents the mean ± 1 standard deviation of the TF magnitude and unwrapped phase for engine castings. Unexpectedly, the standard deviations of the TF magnitude and phase of *nominally identical* diesel engines were found to be fairly high, even reaching 8 dB at higher frequencies.

Moreover, the standard deviation of the TF became larger with increasing frequency. The standard deviations of the TF magnitude and phase were found to be high for the rest of the assembly stages, too. Gibson also did some experiments to prove that the variability is solely caused by variations in structure, not by the experiment itself. With this much variability, it is very difficult to carry out successful inverse filtering or fault diagnosis. The

[1] TF refers to transfer function

implication of the high standard deviation of nominally identical structures is that any fault diagnosis method developed on one engine may not work properly for the other engine, since both of the engines don't have exactly the same TF. Obviously, the TF variability of nominally identical structures isn't encouraging for the development of a reliable fault diagnosis technique.

Another research was done on automobiles in 1992 [6]. 99 *nominally identical* 1991 Isuzu RODEOs and 57 *nominally identical* pick-up trucks were tested and both the airborne and structure-borne TFs of the two types of vehicles were measured. Statistical variations of structural-acoustic characteristics of RODEOs and pick-up trucks were calculated from test data taken in the manufacturer's plant. The report shows larger than expected TF variations as well as the increase of the TF variation with increasing frequency. Thus, the report very well agrees with the Gibson's study and concludes that some of the measured TF variation is clearly due to the inherent structural variability.

So, the past research strongly suggests that the *nominally identical* structures have some amount of inherent TF variability. Actually, it is surprising to find such large difference among *nominally identical* structures. The reason may be the transfer function's high sensitivity to minute differences between nominally identical structures.

Moreover, the TF of a *given* structure is also reported to change under changing environmental conditions, such as temperature and loading [7,18]. Figures 3.2, 3.3, 3.4 illustrate the variability of the TF of a compressor during normal operation, cold operation and warming period. So the TF also changes within a particular structure under changing operating conditions. This variation will be referred to as *structural variability within a structure*

The variation of the TF stemming from *structural variability among nominally identical structures* is easier to explain than that from *the variability within a structure.* So-called *identical* structures are not exactly the same. They are manufactured within certain tolerance limits. Apparently, the TF seems to amplify these minute differences. As the test frequency increases, the variability increases [2]. This is because the wavelength of the in-

[2]Observe the increase of 1 standard deviation with increasing frequency in figure 3.1

put excitation gets smaller and becomes comparable to the size of the minute differences in the structure. Consequently, any minute difference induces considerable variation in the TF.

On the other hand, *variability within a structure* is not as easy to explain as the previous. Recent studies shed light onto this phenomenon. The non-minimum phase zeros of the structure are found to be very sensitive to minute changes in the operating conditions of the structure. Minute changes in operating conditions move the non-minimum phase zeros across the real frequency axis, changing the total phase by 2π [7]. To reduce *variability within a structure*, the all-pass part of the TF, which incorporates the non-minimum phase zeros, are removed. The remaining portion of the signal, the minimum phase part, has less variability due to removed non-minimum phase zeros. In some cases, it is advantageous to use the minimum phase part of the TF in order to reduce variability effects within a structure [7].

3.2 Assessment of Experimental Variability

It is also known that errors in experimentation cause variations [1]. Before starting experimentation, it must be made sure that the variation of the measured data is solely due to *structural variability*, not *experimental variability.*

The procedure to assess experimental variability due to the test set-up is to carry out preliminary experiments pertaining to the repeatability of the test set-up. In preparing the experiment set-up, TF measurements are recorded successively without stopping the instruments. The successive measurements are plotted on top of each other in figure 3.5. All recorded data lie on top of each other, exhibiting no experimental variation at all. The variation in unwrapped phase at low frequencies is due to low coherence [3] at low frequencies and the insufficiency of the *phase unwrapping algorithm.* Other than that, all three measurements have the same pattern of unwrapped phase.

The second step is to disassemble the test set-up and reassemble it and record TF mea-

[3]Refer to figures 4.25 through 4.32 to observe typical coherence recordings of the experiment

surements. Comparing the measurements before and after the disassembly, it is concluded that the experimental variability of the test set-up is negligibly small, as shown in figure 3.6. On the other hand, it is a fact that some changes in the test set-up give rise to considerable amount of experimental variation. Figure 3.7 demonstrates this idea very well. In one measurement, the shaker was tilted slightly, so slight that it was difficult to discover easily. This TF measurement is overlaid on top of properly attached shaker measurement. As shown in figure 3.7, there is considerable change in TF.

The results of the preliminary experiments show that the *experimental variation* of the test set-up is fairly low. Consequently, any variation observed in the TF measurements of the 20 test pieces should be due mainly to *structural variability* of the test pieces.

3.3 Discussion of Structural Variability in the Test Pieces

Figures 3.8 through 3.15 illustrate the mean and the *+1 standard deviation* of the 18 test pieces [4]. As concluded by the past studies [4,6,7], a considerable amount of TF variation is present. The TF variation does not seem to change from either one measurement point to the other or between good parts and bad parts. By virtue of the preliminary experiments the *experimental variation* of the test set-up is reduced to a minimum. Thus, the measured TF variation [5] is mainly due to the *inherent structural variability* of the test piece.

The standard deviation becomes larger with increasing frequency. On the other hand, the increase in standard deviation with increasing frequency is not as clear as Gibson's measurements [4], as shown in figure 3.1. This is partly due to the choice of the frequency range of measurement. Gibson went up to 3200 Hz, whereas our measurements go up to only 500 Hz. Careful investigation of figure 3.1 shows that the increase in standard deviation with increasing frequency reveals itself especially at higher frequencies. This is probably why Gibson [4] observed the phenomenon more clearly. Thus, standard deviation of our TF measurements are expected to increase more as the frequency range of measurement

[4]Recall that 2 of the 20 test pieces were discarded, since they were damaged on the way to MIT. Also the 2 out-of-population test pieces weren't included in the standard deviation calculation.

[5]Refer to figures 3.8 through 3.15

is increased. Consequently this observation indicates that the fault detection may become more difficult at higher frequencies, since the structural variability among *nominally identical* structures grows larger, leaving less opportunity for reliable fault detection.

Having manufactured *nominally identical* good test pieces and *nominally identical* bad test pieces, it is worthwhile to assess the effect of the fault [6] on the standard deviation of the TF measurement. When comparing the TF standard deviation of the good and bad test pieces at each measurement point [7], no significant change in TF standard deviation of the good and bad test pieces is observed. This comparison suggests that the fault didn't change the overall standard deviation level of the TF measurements.

On the other hand, the fault may change the TF magnitude or the TF standard deviation at certain frequencies. Reviewing the figures 3.8 through 3.15 once more, no such change in either TF magnitude or TF standard deviation is noticed. Although there is difference in TF magnitude and its standard deviation between the good and the bad test piece for the same measurement point, there is no clear trend in the TF magnitude and/or the TF standard deviation that will lead to the detection of the fault. As it will be explained in chapter 5, the Finite Element Analysis of the good and bad test piece helped us identify the effects of the fault on the TF measurements. The reason for not identifying the change in TF mesurements due to the fault in figures 3.8 through 3.15 will be discussed in chapter 5.

Another interesting point is the peak at 75 Hz which appears in all TF measurements, regardless of the soundness of the test piece. This peak corresponds to the first global mode of the structure as it is explained in Chapter 5. Since it is a dominant global mode, it appears in all TF measurements and doesn't get affected by the fault very much.

The presence of structural variability of this magnitude, at some frequencies as high as 5 dB, is discouraging for fault diagnosis purposes. Because any successful method has to differentiate the good from the bad in the presence of structural variability. If the fault

[6] Recall that the fault is a minute structural defect in our experiment, 7 cold welds out of 80 spot-welds. Refer to section 2.1 for further details on the explanation of cold weld

[7] Refer to figures 3.8 through 3.15

under consideration is composed of minute changes in the structure, such as several faulty welds, the problem becomes even more challenging, since the high structural variability is more likely to suppress the fault signature in TF.

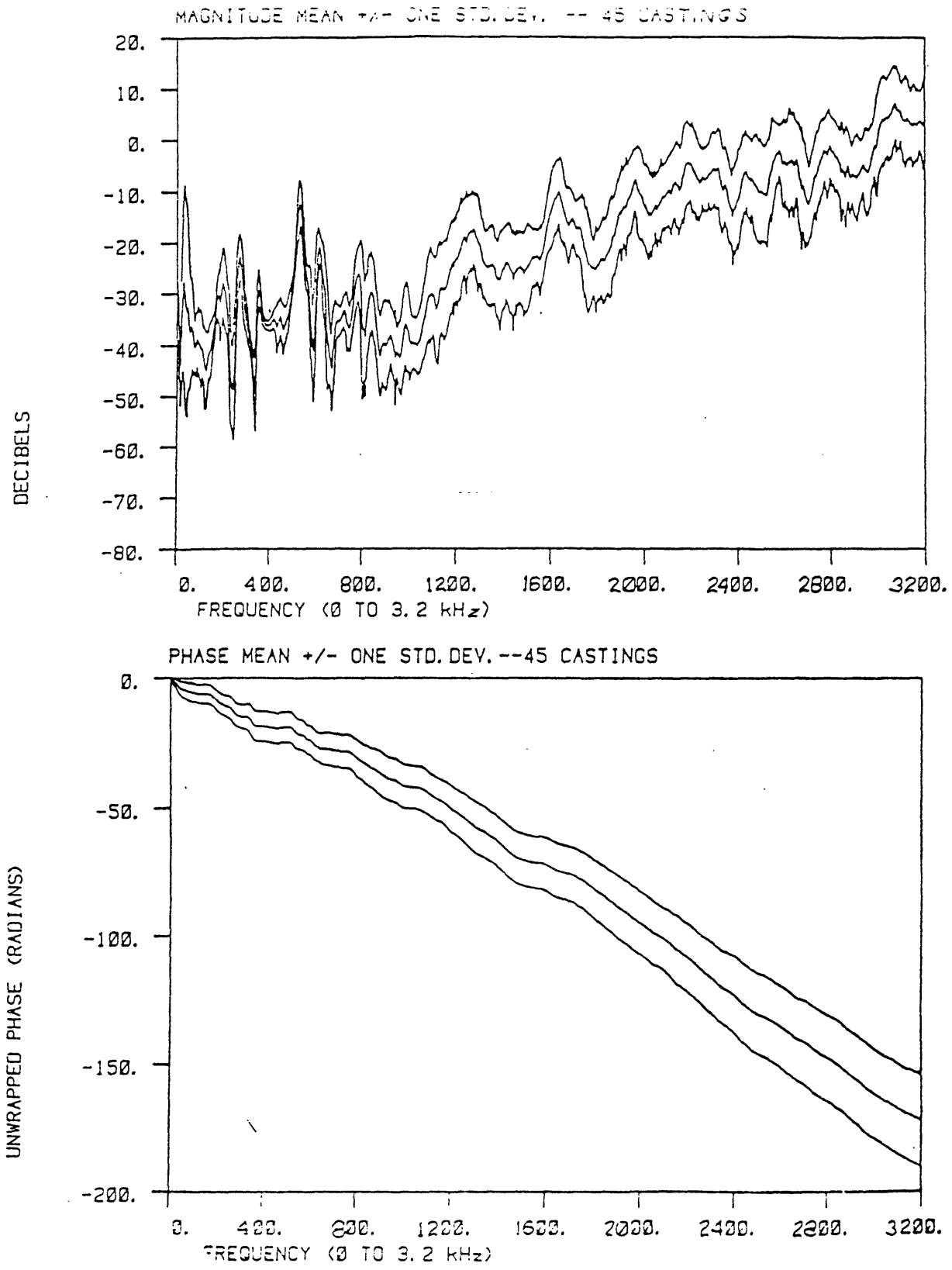

Figure 3.1 Transfer function variation of 45 identical engine castings

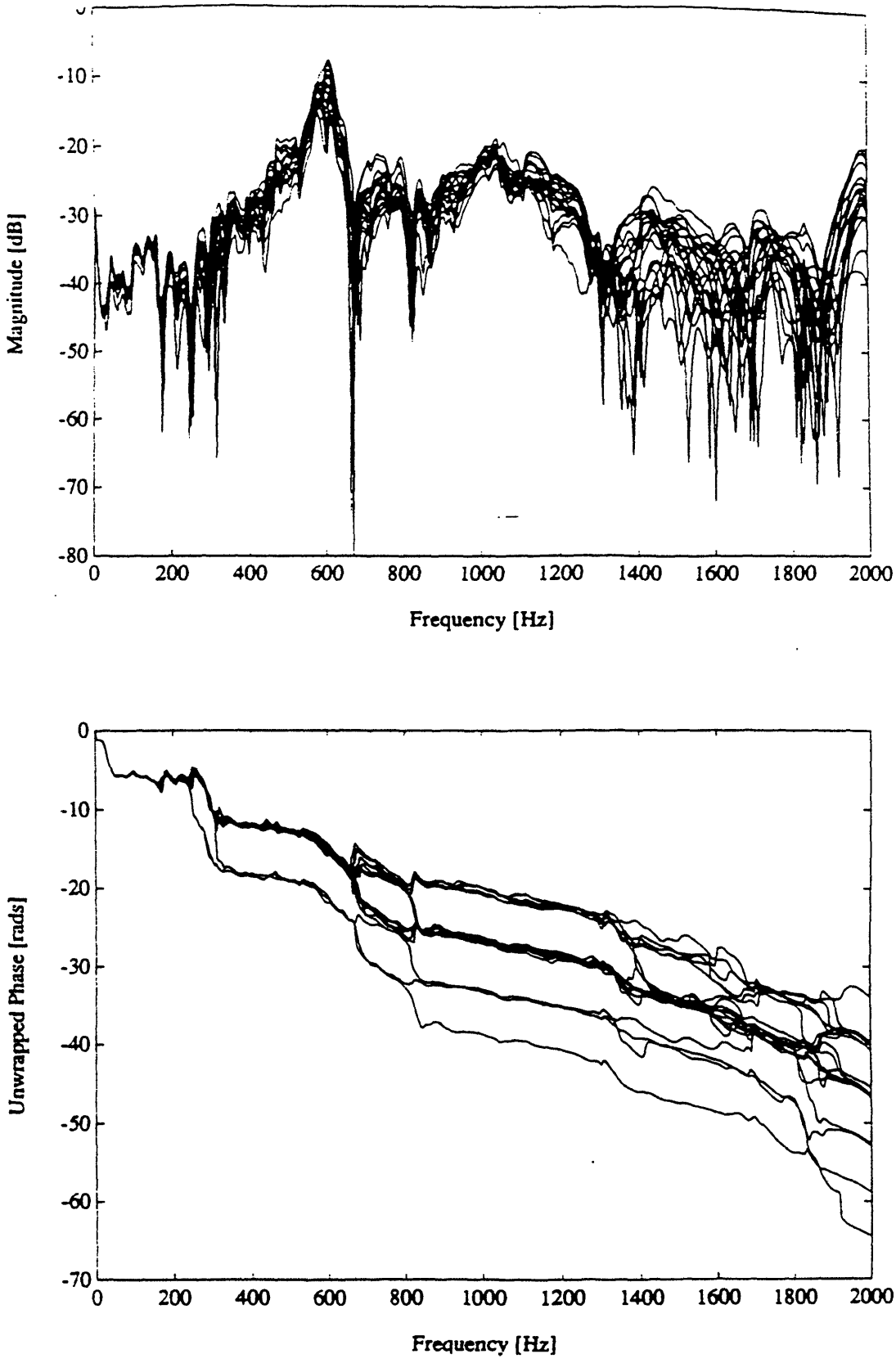

Figure 3.2 Transfer function variation of a compressor during normal operation

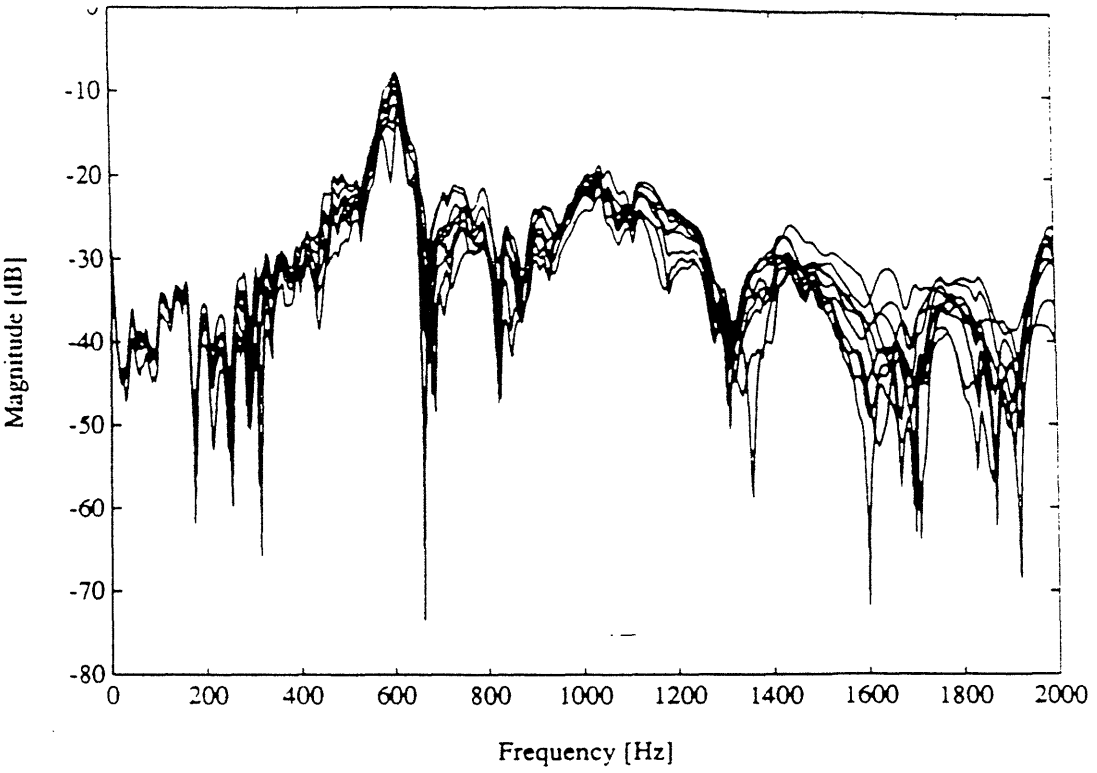

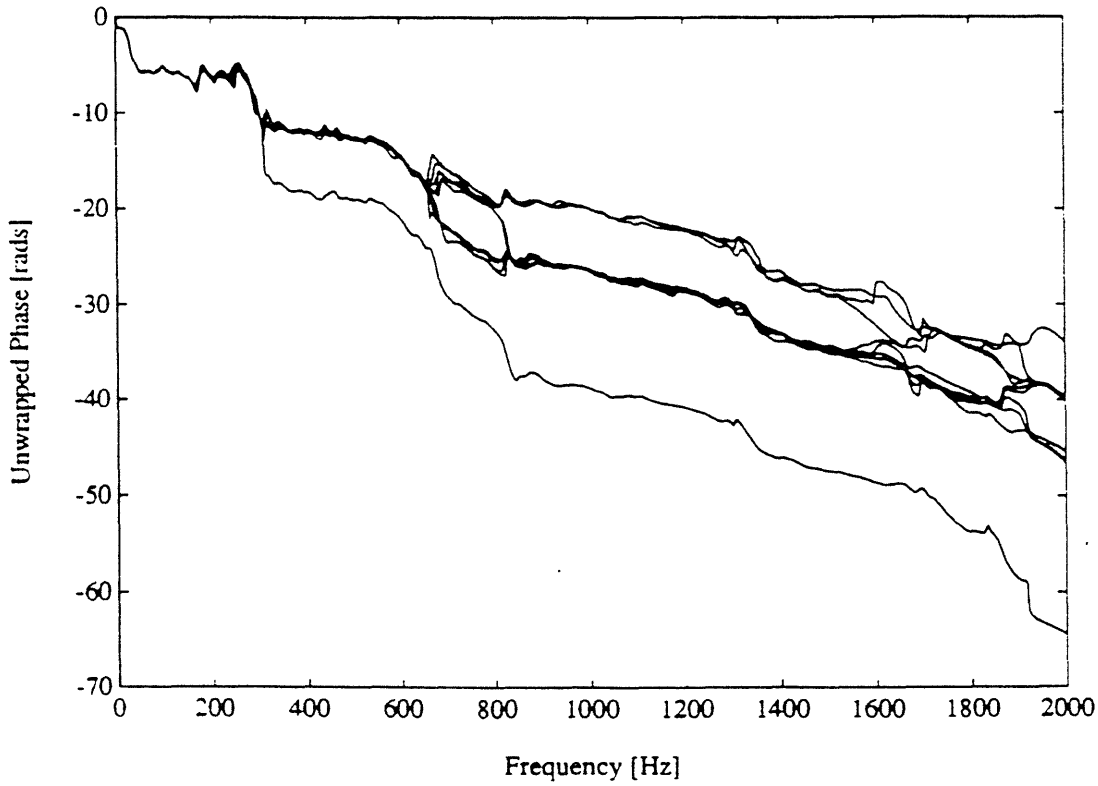

Figure 3.3 Transfer function variation of a compressor during cold operation

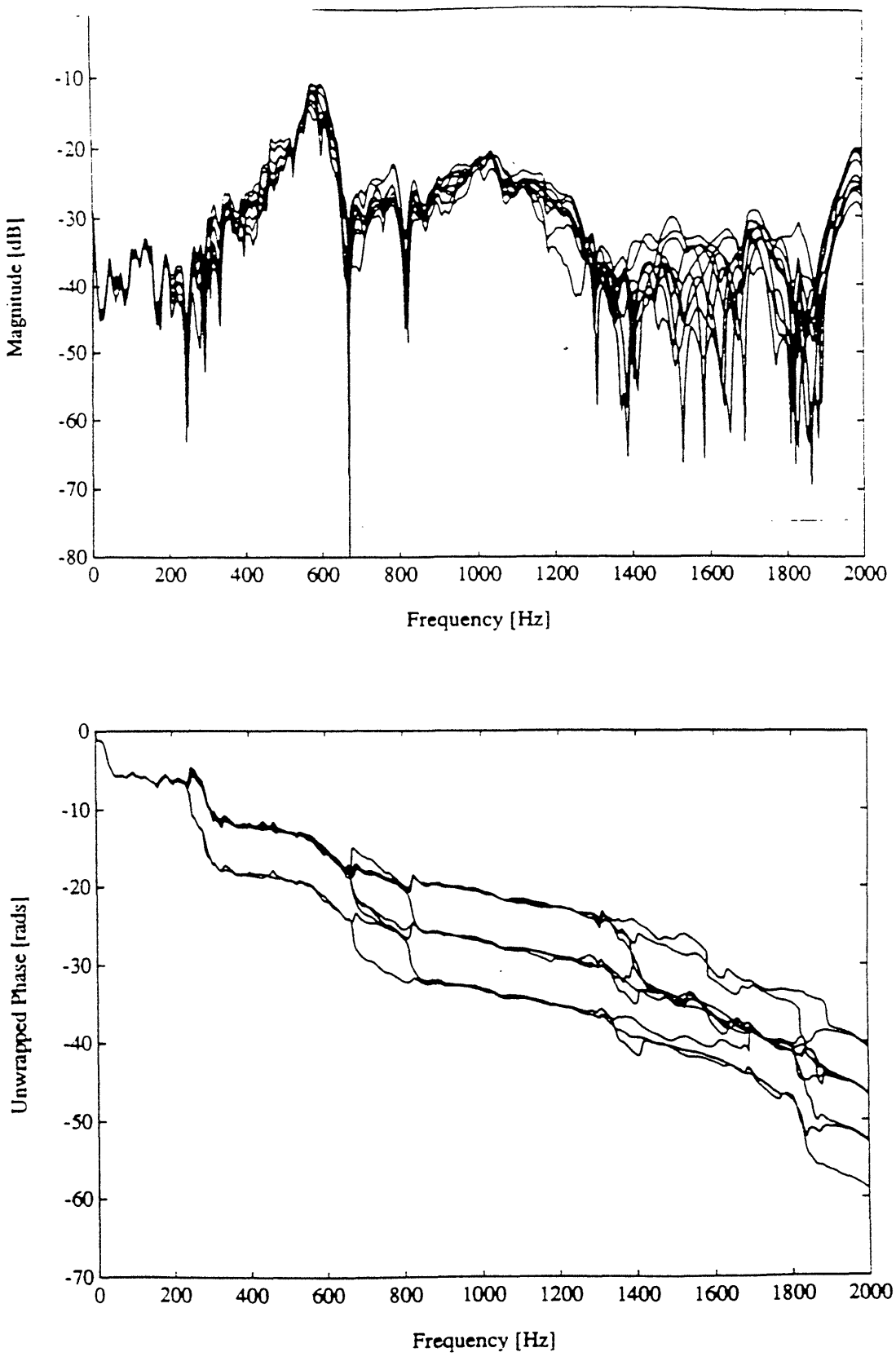

Figure 3.4 Transfer function variation of a compressor during warm operation

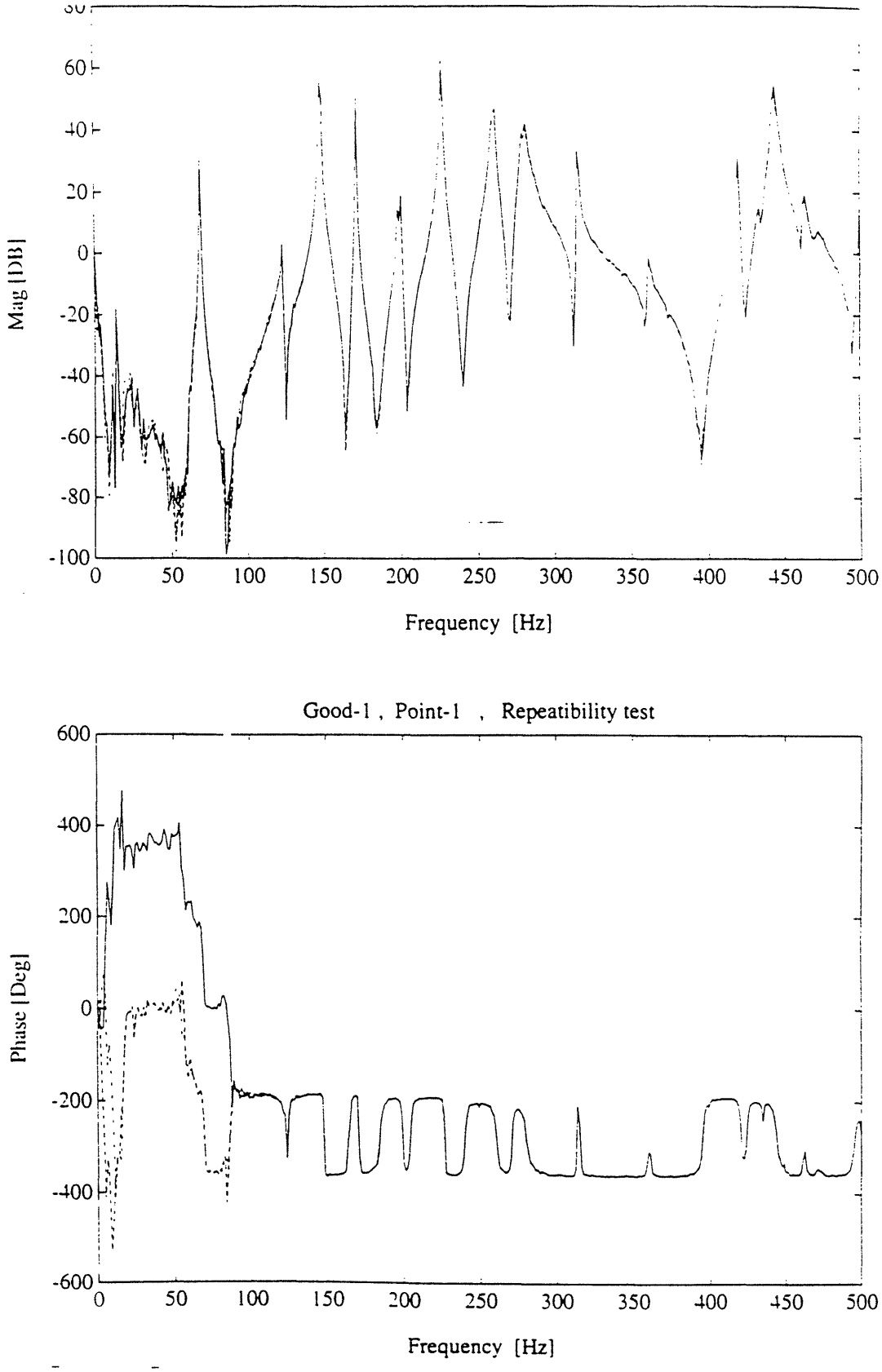

Figure 3.5 Repeatability test : Successive measurements are plotted on top of each other

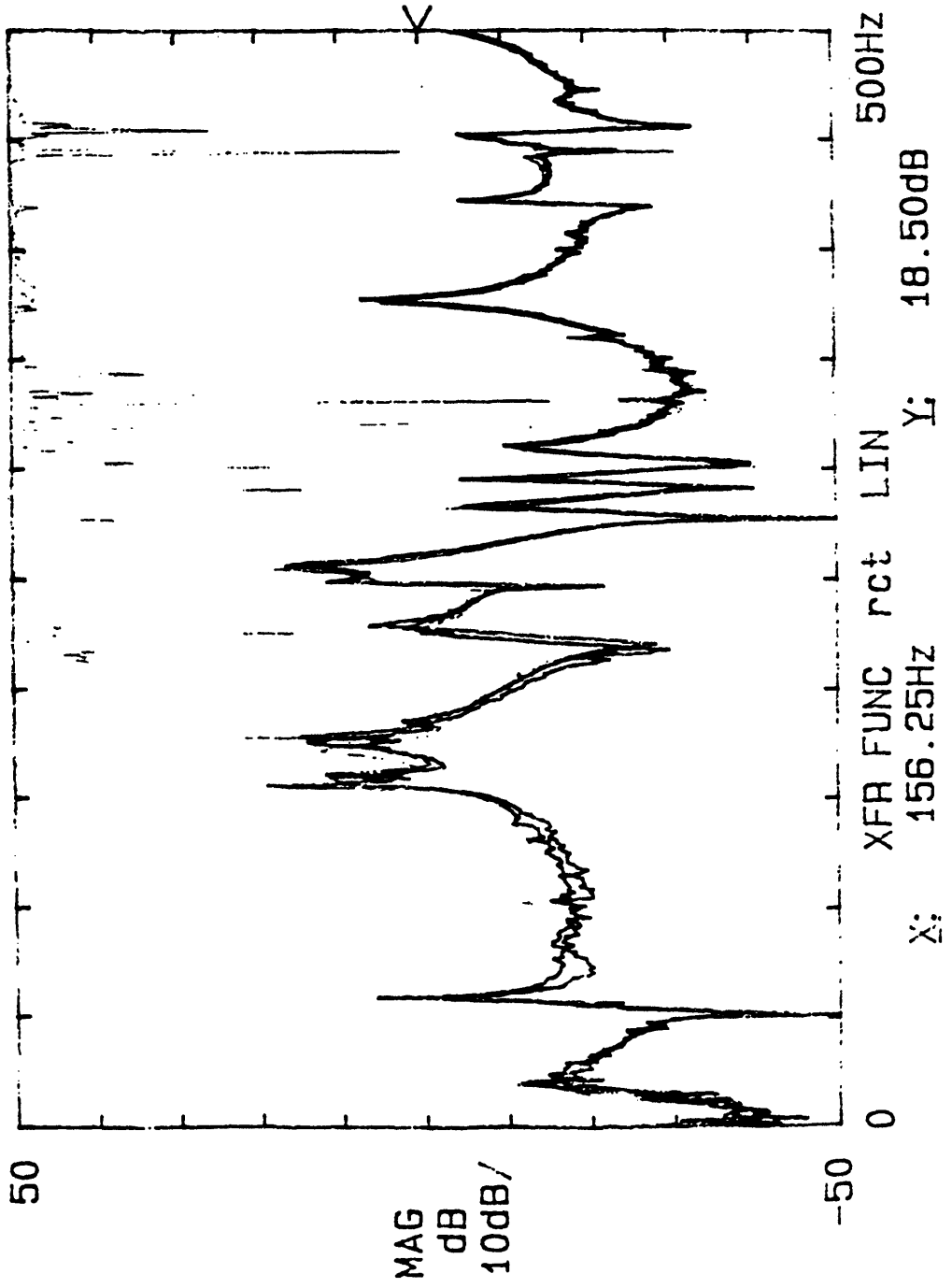

Figure 3.6 Repeatability test : Measurements before and after disassembly are plotted on top of each other

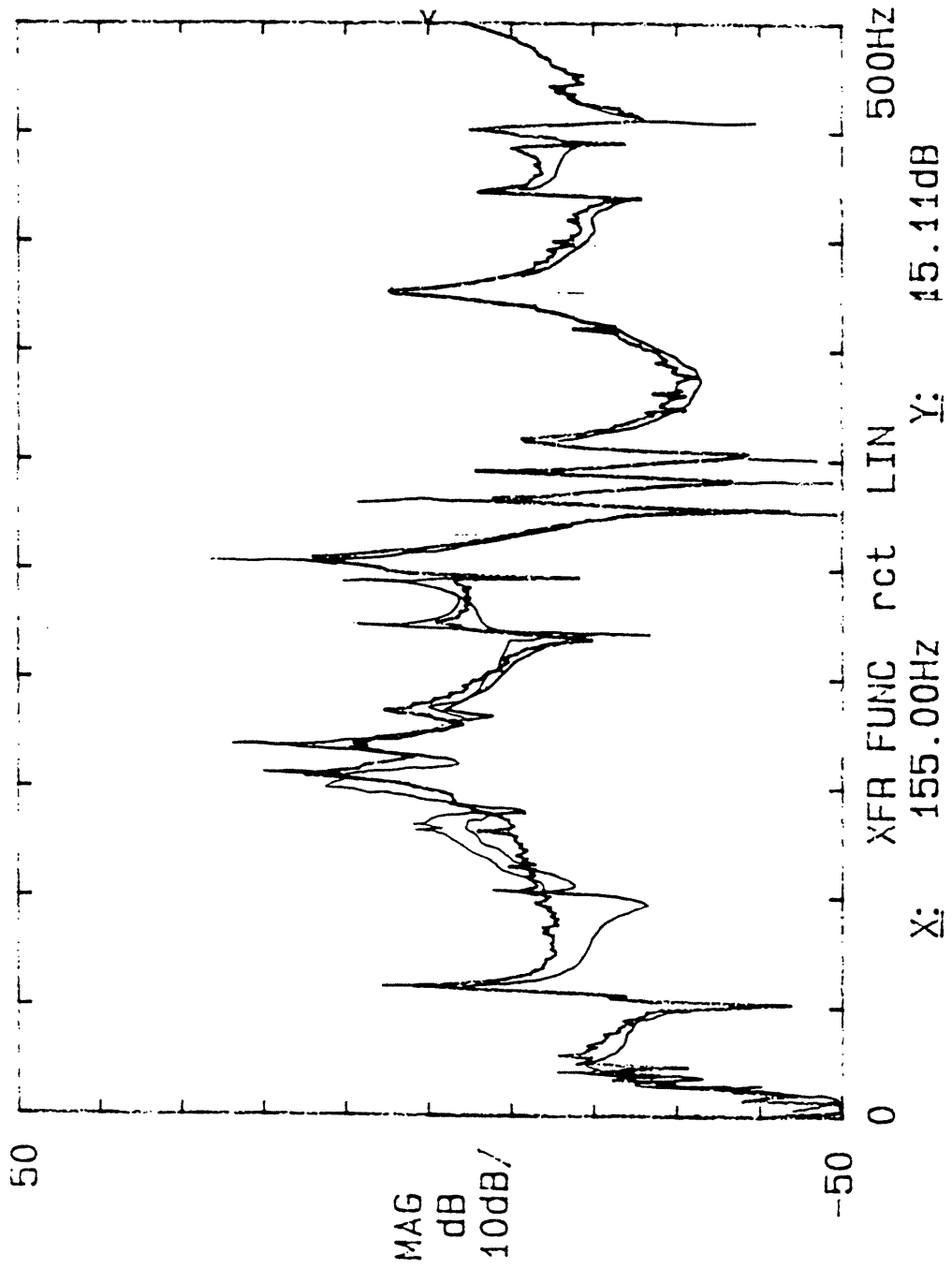

Figure 3.7 Experimental variation due to improper shaker attachment

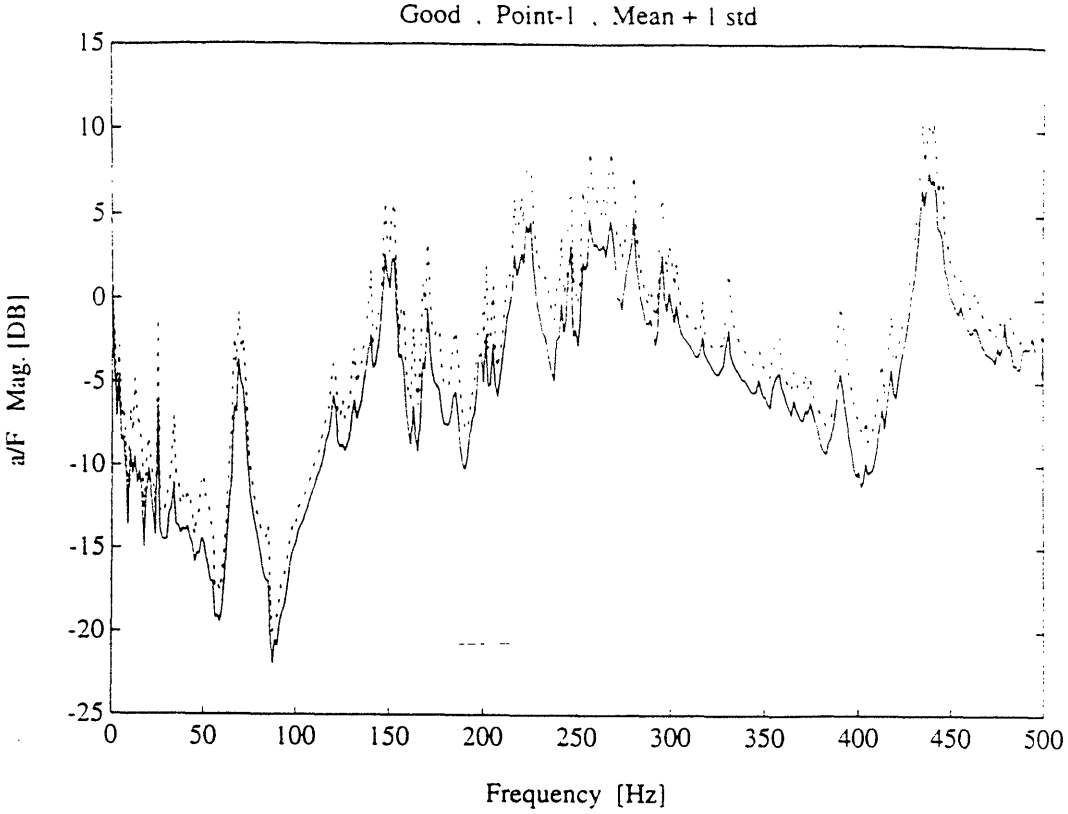

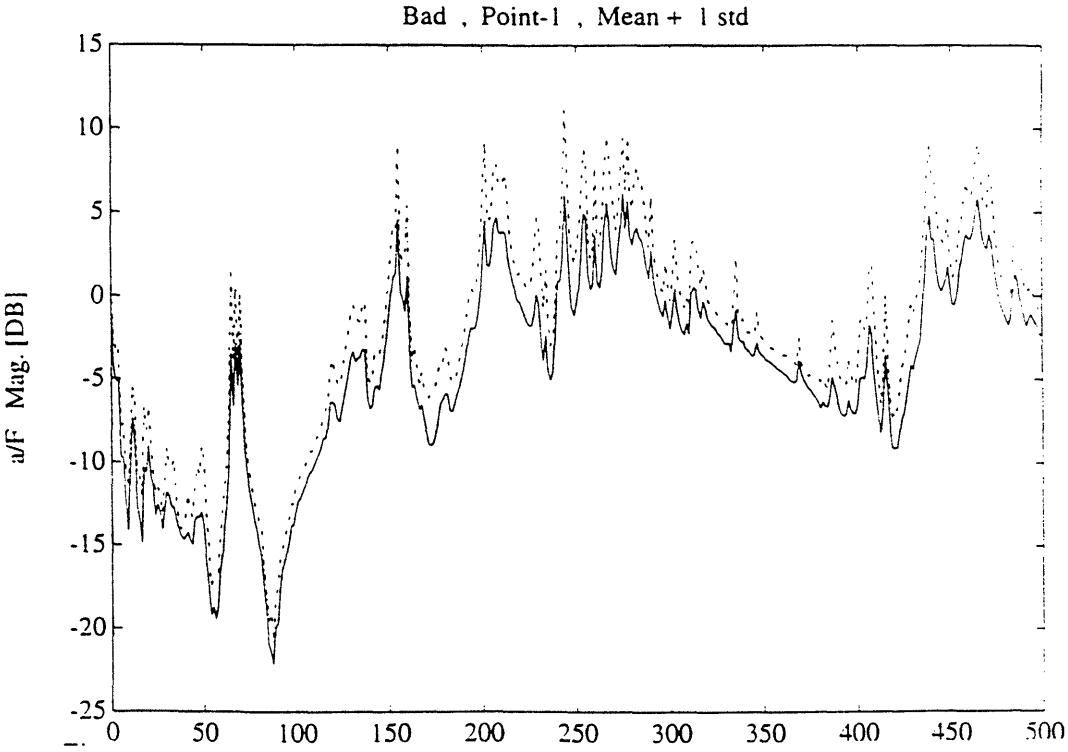

Figure 3.8 Transfer function variation of 9 *identical good* and 9 *identical bad* test pieces : point 1

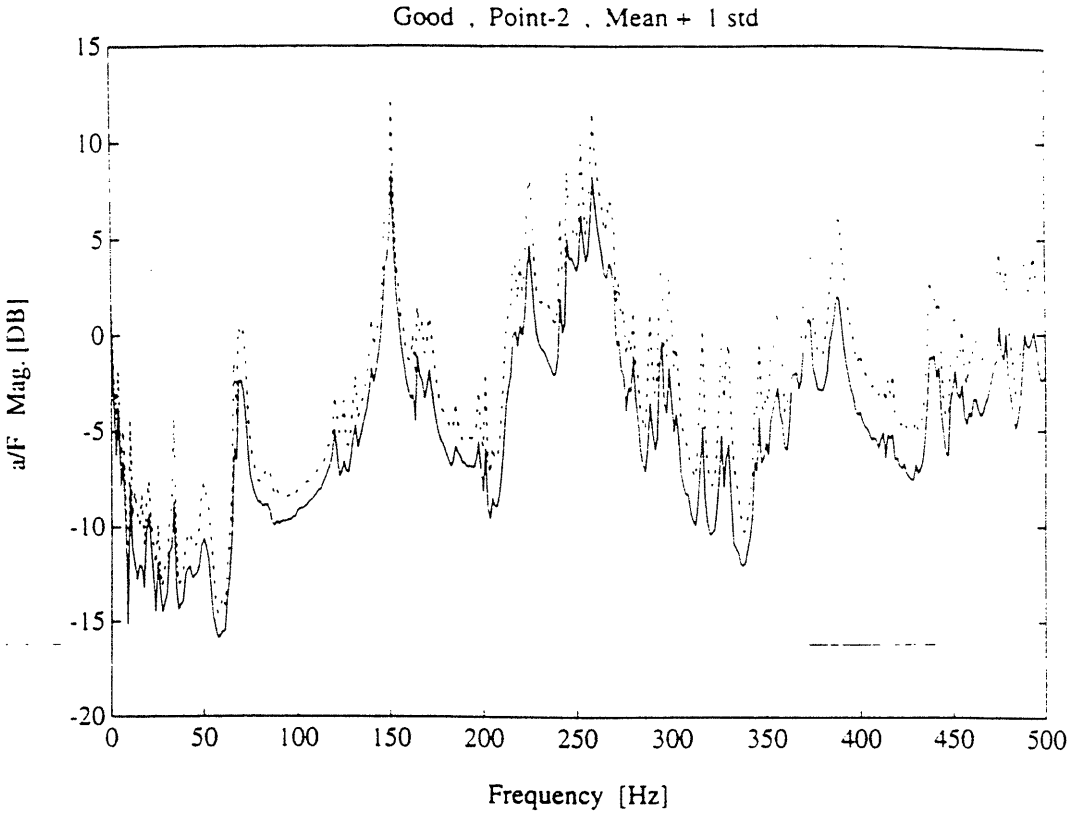

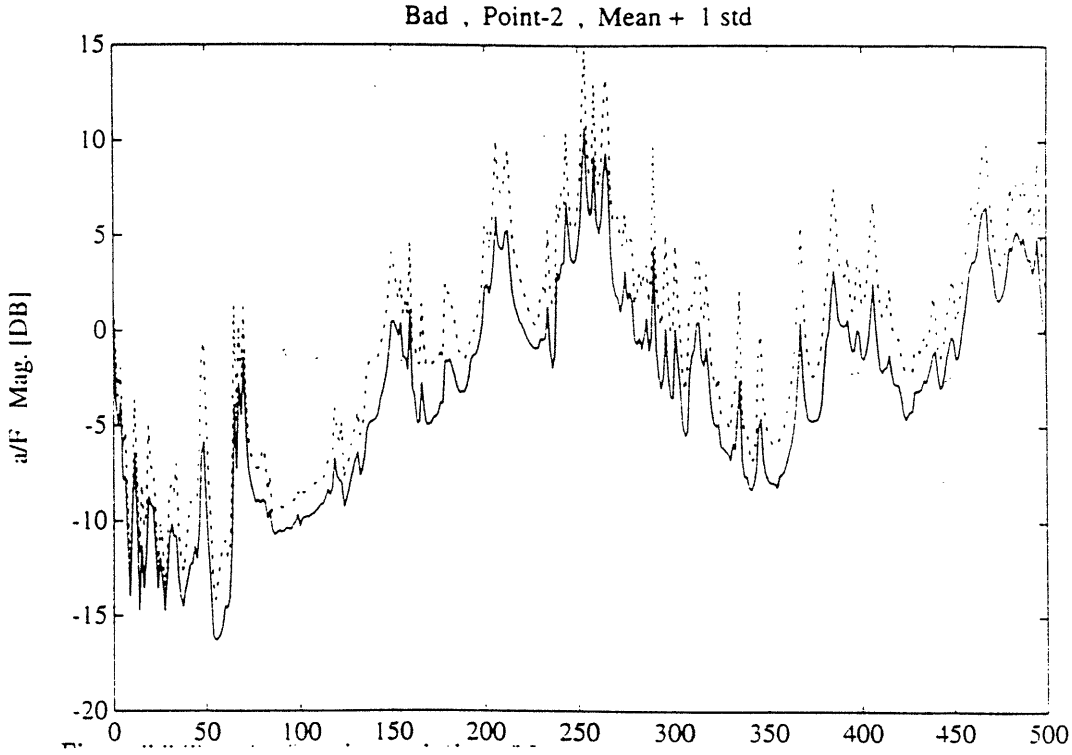

Figure 3.9 Transfer function variation of 9 *identical good* and 9 *identical bad* test pieces : point 2

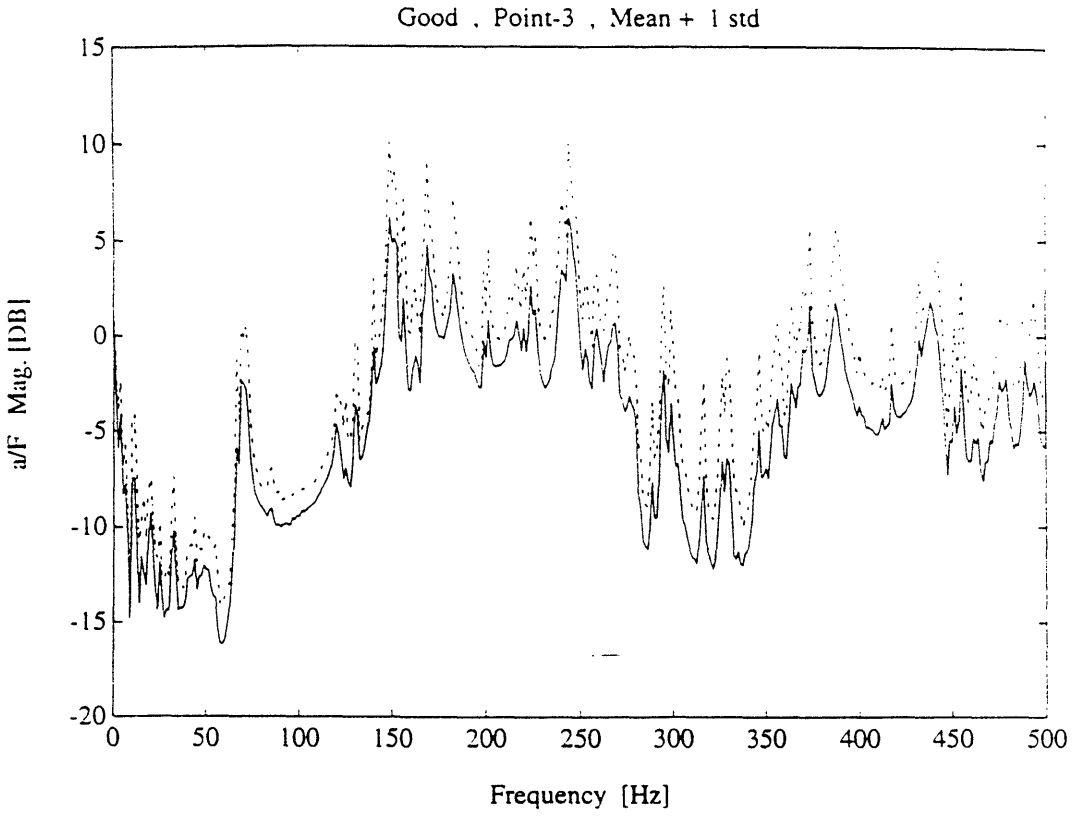

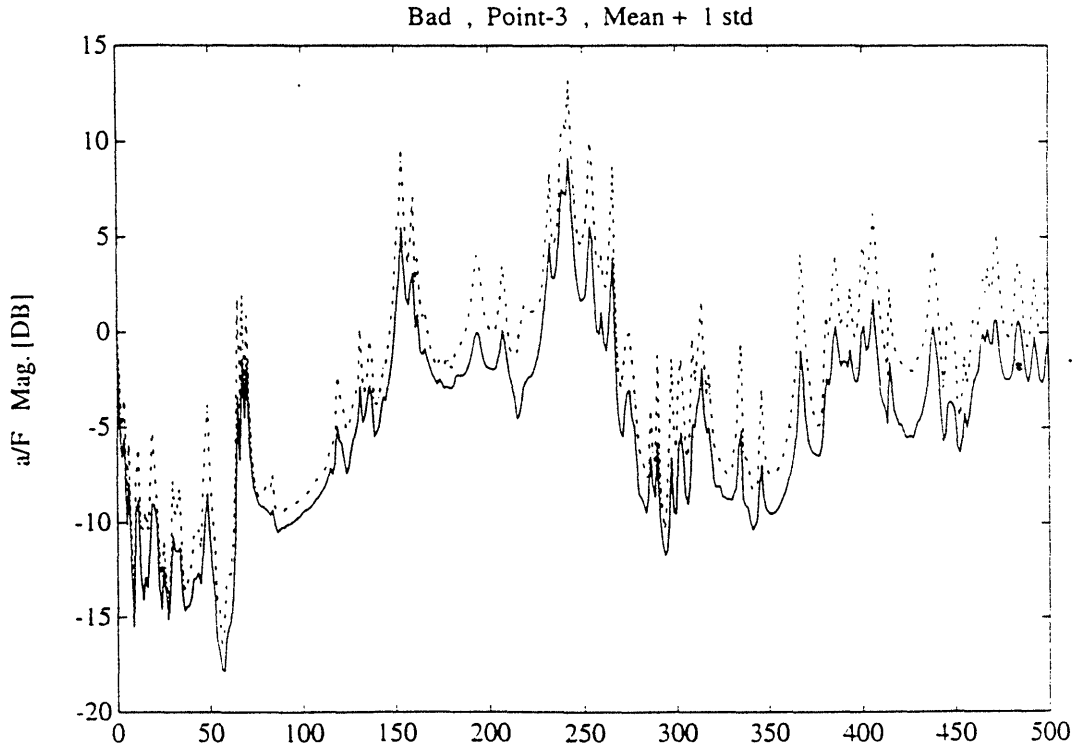

Figure 3.10 Transfer function variation of 9 *identical good* and 9 *identical bad* test pieces : point 3

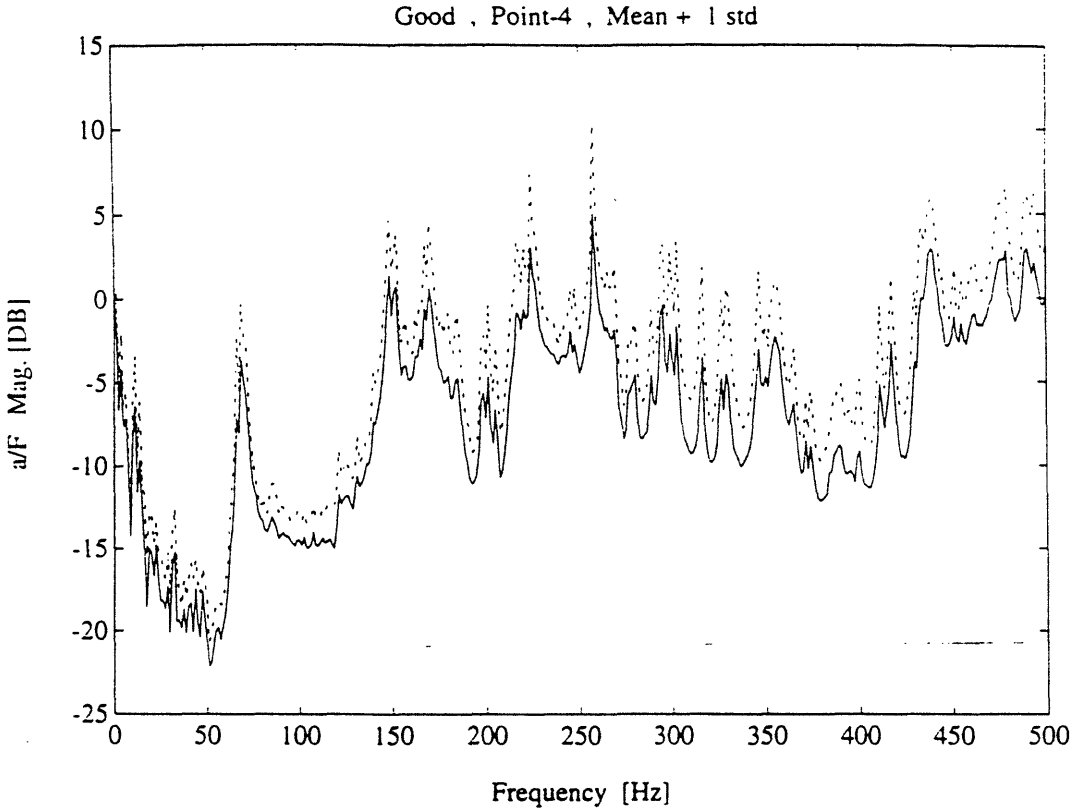

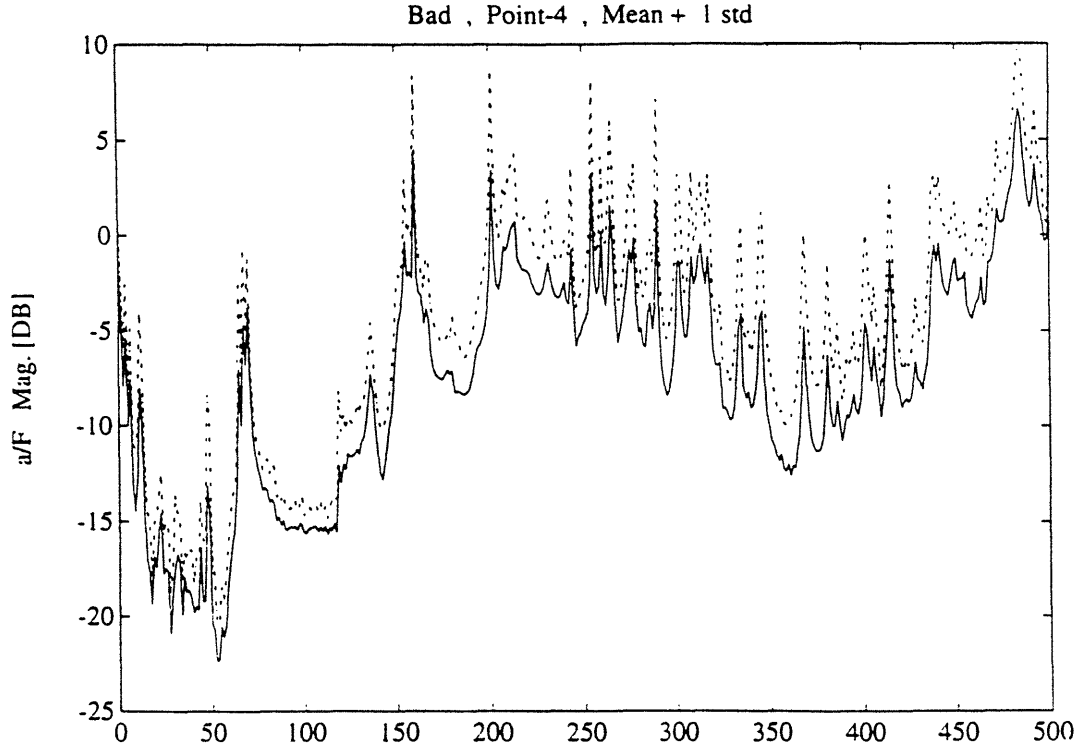

Figure 3.11 Transfer function variation of 9 *identical good* and 9 *identical bad* test pieces : point 4

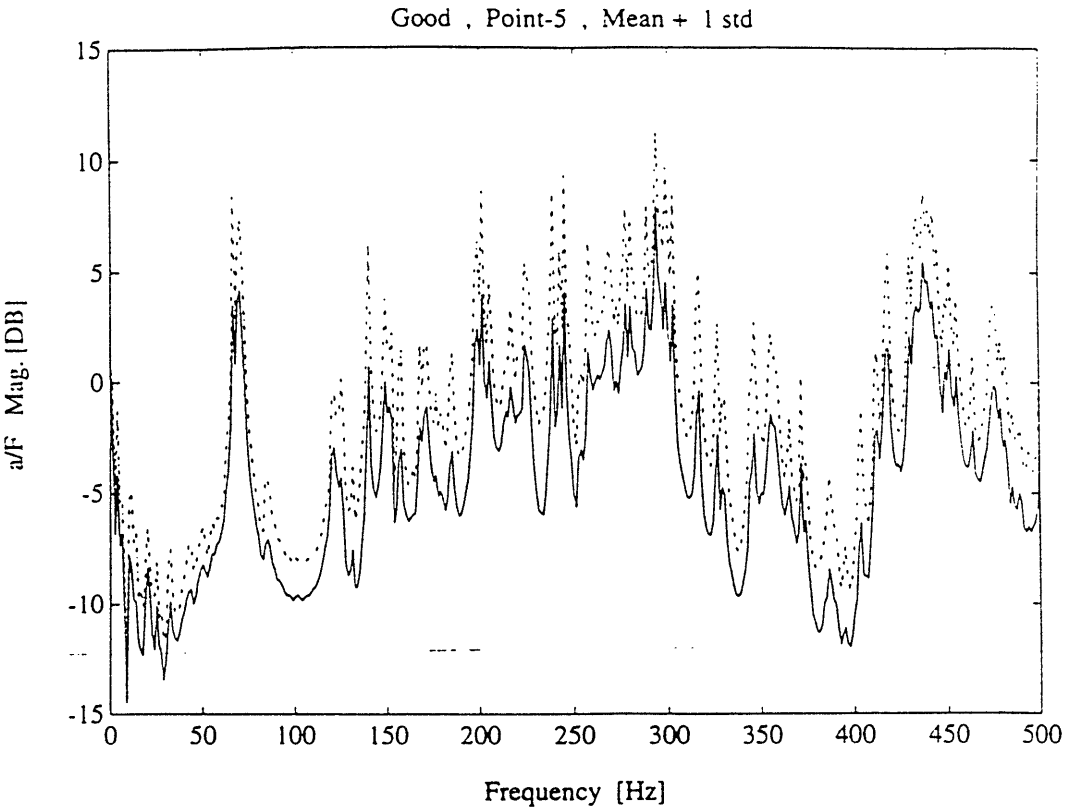

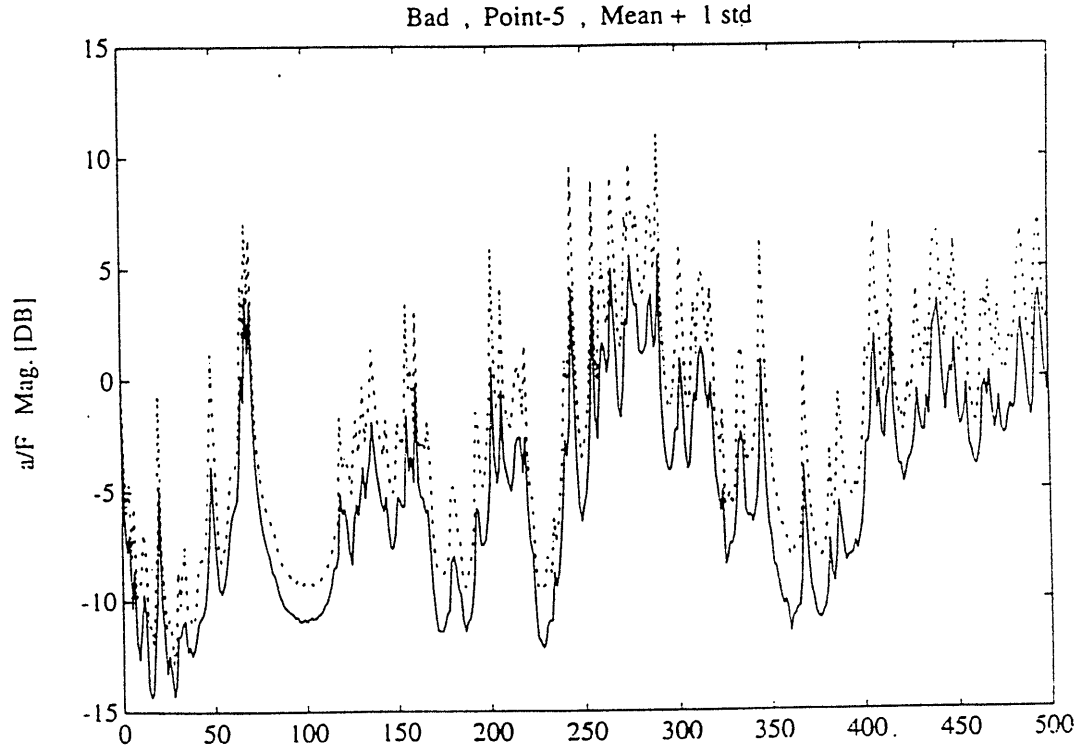

Figure 3.12 Transfer function variation of 9 *identical good* and 9 *identical bad* test pieces : point 5

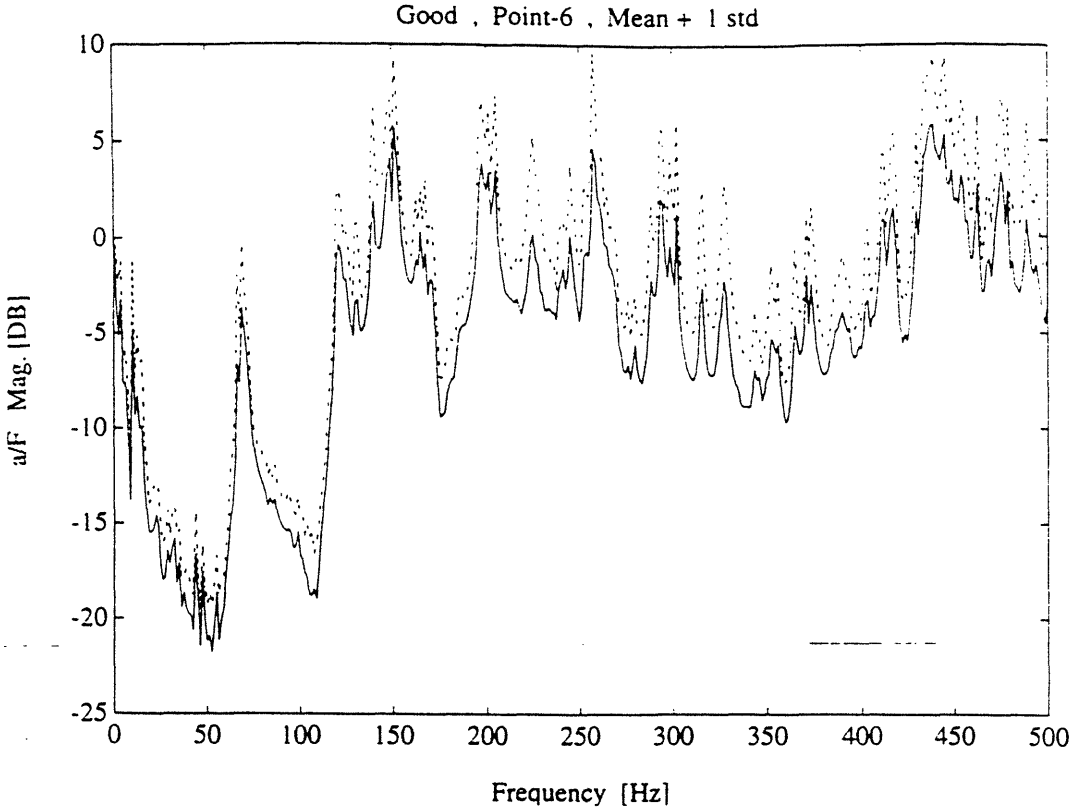

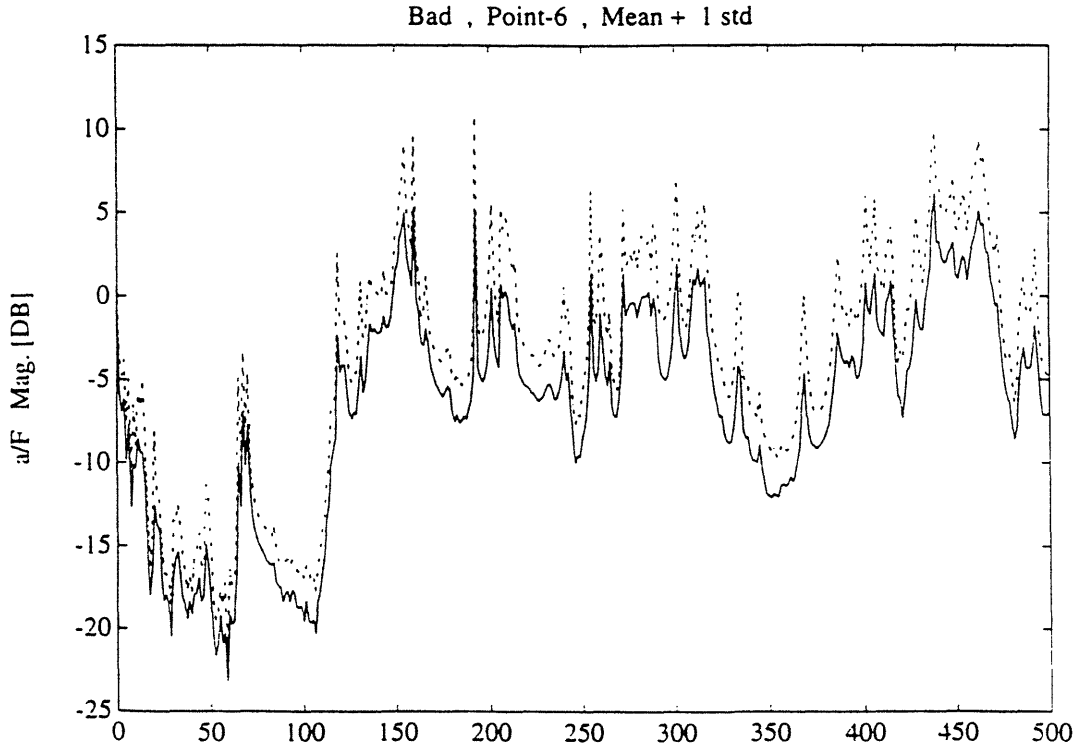

Figure 3.13 Transfer function variation of 9 *identical good* and 9 *identical bad* test pieces : point 6

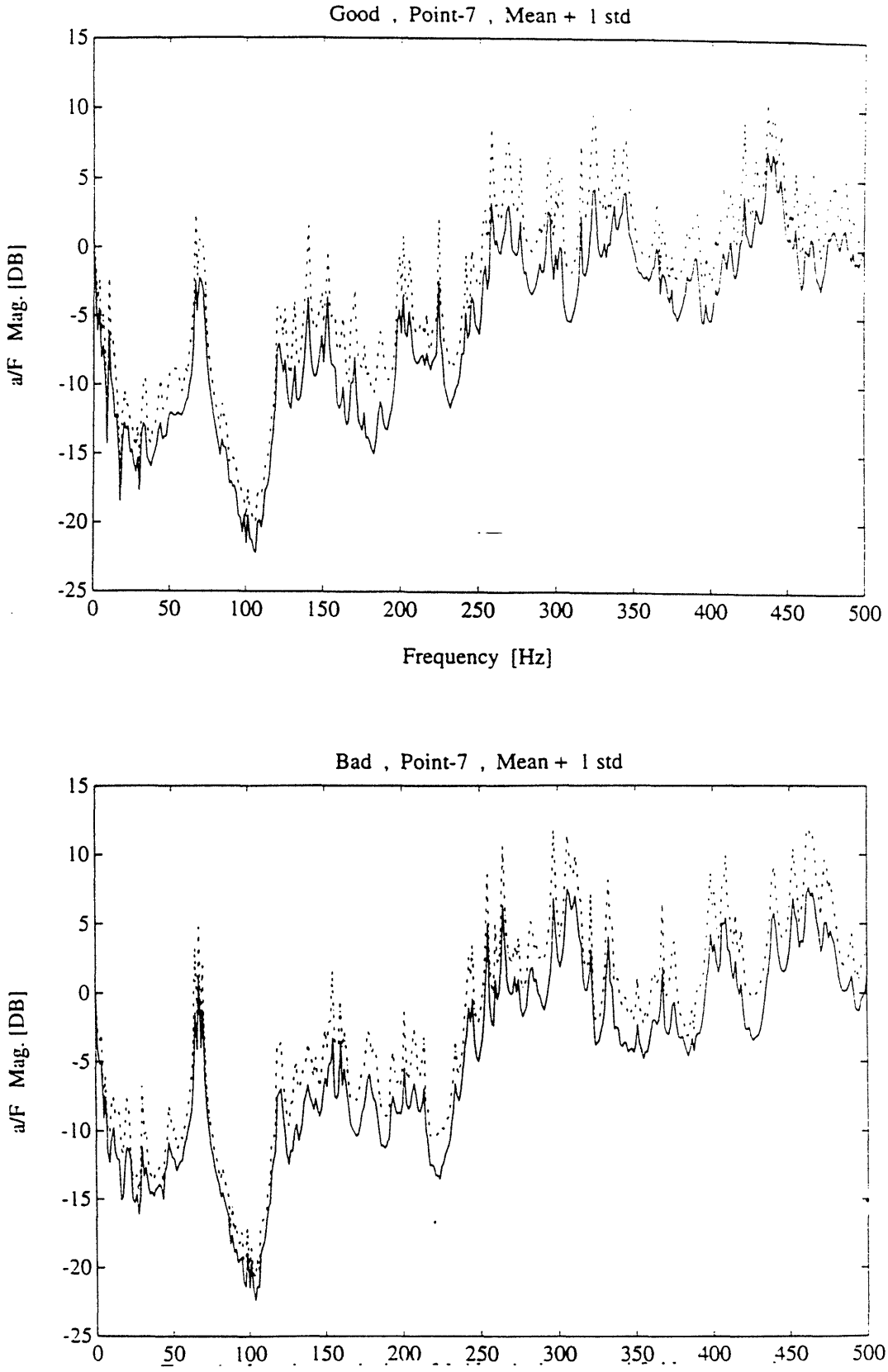

Figure 3.14 Transfer function variation of 9 *identical good* and 9 *identical bad* test pieces : point 7

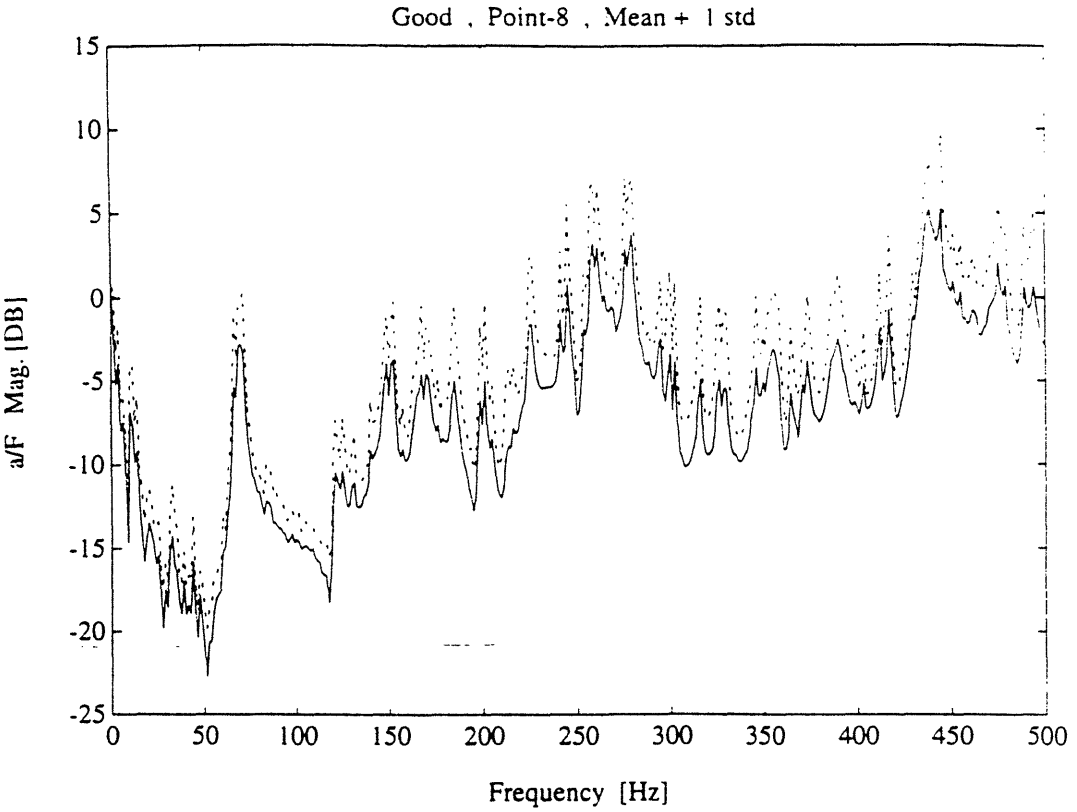

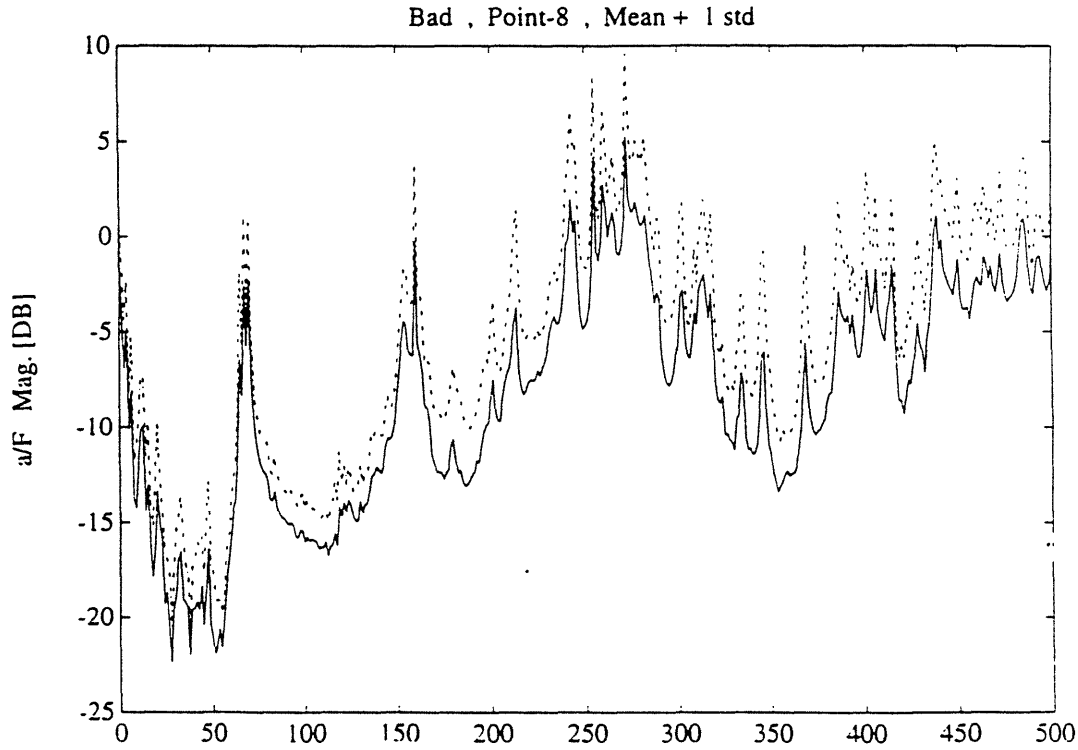

Figure 3.15 Transfer function variation of 9 *identical good* and 9 *identical bad* test pieces : point 8

Chapter 4

Transfer Function Study

The transfer function is defined as the ratio of the output signal to the input signal in the frequency domain. It reveals the structural characteristics of the test piece. As a result, the TF tells about the structure itself, which is of interest in fault diagnosis.

4.1 Background

TF is one of the most important tools in the diagnosis of structures. The input and output time signals are sampled and the fourier transforms are calculated. The ratio of the two is called the *transfer function.* The TF has an imaginary part as well as a real part. It is generally presented in the magnitude-phase form, as shown in figure 4.1. Most of the commercially available fault diagnosis techniques make use of the magnitude. On the other hand, there are few applications based on phase.

The peaks in magnitude plot reveal the poles, in other words, resonances. Structures can easily accept energy at such frequencies. The valleys in the magnitude plot reveal the zeros of the transfer function. In figure 4.1 the output signal is the acceleration at the measurement point and the input is the force signal at the excitation point.

Furthermore, the TF phase can be represented in several ways. It can be presented in wrapped phase form, which varies between $-\pi$ and $+\pi$ radians. Then, wrapped phase can be unwrapped using one of the phase unwrapping algorithms. It is generally the un-

wrapped phase which is of interest. The phase unwrapping algorithms are observed to miss some zeros close to the real frequency axis [4,8]. During data processing, phase unwrapping algorithms of both the FFT analyzer and MATLAB are tested. As it is shown in figure 4.2, the FFT analyzer phase unwrapping algorithm missed one of the pole-zero pairs close to the real frequency axis, whereas MATLAB's phase unwrapping algorithm detected the sharp pole-zero pair. This is a clear evidence for the importance of a correct choice of phase unwrapping algorithm.

There is a $-\pi$ step change in phase for each pole and a $+\pi$ step change in phase for each minimum phase zero [1]. The minimum phase zeros are the ones above the real frequency axis, whereas the non-minimum phase zeros are located below the real frequency axis, as shown in figure 4.3. The non-minimum phase zeros give a $-\pi$ step change in phase.

As the test frequency line is lowered, which corresponds to applying an exponential window in the time-domain, the non-minimum phase zeros may become minimum phase zeros. This makes a $+2\pi$ change in the total accumulated phase. The physical interpretation of the lowered frequency line is an increase in damping [8]. Eventually, damping reaches a certain point where all the non-minimum phase zeros become of minimum phase type. This is the propagation delay [8].

As shown in figure 4.3, the poles are expected to be lying on a line, whereas zeros can be anywhere in the plane [11]. For a drive-point measurement, poles and zeros alternate and all zeros lie on the pole-line. Moreover, as the measurement point moves away from the excitation point, zeros start moving away from the pole-line. Whilst, poles stay on the pole-line [11].

Another interesting feature is the effect of impulse response truncation on total accumulated phase. This is observed when the time record length of measurement isn't long enough to capture the whole impulse response of the test piece or in other words when the frequency line spacing of the measurement is not small enough to allow the impulse response of the structure to diminish rapidly enough. For instance, if the frequency line

[1] Note that the convention is e^{+jwt} time dependence

spacing is 2 Hz, then 0.5 second of the structure's impulse response is captured. The rest is truncated unless the structure's impulse response dies out in 0.5 seconds. The adverse effect of impulse response truncation is an extra *artificial* phase contribution to total phase [9]. The more complex the structure is, the longer time record length of measurement is required to eliminate artificial phase component due to impulse response truncation.

4.2 Impulse Response Truncation and Its Consequences

Realizing that impulse response truncation may have adverse effects on the TF phase the impulse responses of our measurements are checked. Figures 4.4 and 4.5 show some amount of impulse response truncation. All other impulse responses follow the same pattern. In our case, there are 400 spectral lines in the 0-500 Hz range. So the resolution in frequency is 1.25 Hz. The reciprocal of 1.25 is 0.8 seconds, which is the time record length of the measured impulse response. It is clear that the impulse response of the test piece does not die out in 0.8 seconds. A longer time record length is required. In other words, more spectral lines are required to eliminate the impulse response truncation effect. To judge the adverse effect of the impulse response truncation, several different exponential windows are applied to the original data. Figures 4.6 through 4.21 exemplify the effect of exponential windowing. The exponential window is :

$$w(t) = e^{\frac{-t}{t_c}} \tag{4.1}$$

It is recommended that t_c be picked to be at most one-quarter of the time record length [3]. Three different windows are applied, T/4, T/16,T/32. The original data has the lowest structural damping value. The structural damping increases as the t_c, the time constant of the exponential window, is lowered. So in figures 4.6 through 4.21 $t_c = T/32$ has the highest structural damping value. Since it is too high a damping value for the test piece, the total accumulated phase at 500 Hz almost represents the propagation delay of the test piece. At this particular damping value, almost no reverberations occur and the measured total accumulated phase is solely due to the direct propagation delay. Since exponential windowing in the time domain is equivalent to adding damping to the structure, the expectation is a smaller total phase with increase in the structural damping [8]. Reviewing

figures 4.6 through 4.21, it is noticed that the windowed data perfectly follow the expected pattern with some exceptions at low frequencies.

For instance, the original data, which has the least damping of all, has greater total phase especially up to 250 Hz. Figures 4.25 through 4.32 demonstrate typical coherence plots of both thegood and bad test pieces for 8 measurement points. The coherence plots are almost unity except below 50 Hz. The major reason is the shaker's inability to input enough energy at low frequencies due to the displacement limitation on the moving element of the electrodynamic type shaker used in the experiment. Since the shaker can't provide enough energy to the test piece at low frequencies, noise in the test set-up dominates the measurements at low frequencies resulting in low frequency artificial peaks and valleys in the TF. Figures 4.6 through 4.21 clearly demonstrate the low frequency artificial poles and zeros. For instance, in the phase plot of figure 4.11 the original data has less accumulated phase at 500 Hz than the windowed TF data. This is physically unlikely since windowing is equivalent to adding damping to the test piece. The test piece with less structural damping has to have more phase. Careful investigation proves that the discrepancy in total accumulated phase of original data and the windowed data is caused by the phase contributions at low frequencies. Above 50 Hz original data and the windowed data have the same pole zero pattern.

As a result of this shaker limitation the phase unwrapping algorithm recognizes the low frequency artificial peaks as poles, resulting in artificial phase component at low frequencies. The remedy is to discard low frequency artificial poles and zeros. Actually discarding the artificial poles and zeros below 50 Hz [2], the phase trend of the original data and the windowed data look the same except for a decrease in phase shift due to an increase in damping.

To better visualize the effect of the impulse response truncation on the transfer function, the following experiment was carried out. Two out of the 160 impulse responses were selected, bad-3 point-3 and good-2 point-3. The fourier transforms of the 0.8 second long and 0.32 second long impulse responses were calculated and compared. The 0.32 second long

[2]As it will be explained in Chapter 5, the first mode is at 57 Hz . So discarding poles below 50 Hz is not detrimental to the modes of the test piece.

impulse response represents the truncated version of the 0.8 second long original impulse response. Figures 4.23 and 4.24 demonstrate the difference in the frequency domain for the bad-3 point-3 and good-2 point-3. There is an enormous increase in total phase. On the other hand, the TF magnitude does not change much. The pole and zero frequencies don't shift, whereas fluctuations in magnitude are observed. A theoretical study on the truncated impulse response and its effect on phase reported artificial fluctuations in TF magnitude and extra phase component due to the impulse response truncation [9]. In figures 4.23 and 4.24, the solid line represents the 0.8 second long original impulse response, whereas the dashed line represents the 0.32 second long truncated impulse response.

In figure 4.24 of good-2 point-3, the total phase of the original data is about -2000 degrees, whereas the truncated 0.32 second long impulse response has about -3500 degrees of total phase at 500 Hz. Clearly, the 1500 degrees of difference is an extra artificial phase component due to the impulse response truncation. In figure 4.23 of bad-3 point-3, the total phase of the original data is about -1000 degrees, whereas the truncated 0.32 second long impulse response has about -9000 degrees of total phase at 500 Hz. Clearly, the 8000 degrees of difference is an extra artificial phase component due to the impulse response truncation. The adverse effect of the impulse response truncation turns out to be more severe in the bad test piece, bad-3 point-3. This observation is also evident in figures 4.4 and 4.5, the impulse responses of the good-2 point-3 and bad-3 point-3. A longer portion of the impulse response of the good test piece is captured compared to the bad test piece. Thus, this example illustrates the importance of capturing the whole impulse response of the structure.

Since the adverse effect of the impulse response truncation is discovered, 0.8 second long original impulse responses of the test pieces are utilized in further processing of the experiment data. This observation also suggests that the better representation of the TF can be obtained by capturing longer portions of the impulse response of the test piece. The impulse response truncation has the effect of artificially moving the real frequency axis [3] upward in y direction [9]. In order to reduce the adverse effect, the real frequency axis has to be lowered down to compensate for the artificial upward movement of the real frequency axis.

[3]Refer to figure 4.3 to visualize the real frequency axis

Thus, the combined adverse effect of low coherence[4] and impulse response truncation shows up in the low frequency range. Exponential windowing seems to decrease this adverse effect. But it should be kept in mind that exponential windowing also converts non-minimum phase zeros to minimum phase zeros, resulting in less total phase than there actually is. Although windowing does not eliminate the problem completely, it reduces the problem considerably. The ideal case is to capture the whole impulse response of the test piece while making sure that enough energy is provided to the test piece especially at low frequencies. On the other hand, due to experimental limitations the ideal case may not be achieved at all times. In this case exponential windowing is observed to reduce the artificial phase components.

4.3 What the TF reveals

The TF measurements can reveal more than just the effects of impulse response truncation and exponential windowing. Careful examination of TF magnitude and phase adds to our understanding of the structure characteristics.

Figures 4.6 through 4.21 suggests that the distribution of poles in the frequency domain[5] looks like a cloud above the real frequency axis, each one having different damping values. A couple of observations leads to this idea. As damping increases, poles and zeros which are further away from the real frequency axis, disappear whereas closer ones still appear in magnitude and phase plots. A representative example is in figure 4.10. At the frequency marked by 1, there used to be a pole, giving approximately a $-\pi$ phase shift, but after applying T/32 exponential window, it becomes too far away from real frequency axis for the phase unwrapping algorithm to detect. At the frequencies, marked by 2 and 3, a similar thing happens to pole-zero pairs. Additional examples are in figure 4.11 at frequencies marked by 1, 2, 3 and 4. As far as the total phase is concerned, the smearing out of a pole with increasing damping increases the total phase by approximately π, whereas the

[4]Figures 4.25 through 4.32 present the coherence plots.
[5]Refer to figure 4.3 for the representation of poles in the frequency domain

smearing out of a pole-zero pair does not affect the total phase.

Figure 4.3 shows a typical pole-zero cloud of a structure. The non-minimum phase zeros[6] are one of the sources of problem in inverse filtering. They can easily move and become a minimum phase zero due to normal changes such as a temperature change. In figures 4.6 through 4.21, conversion of the non-minimum phase zeros to the minimum phase zeros due to increase in damping is evident. In figure 4.7 the frequencies marked as 2, 3 are the good examples of this. In figure 4.8 the frequencies marked as 1, 2, 3, 4, 5 illustrate the same phenomenon.

A stable structure has its poles above the real frequency axis, which corresponds to positive damping. Thus, each pole has to give approximately a $-\pi$ phase shift. In figure 4.22 poles at points 1 and 2 give a $+\pi$ *phase shift*, implying that these two poles are *below* the real frequency axis. Since the measurements belong to a stable structure, these two poles can not be below the real frequency axis, which would imply instability. These *minimum phase poles* are clear evidences of the impulse response truncation effect. As explained earlier in this chapter, truncation has the effect of artificially moving the real frequency axis up [9]. So these two poles, which have very low damping [7] stay below the real frequency axis after the axis's upward movement due to truncation.

[6] Zeros below the real frequency axis.
[7] very close to real frequency axis

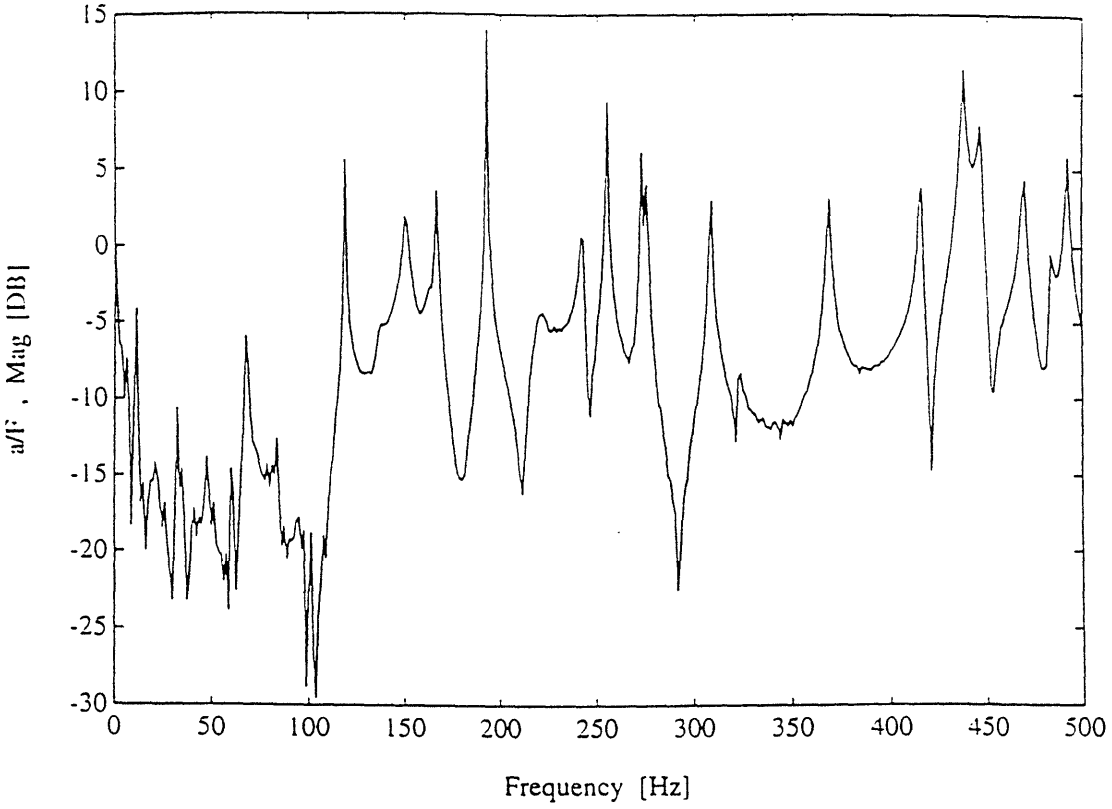

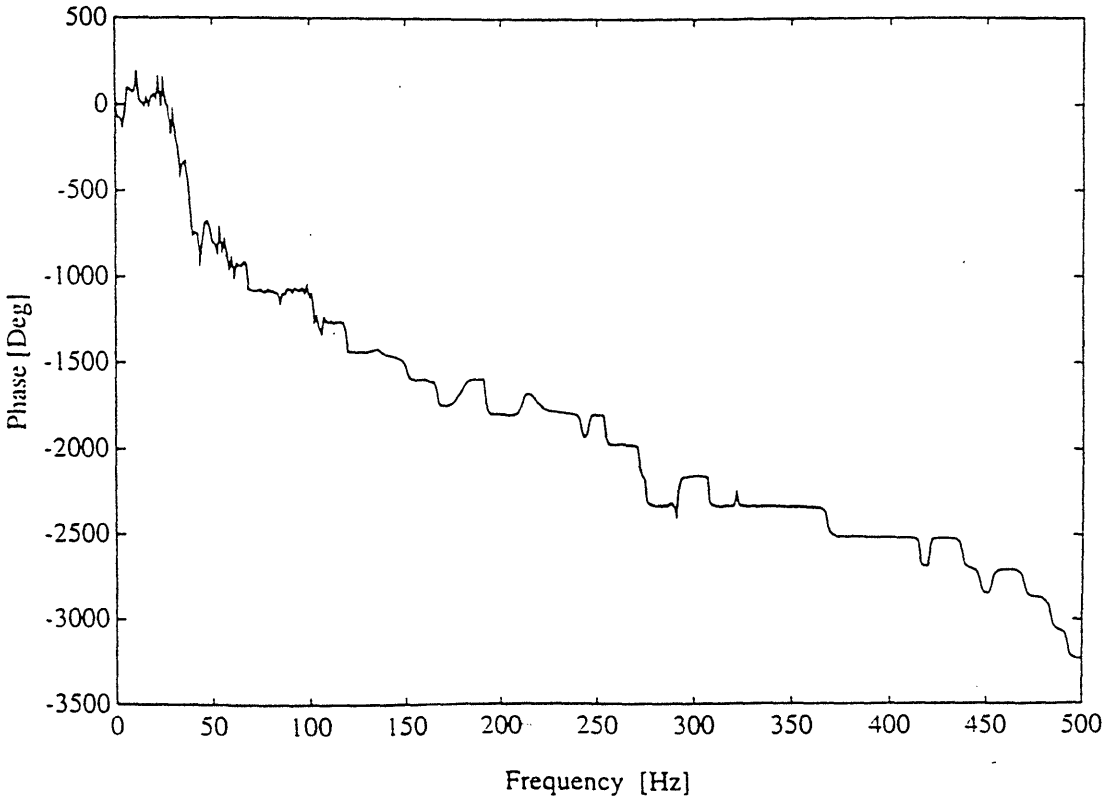

Figure 4.1 Transfer function magnitude and unwrapped phase

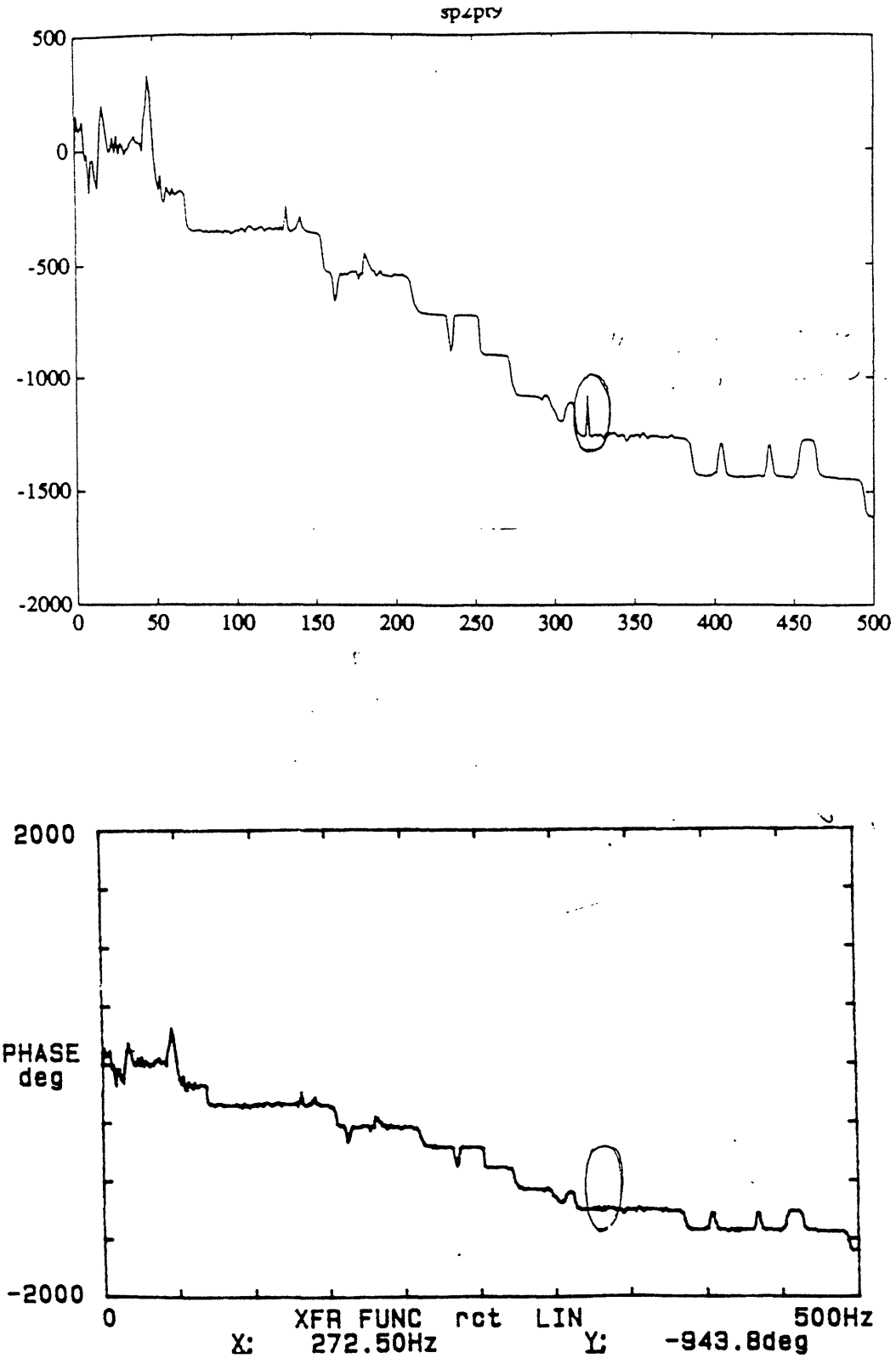

Figure 4.2 Importance of phase unwrapping algorithm :
Top plot by MATLAB,bottom plot by FFT analyzer.
At 325 Hz , FFT analyzer missed one pole-zero pair

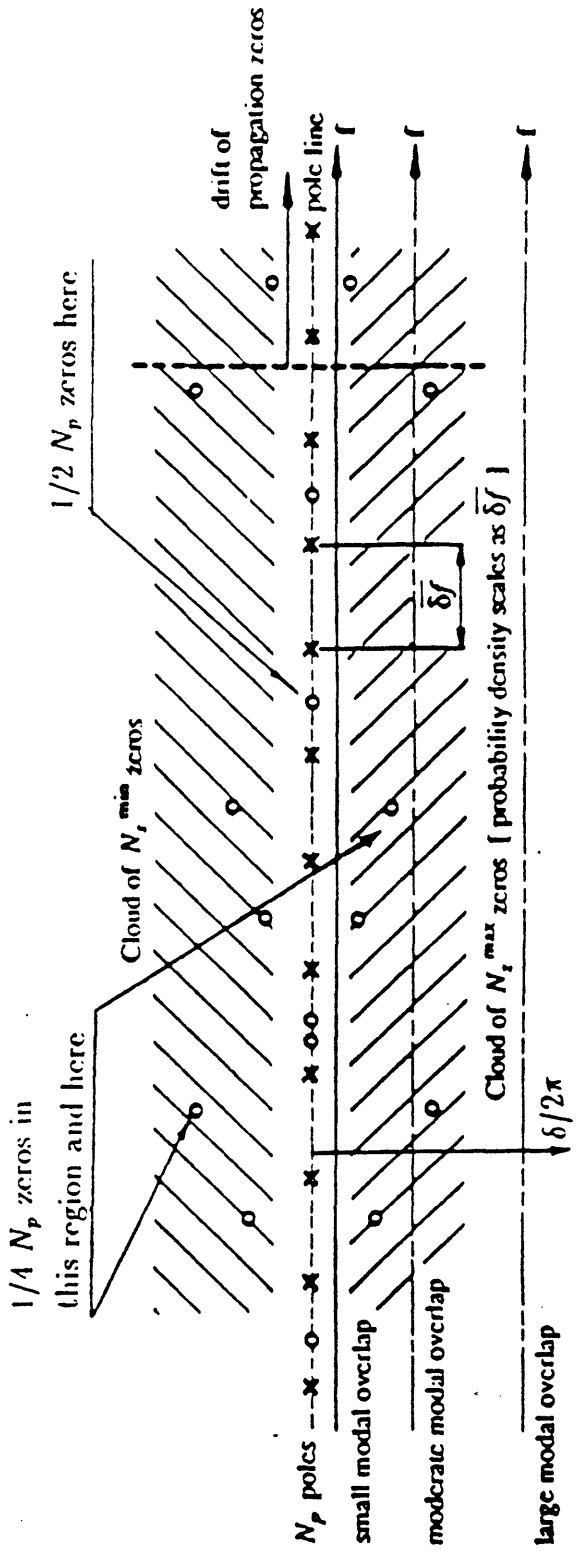

Figure 4.3 Typical pole-zero distribution of a system

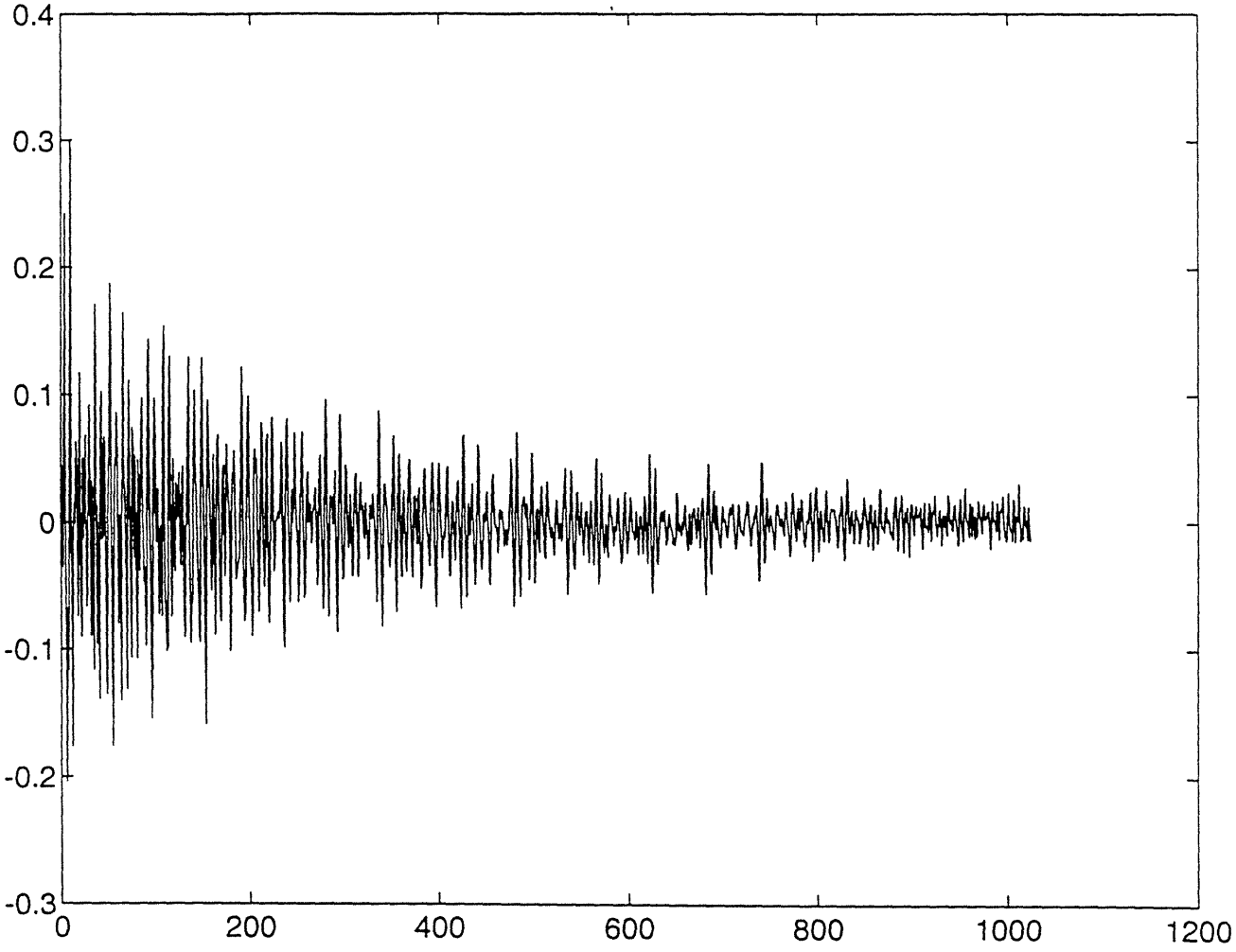

Figure 4.4 Impulse response of good-2 point-3

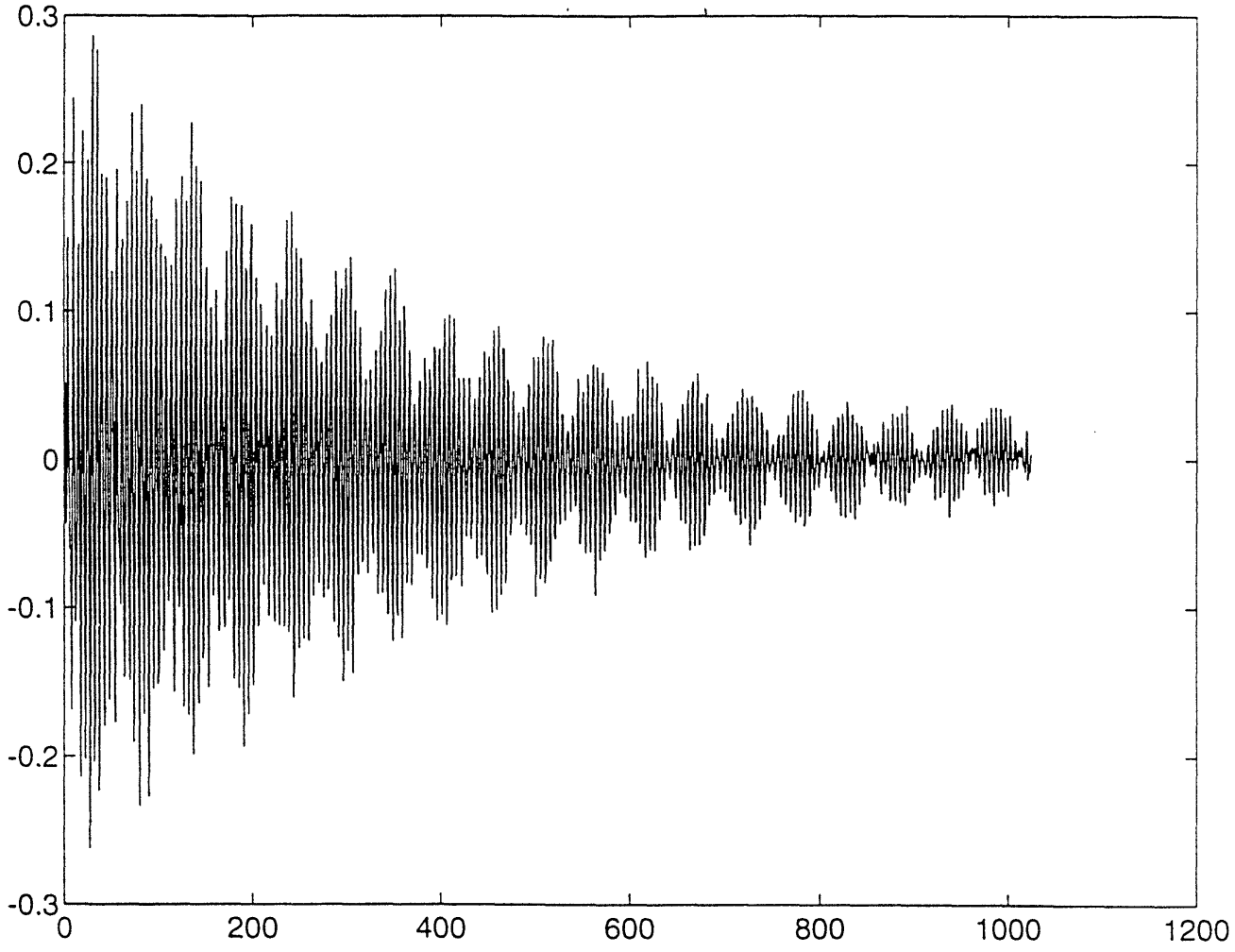

Figure 4.5 Impulse response of bad-3 point-3

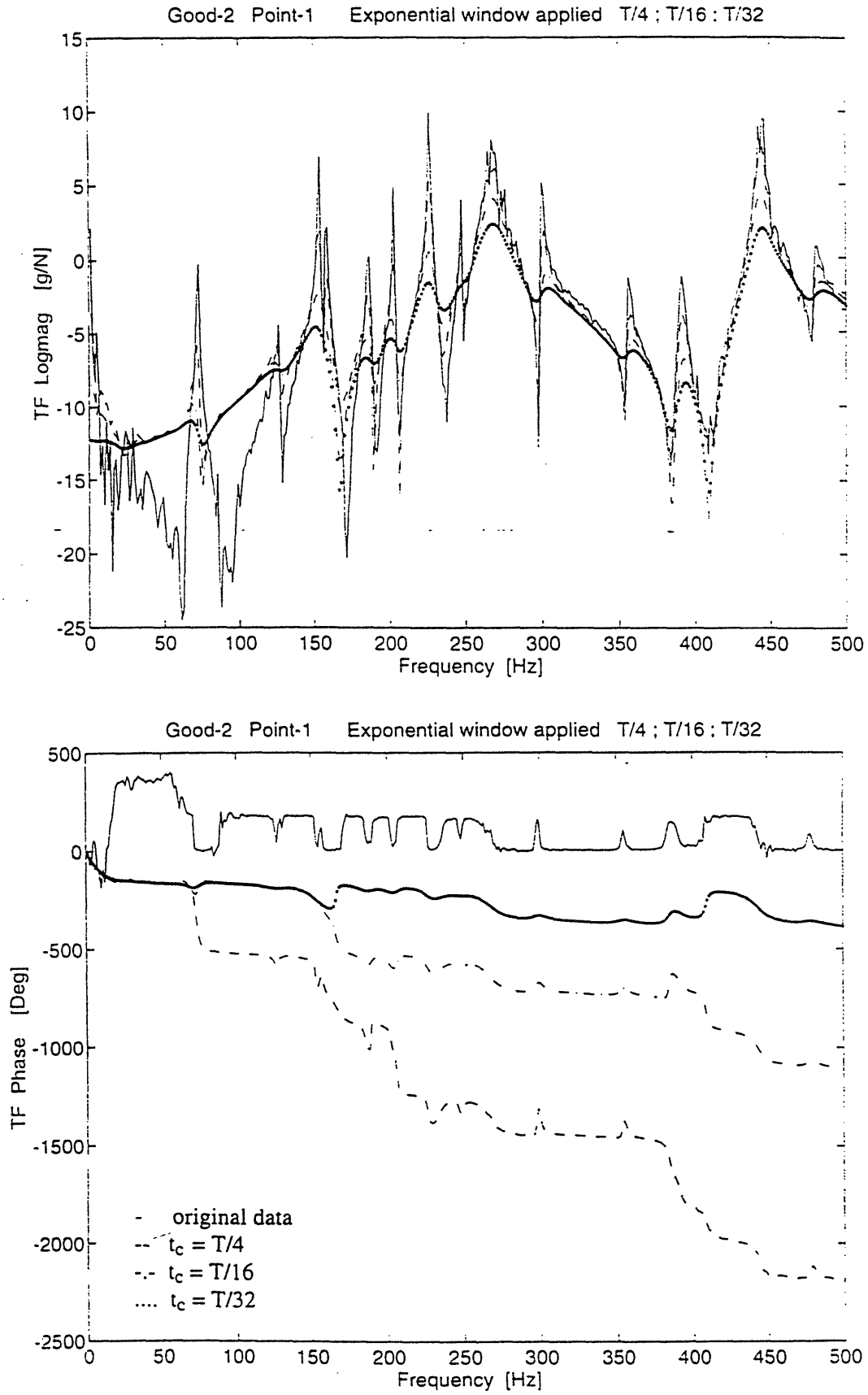

Figure 4.6 Transfer function magnitude and phase of good-2 point-1

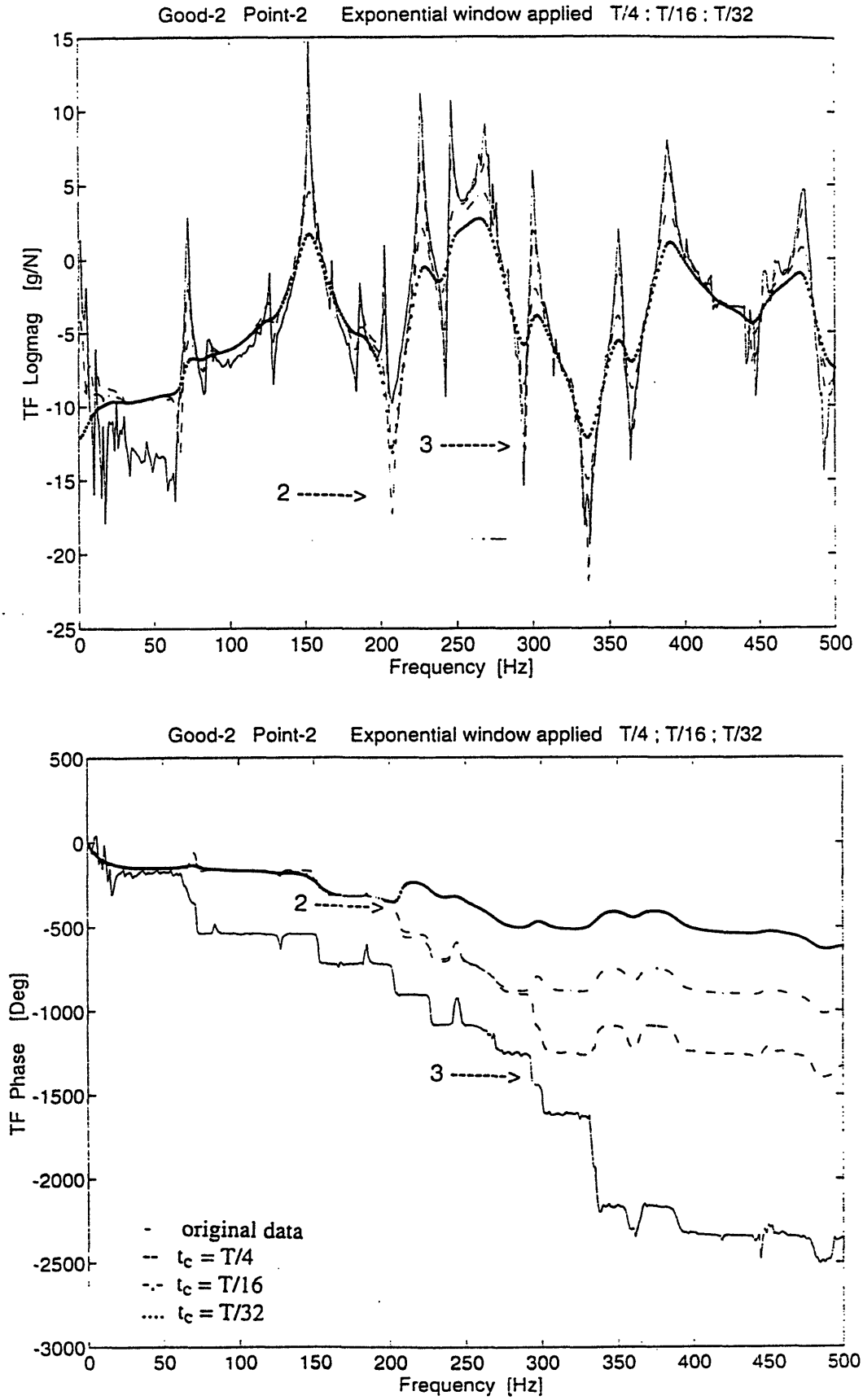

Figure 4.7 Transfer function magnitude and phase of good-2 point-2

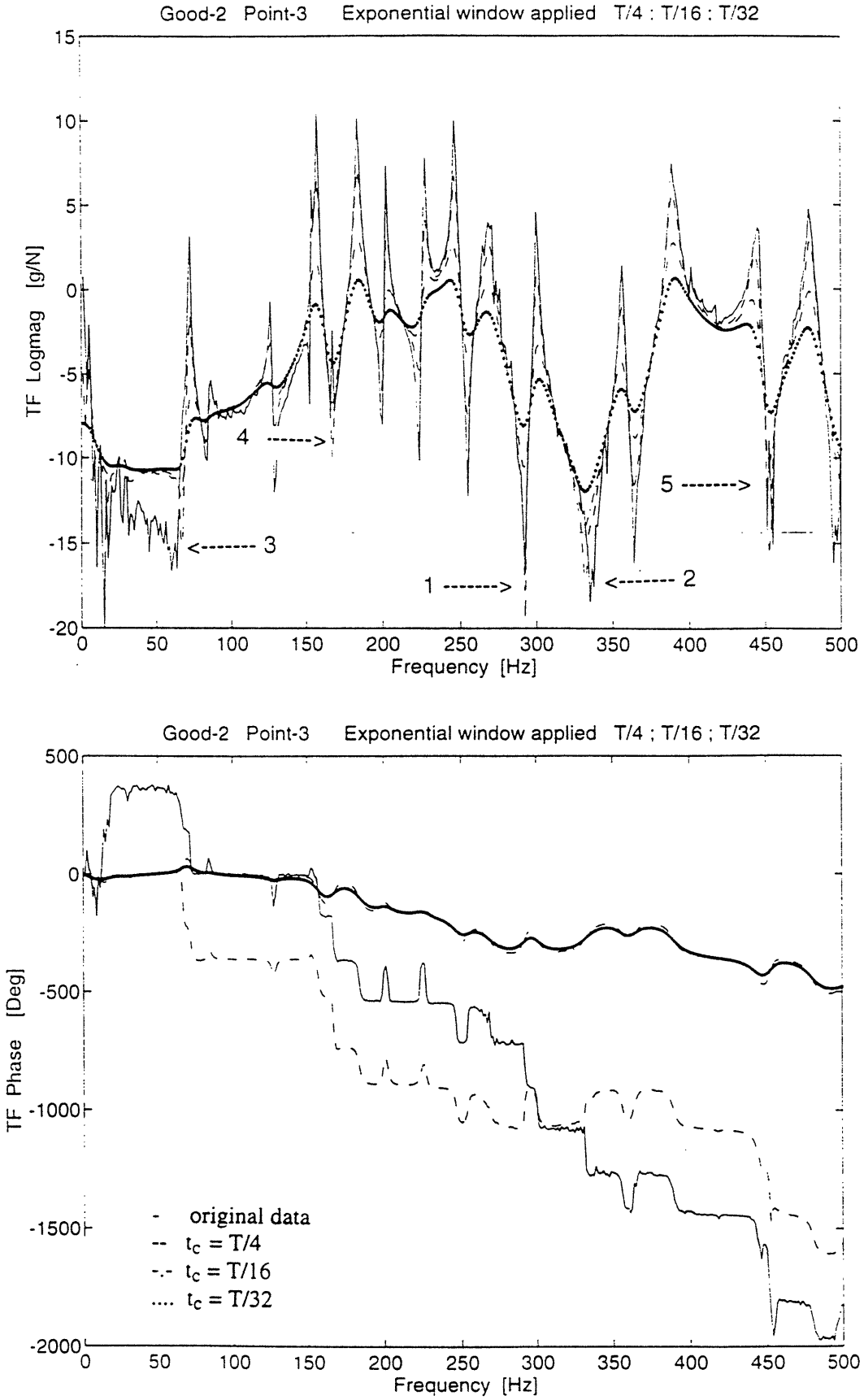

Figure 4.8 Transfer function magnitude and phase of good-2 point-3

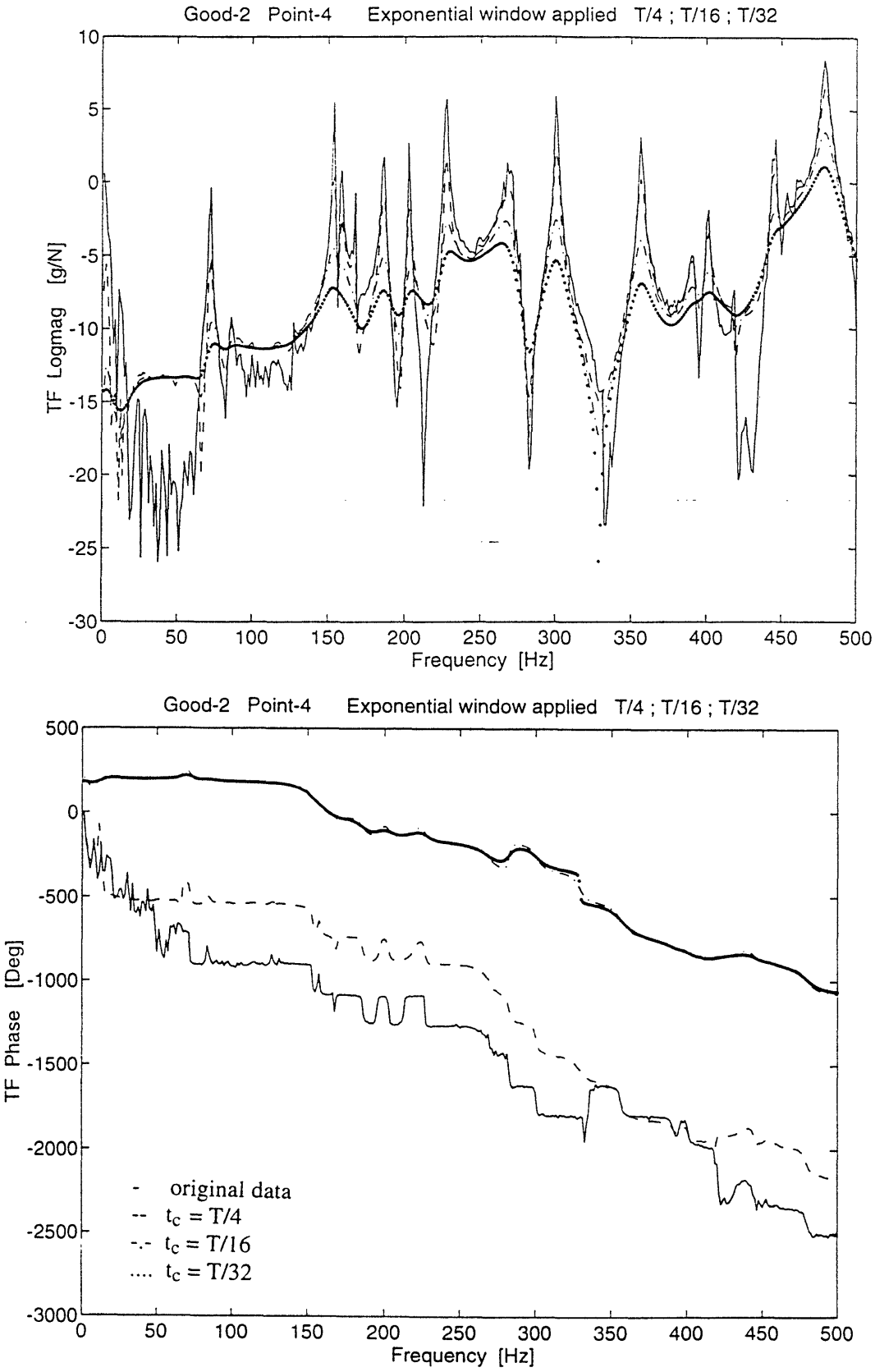

Figure 4.9 Transfer function magnitude and phase of good-2 point-4

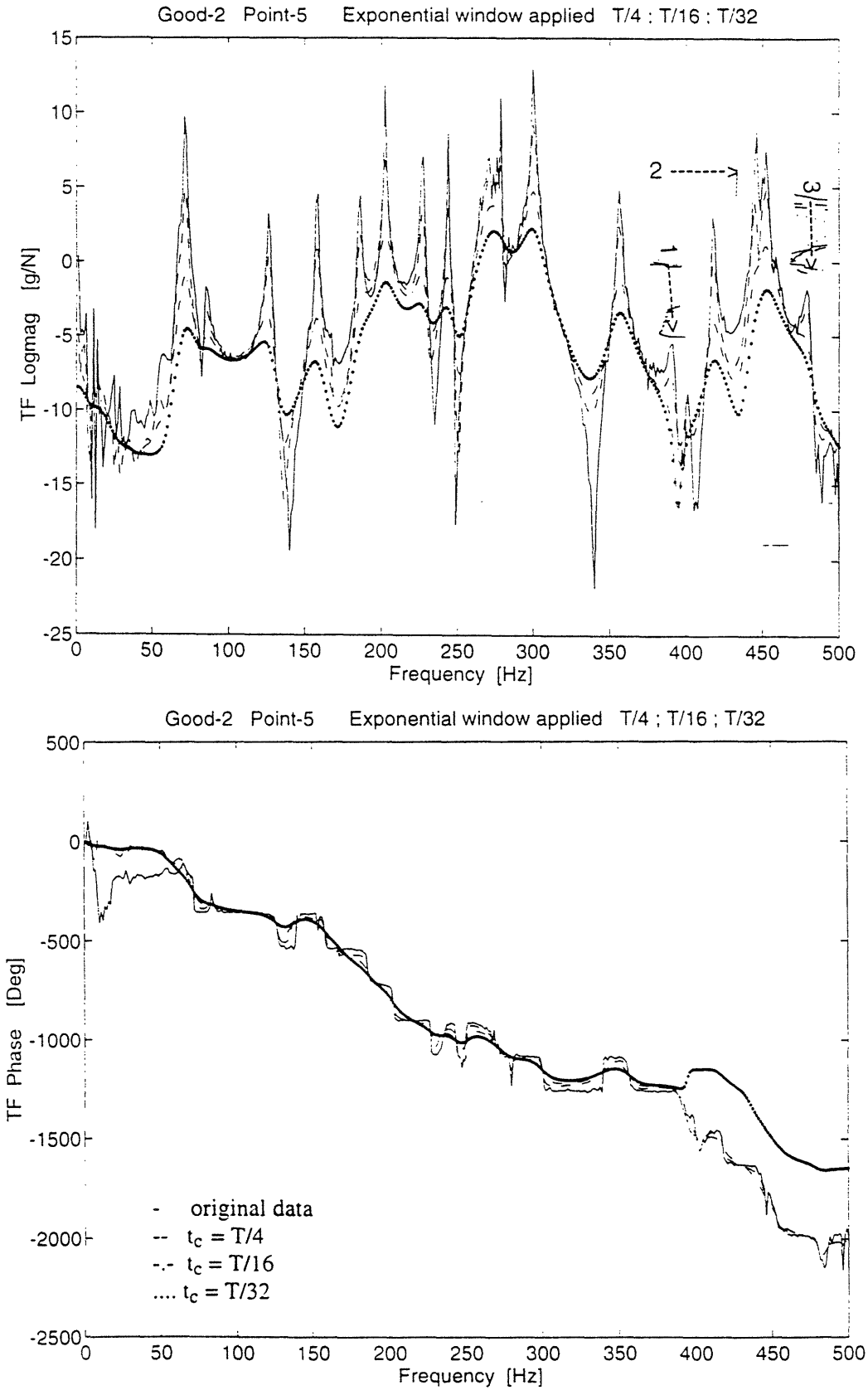

Figure 4.10 Transfer function magnitude and phase of good-2 point-5

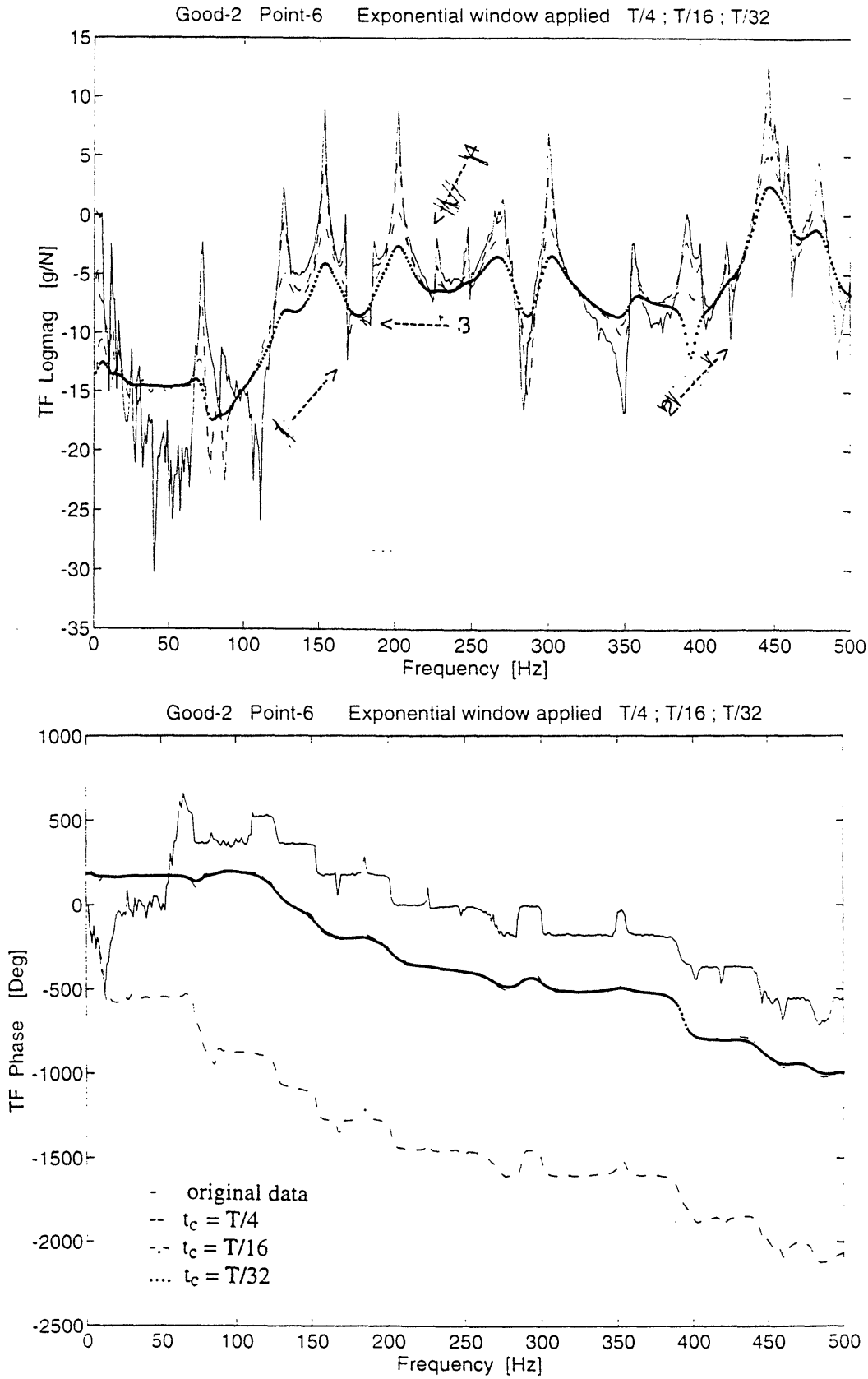

Figure 4.11 Transfer function magnitude and phase of good-2 point-6

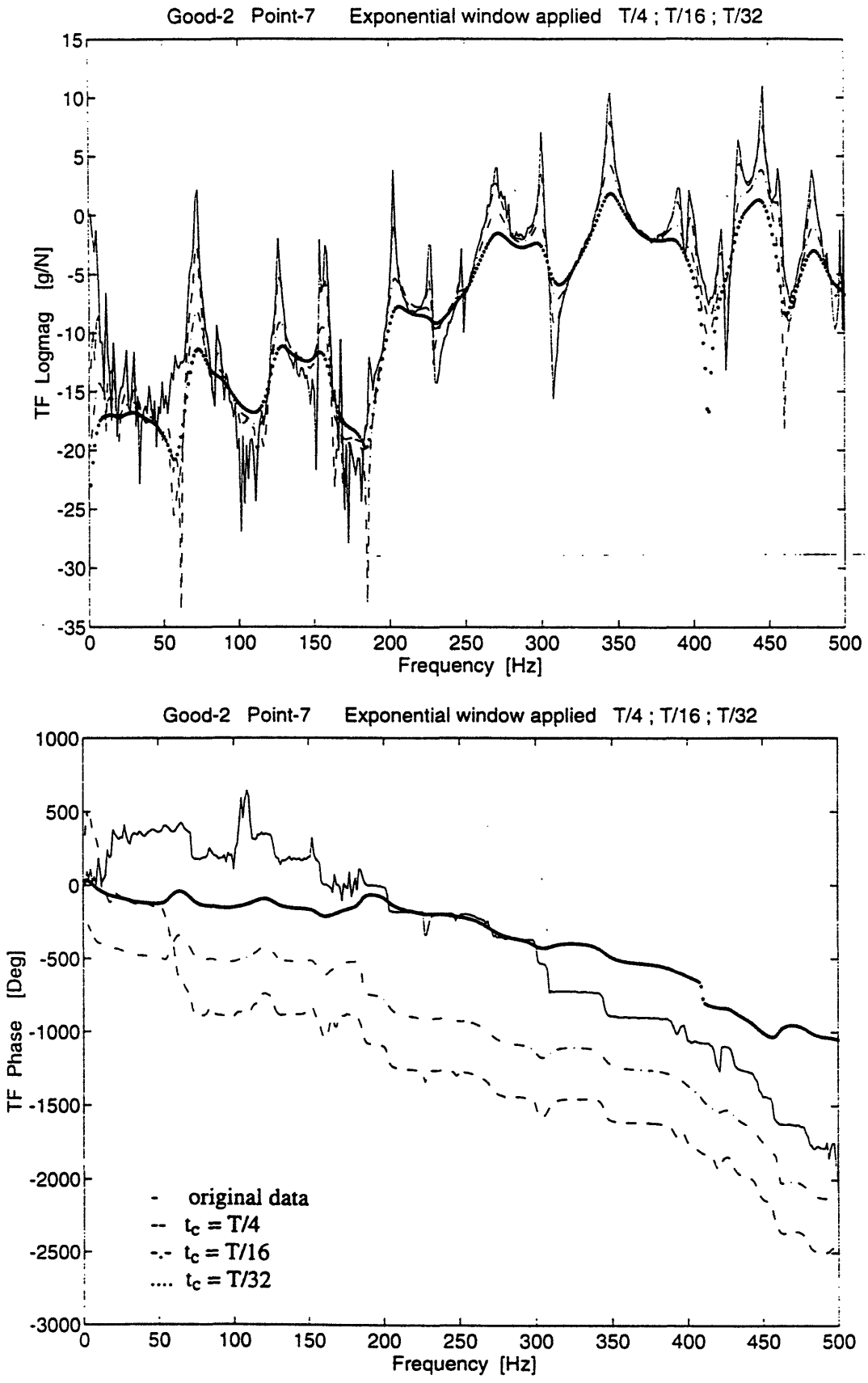

Figure 4.12 Transfer function magnitude and phase of good-2 point-7

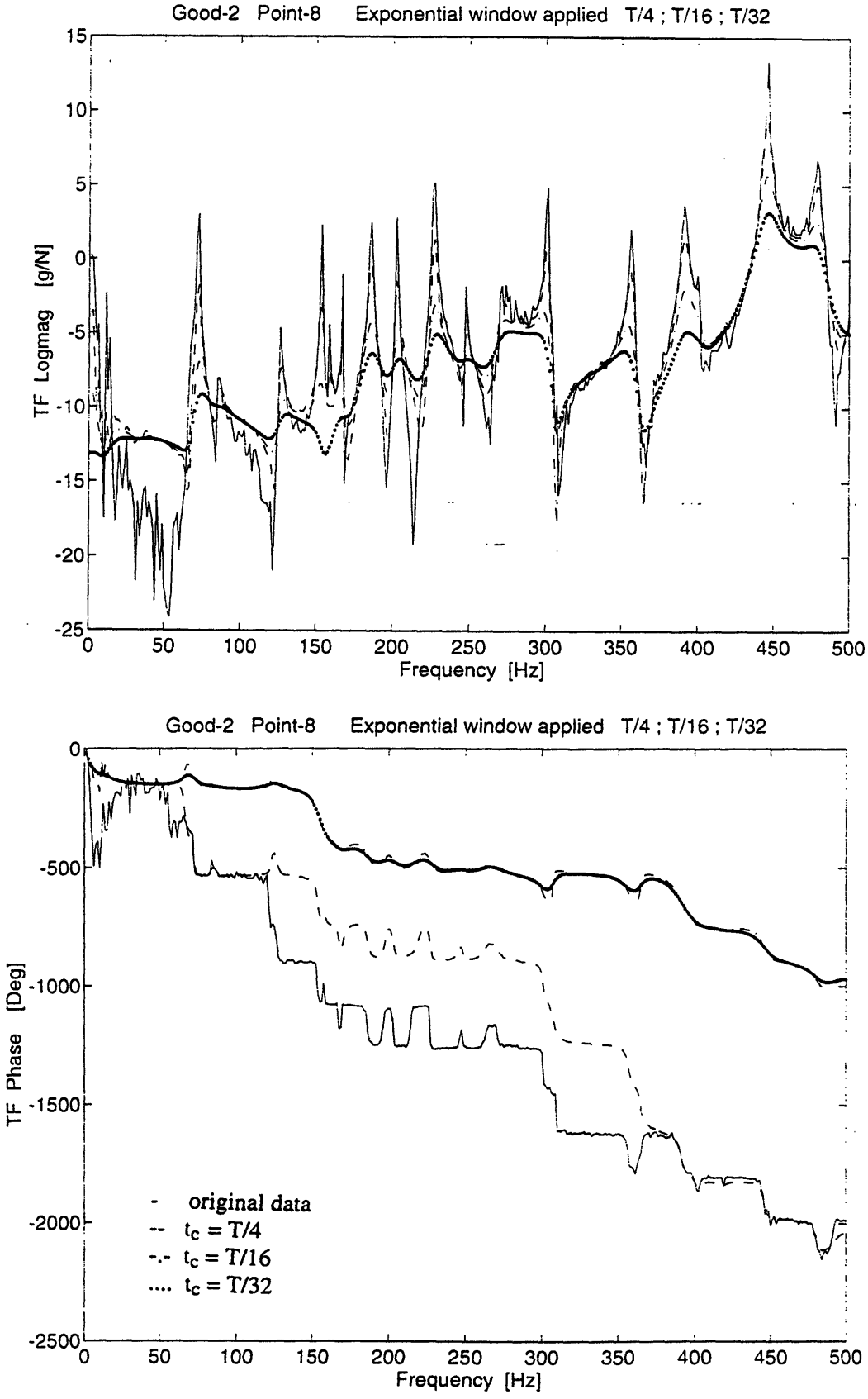

Figure 4.13 Transfer function magnitude and phase of good-2 point-8

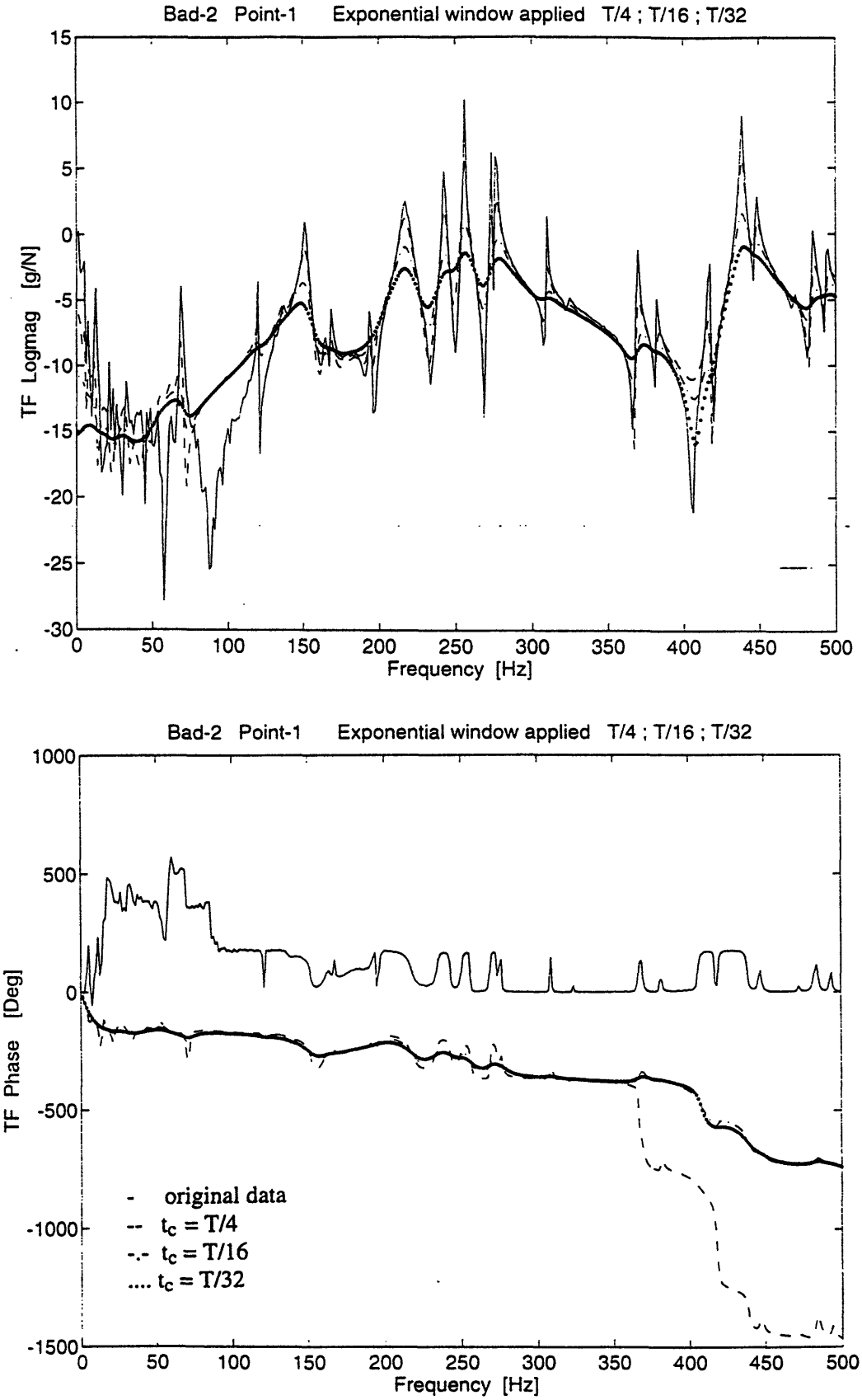

Figure 4.14 Transfer function magnitude and phase of bad-2 point-1

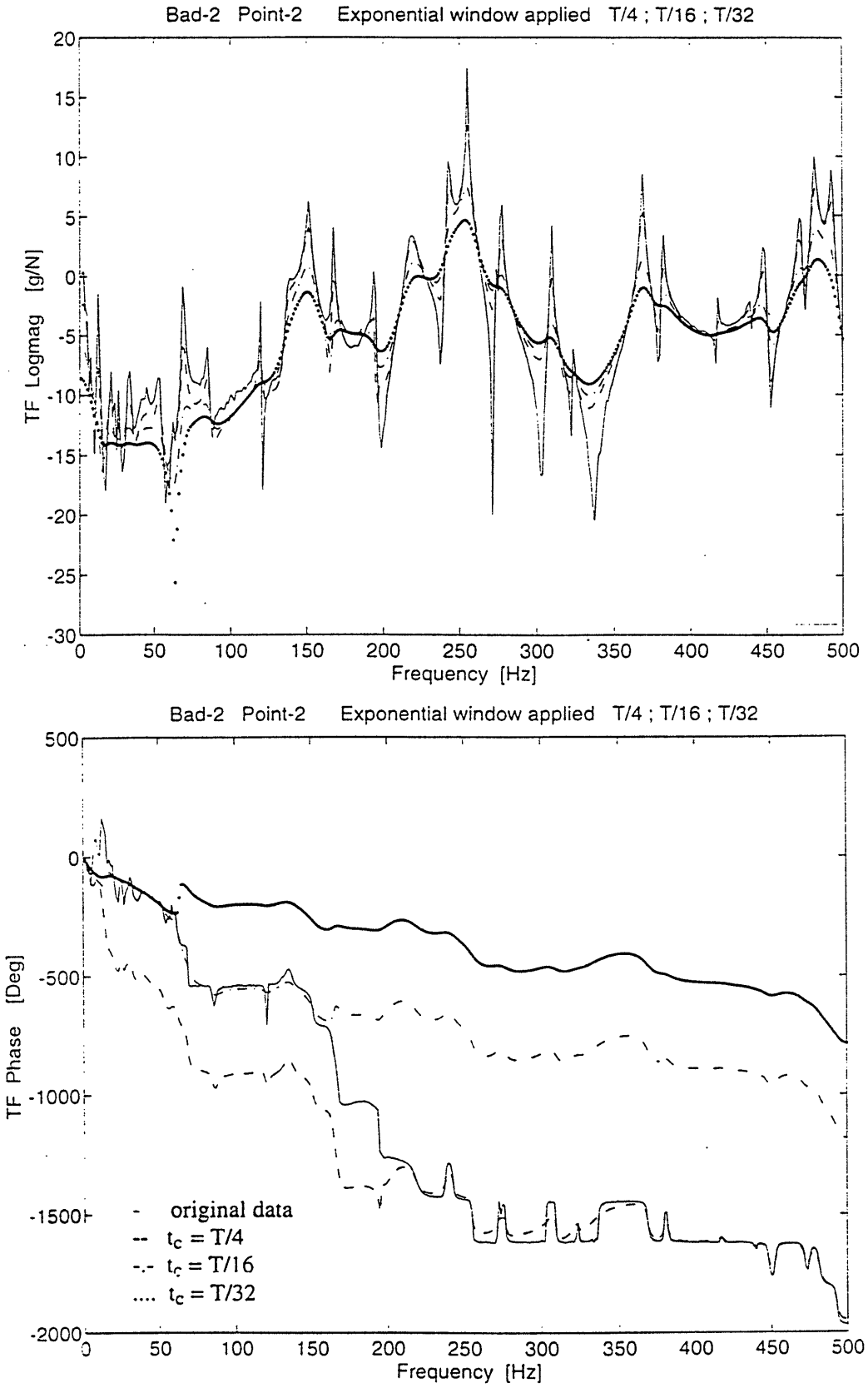

Figure 4.15 Transfer function magnitude and phase of bad-2 point-2

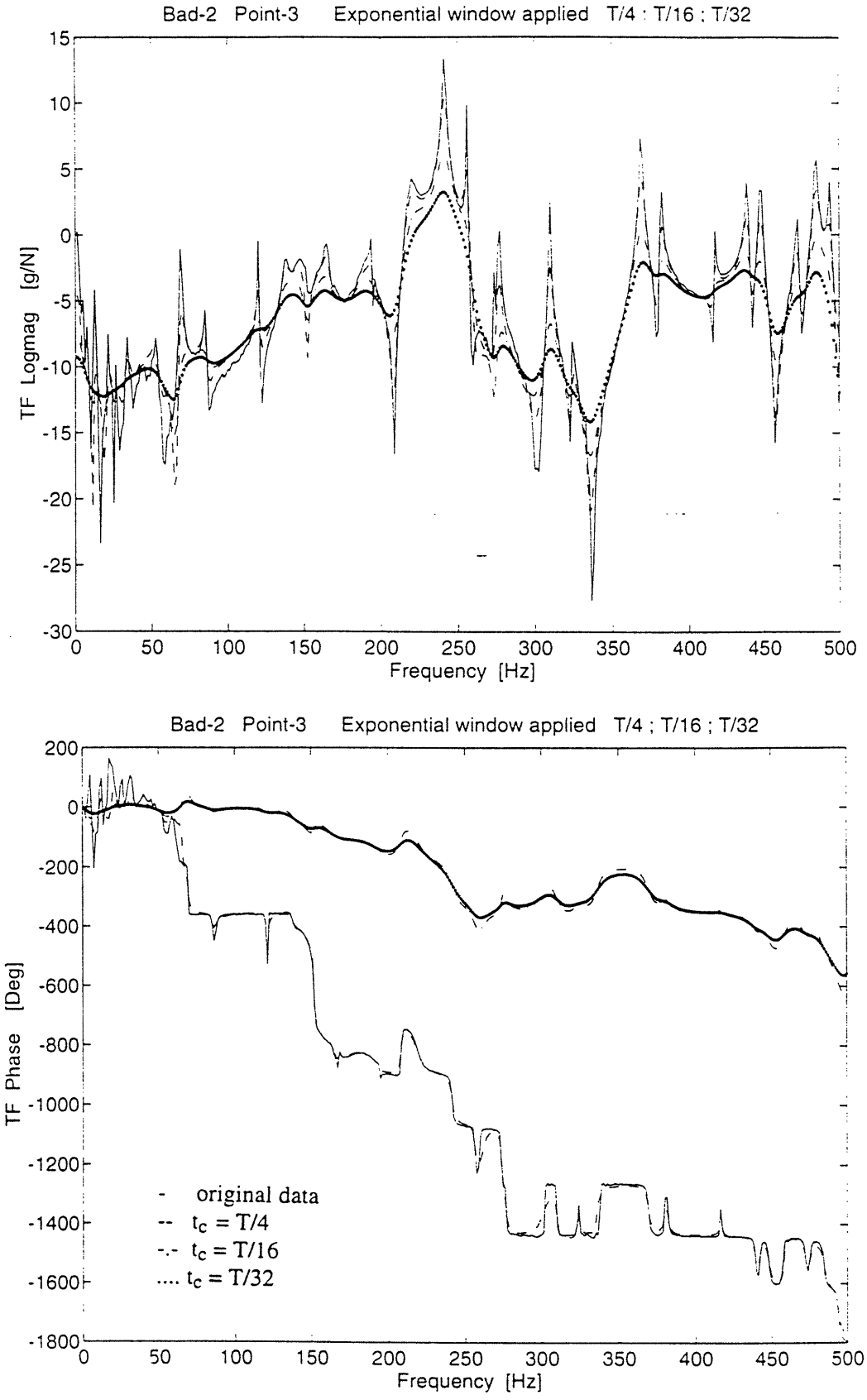

Figure 4.16 Transfer function magnitude and phase of bad-2 point-3

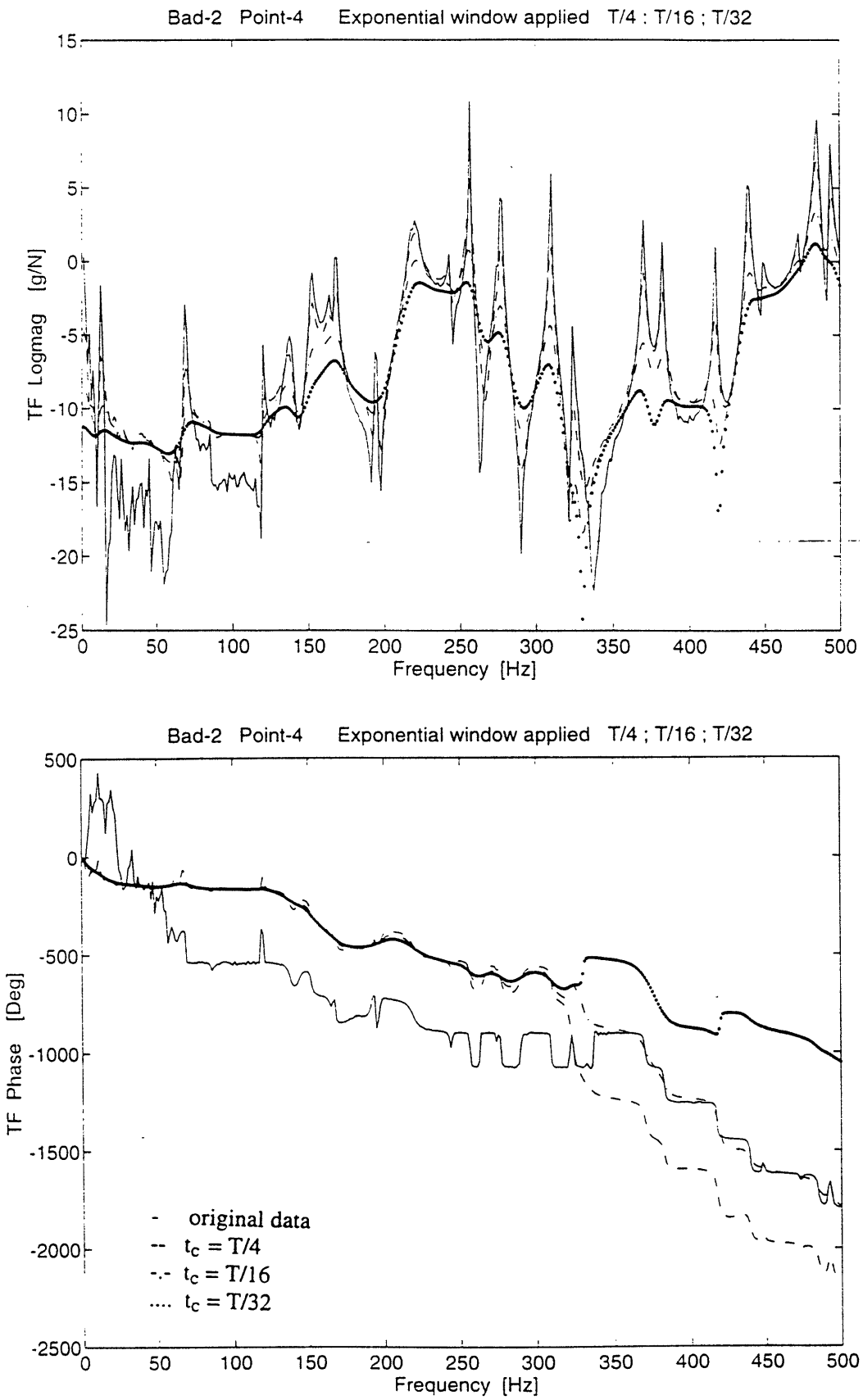

Figure 4.17 Transfer function magnitude and phase of bad-2 point-4

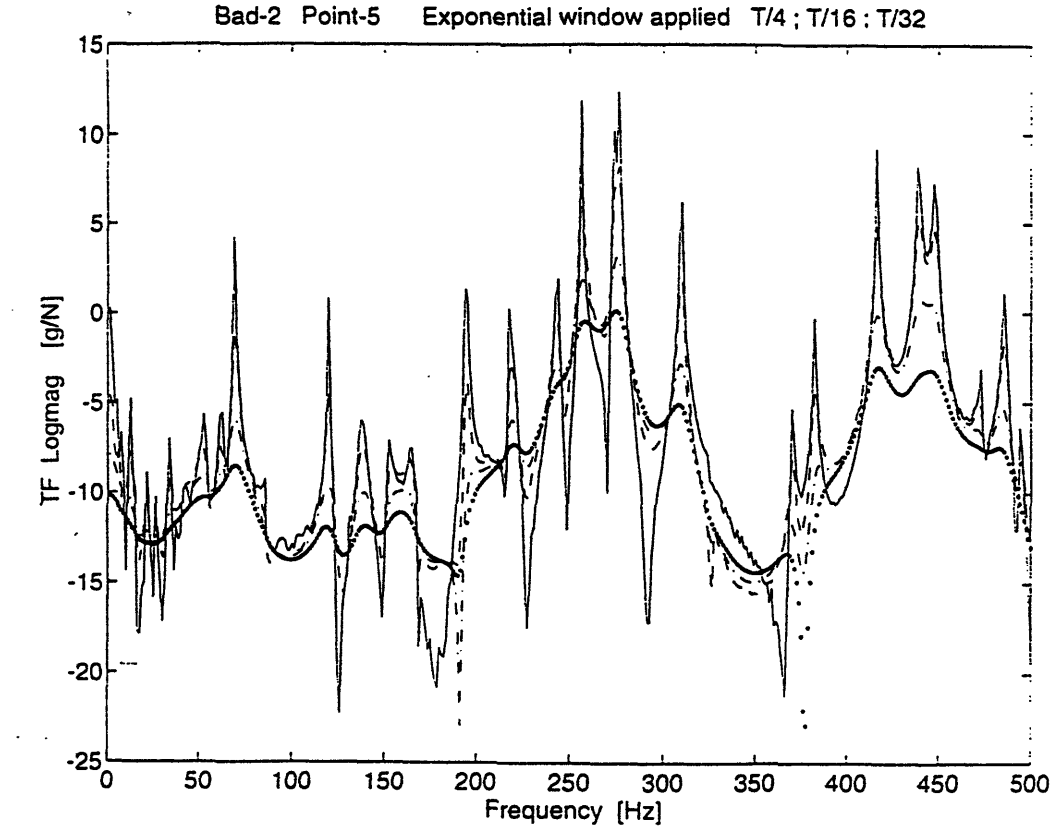

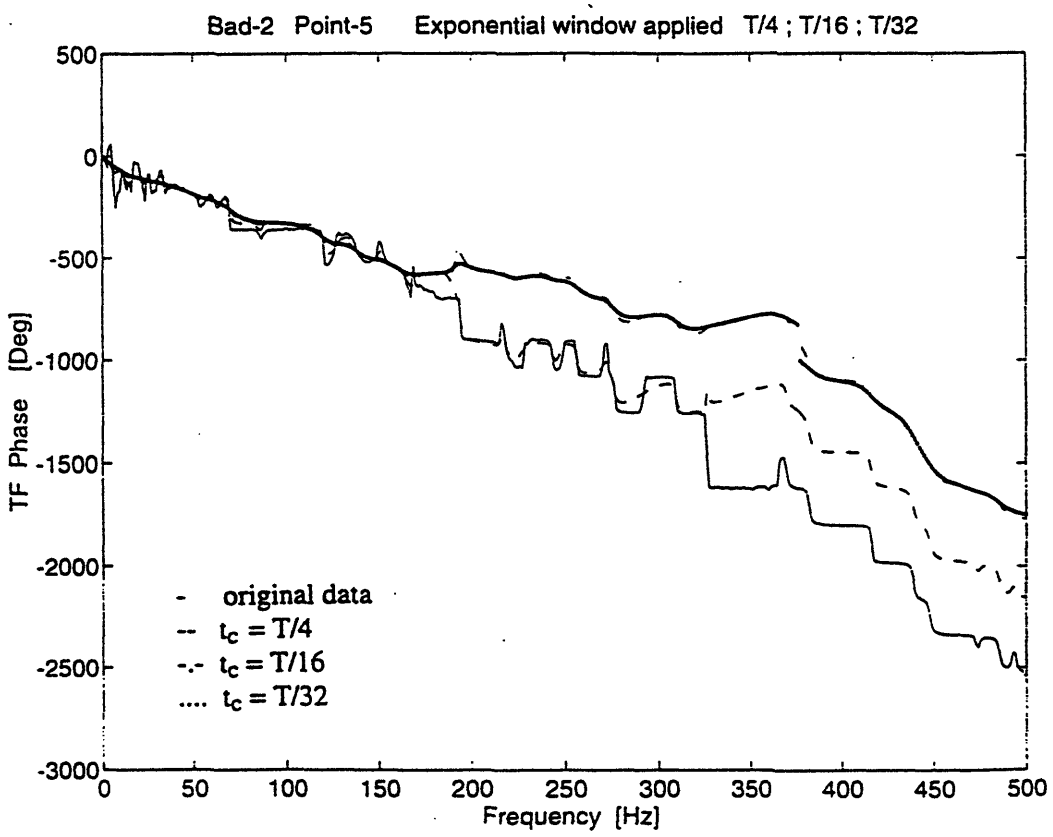

Figure 4.18 Transfer function magnitude and phase of bad-2 point-5

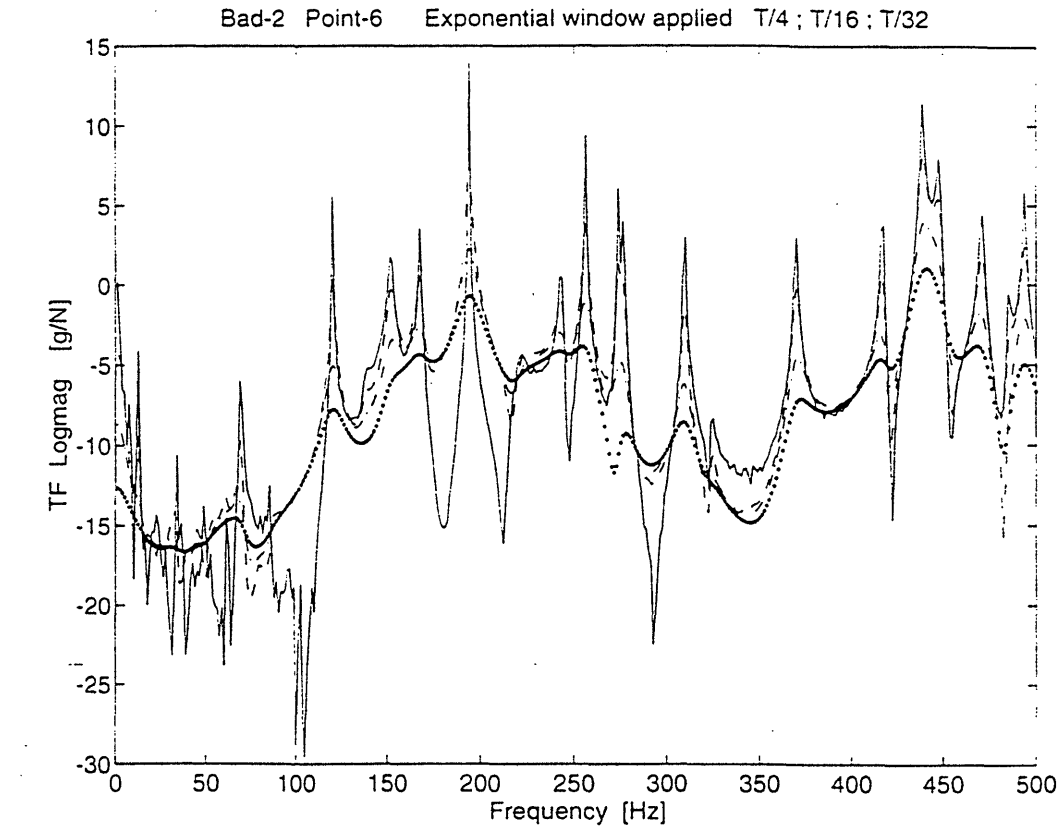

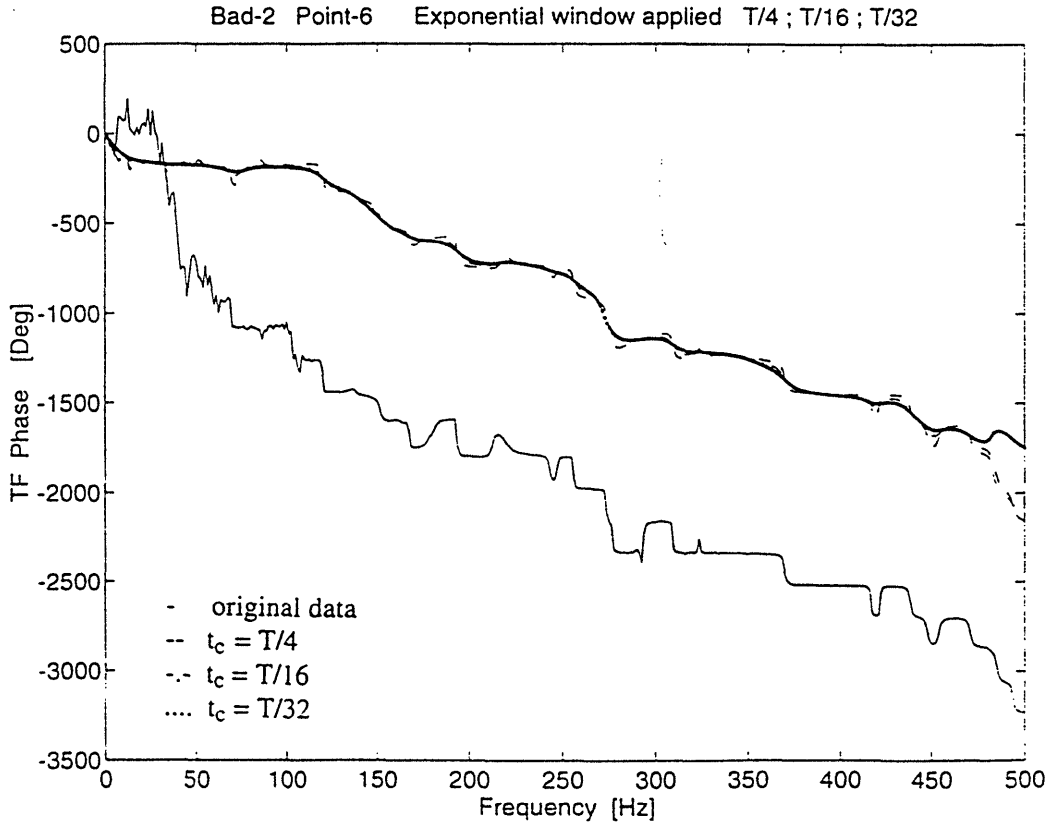

Figure 4.19 Transfer function magnitude and phase of bad-2 point-6

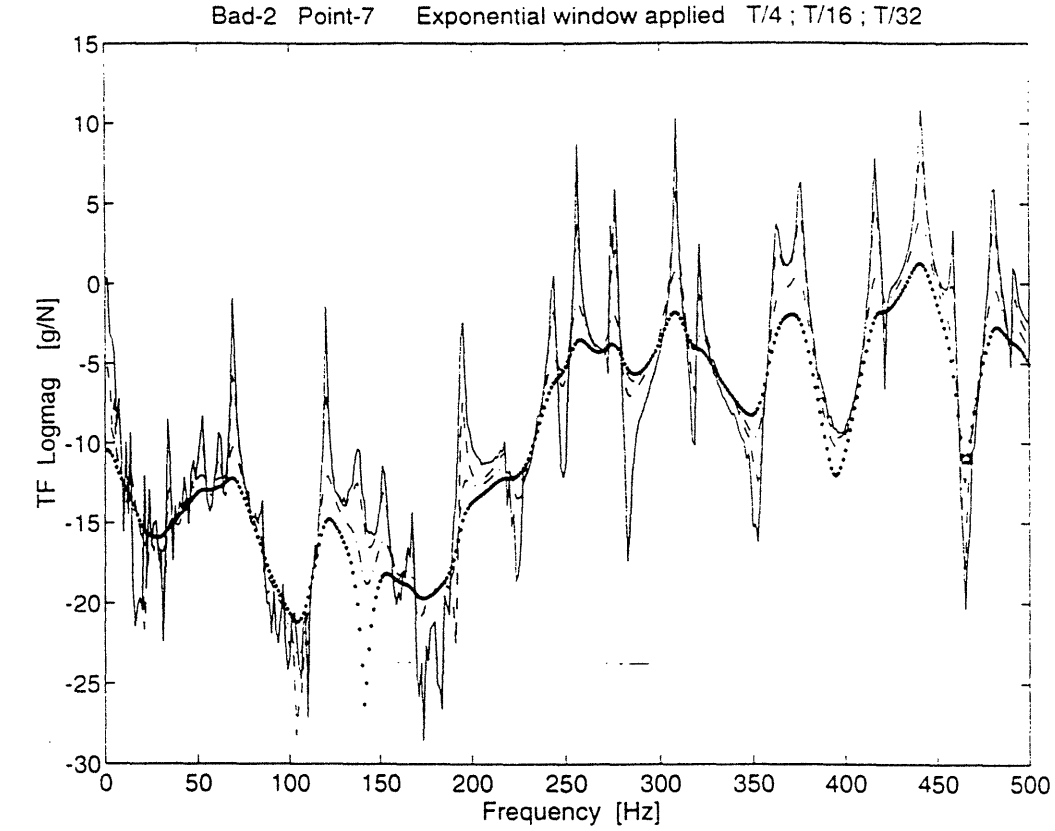

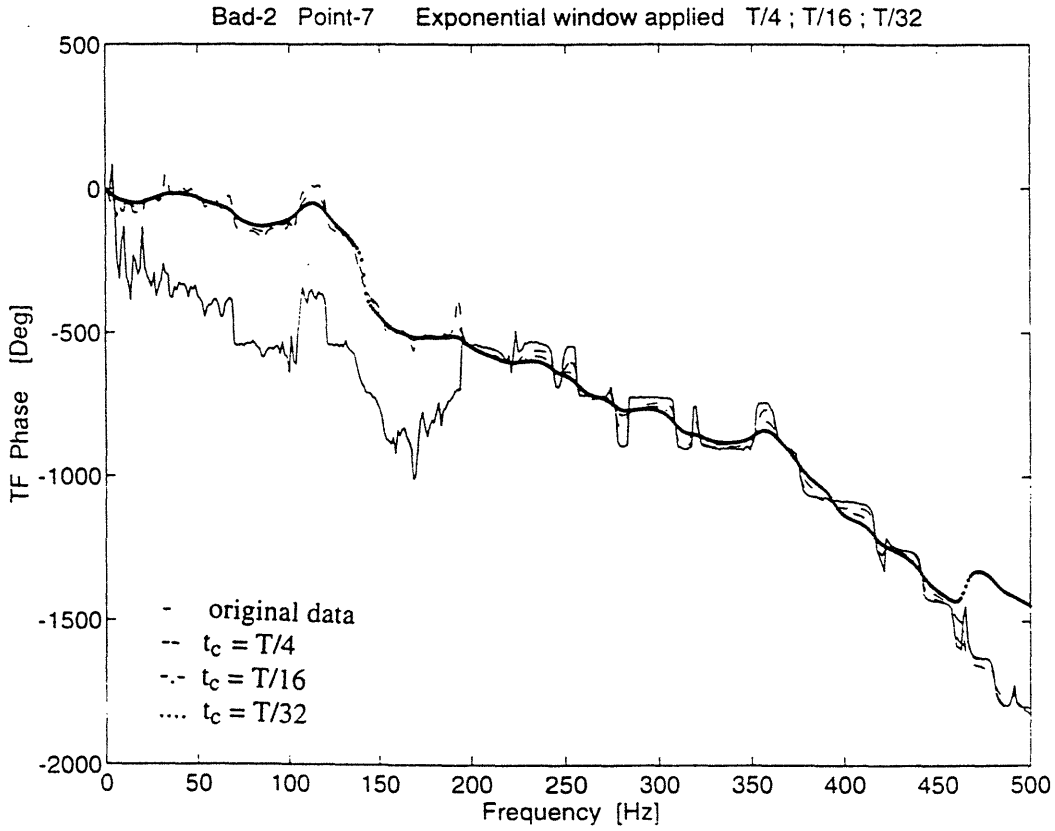

Figure 4.20 Transfer function magnitude and phase of bad-2 point-7

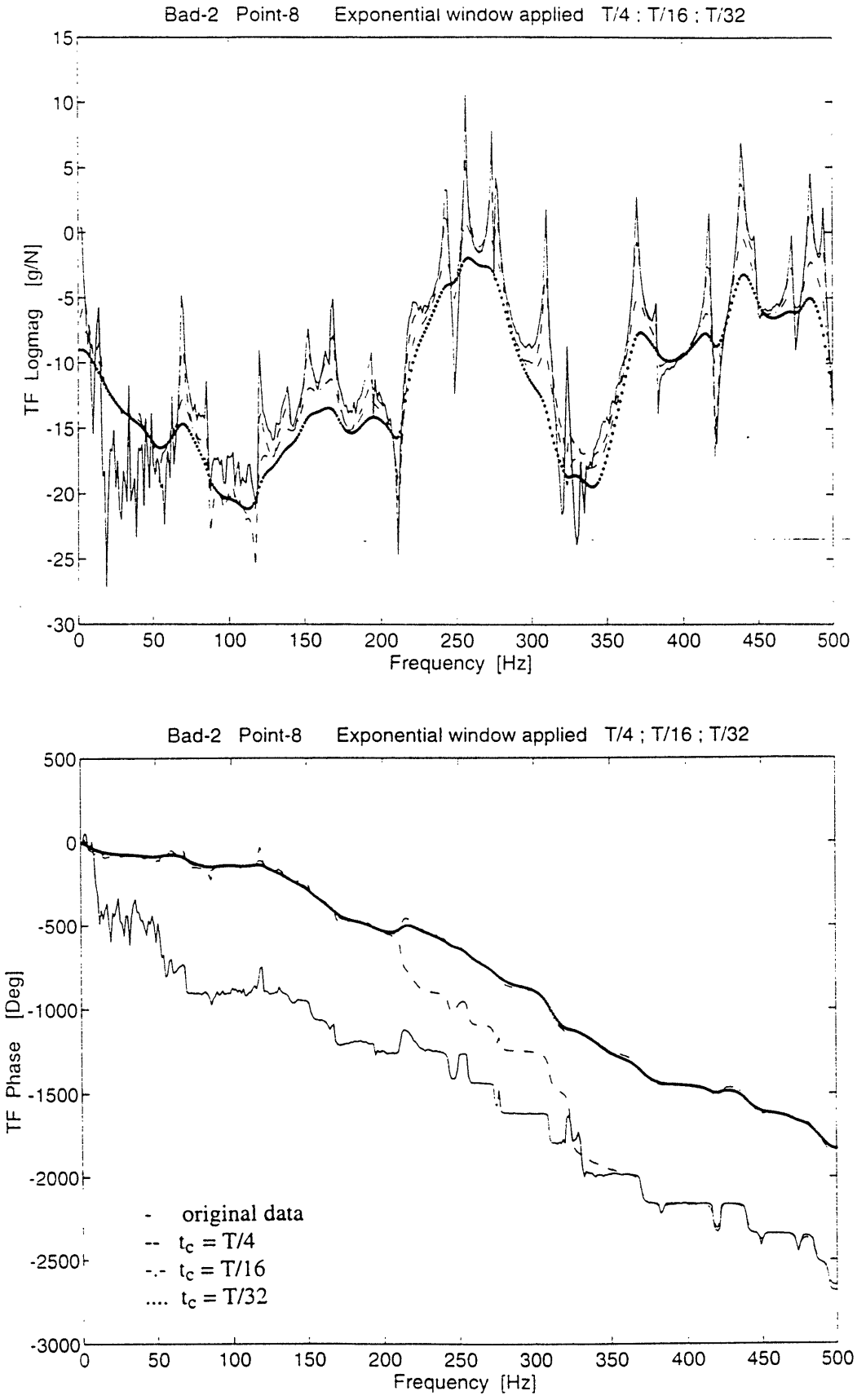

Figure 4.21 Transfer function magnitude and phase of bad-2 point-8

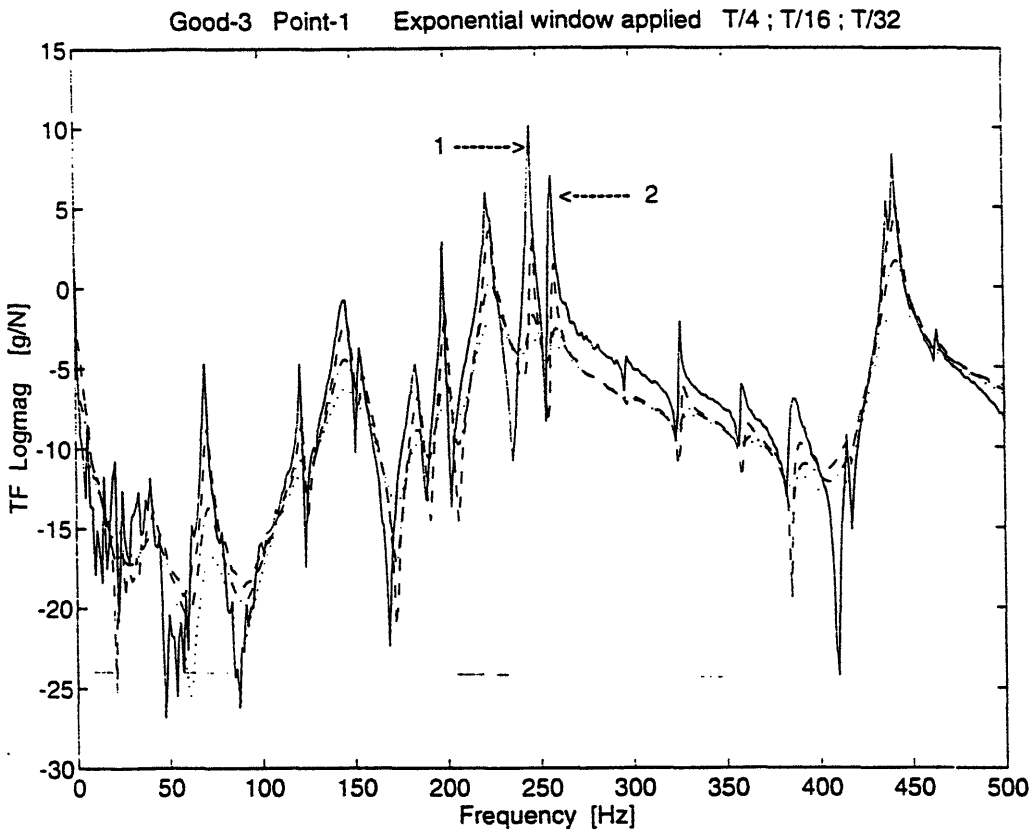

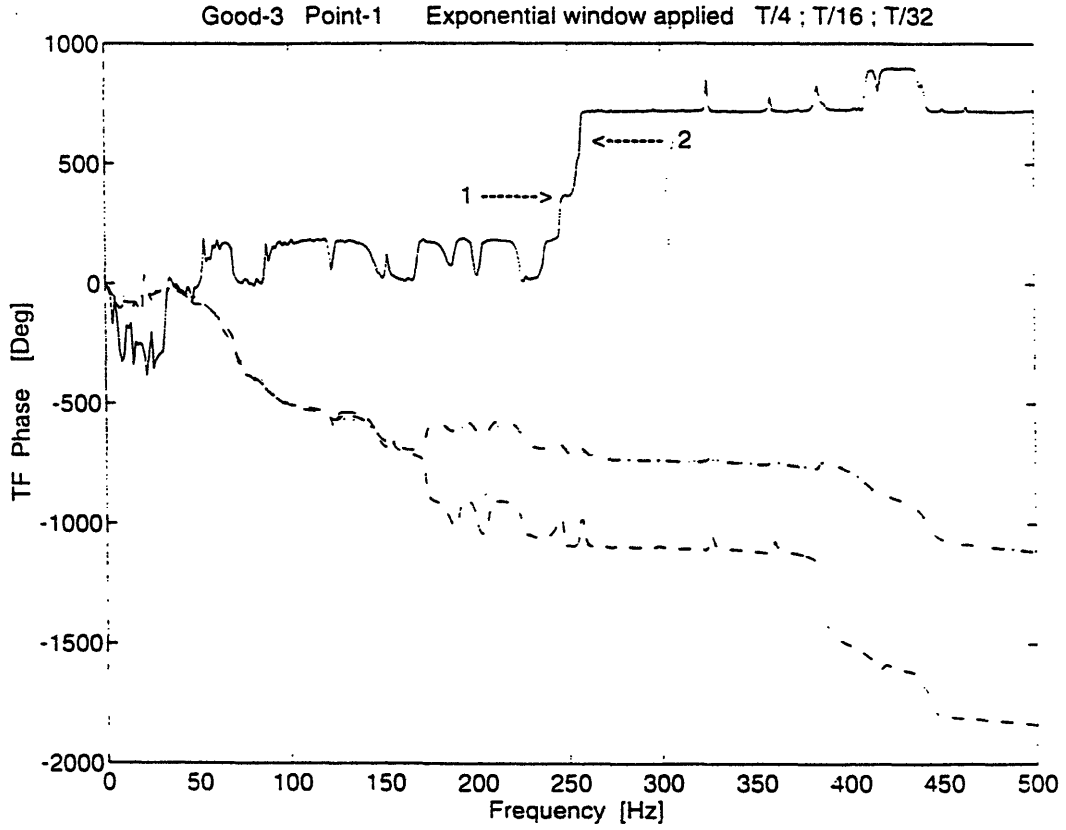

Figure 4.22 Transfer function magnitude and phase of good-3 point-1

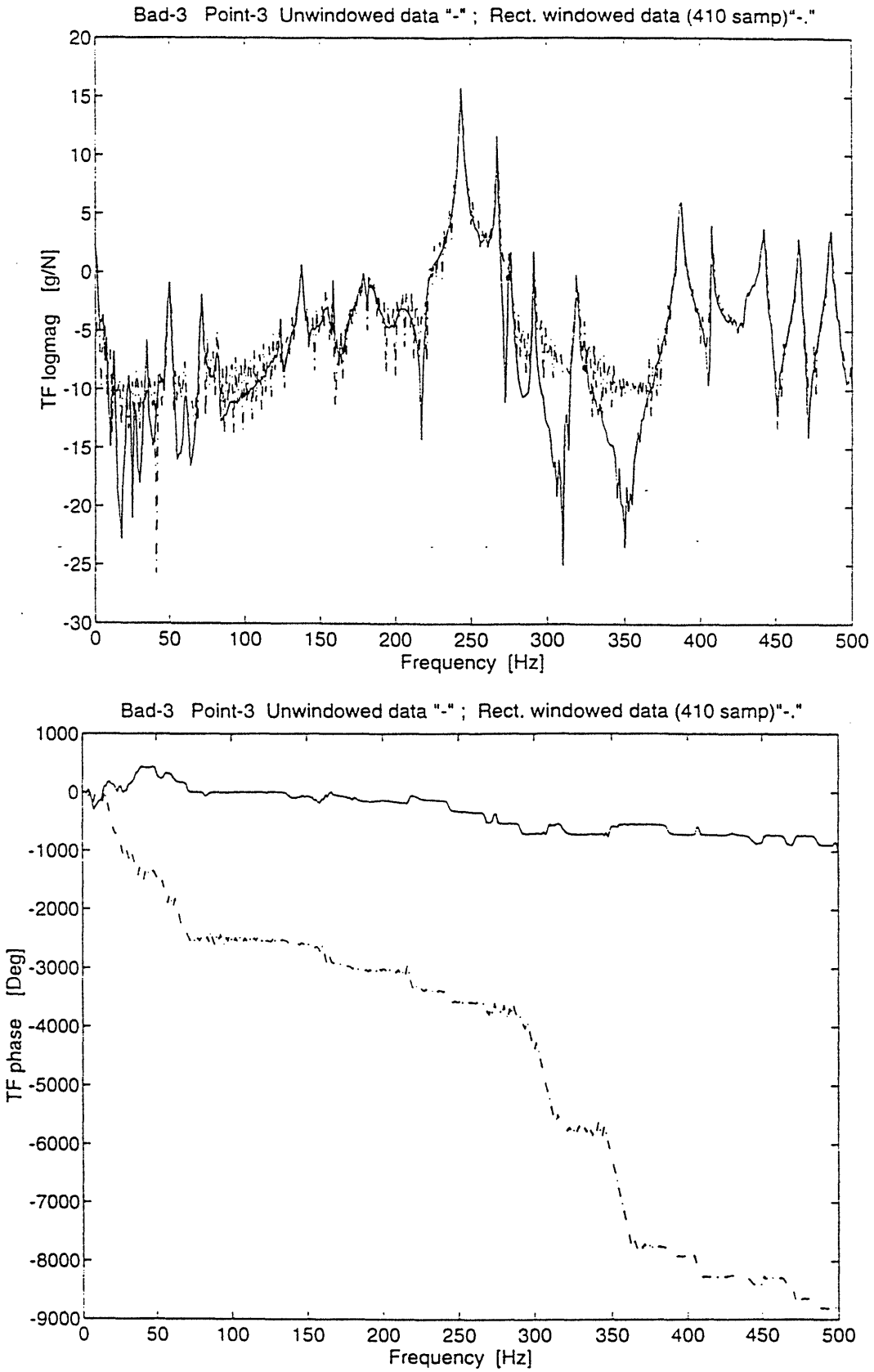

Figure 4.23 Comparison of magnitude and phase of truncated (410 samples) and original impulse response (1024 samples) : bad-3 point-3

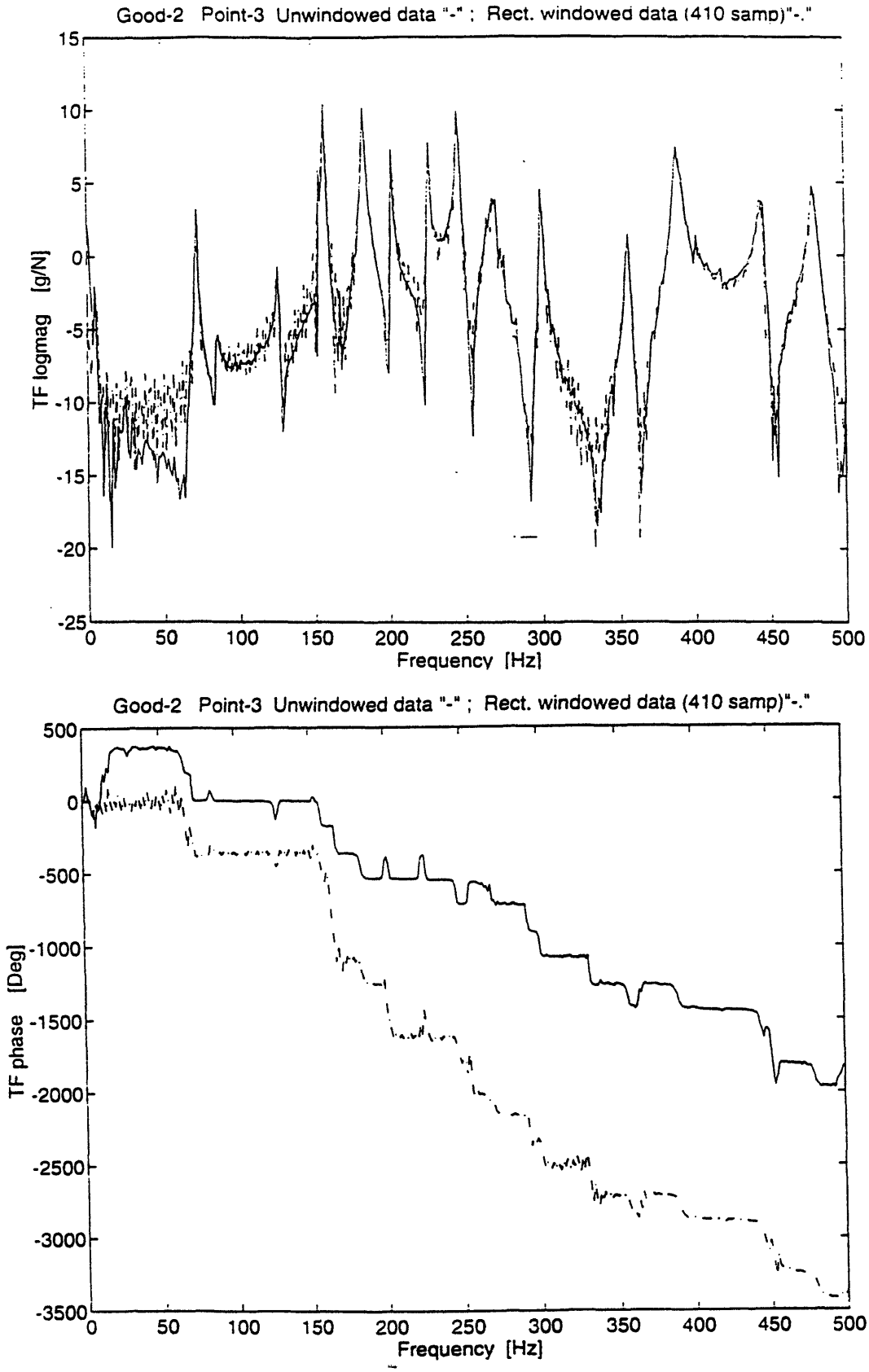

Figure 4.24 Comparison of magnitude and phase of truncated (410 samples) and original impulse response (1024 samples) : good-2 point-3

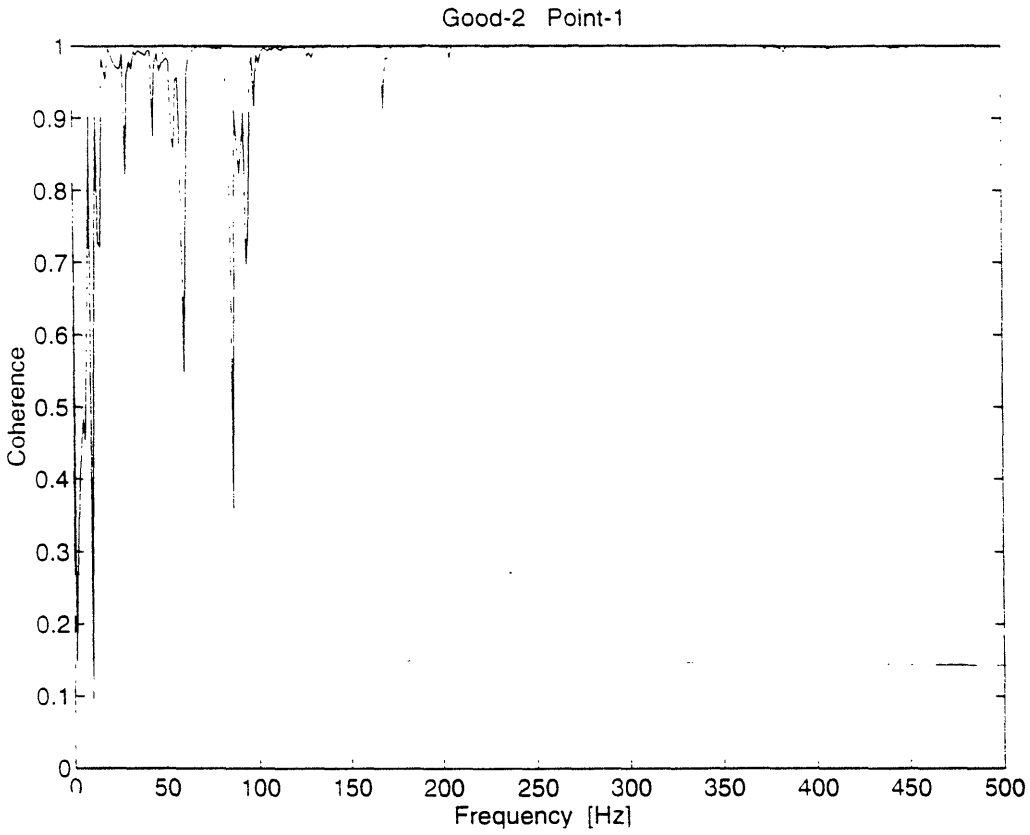

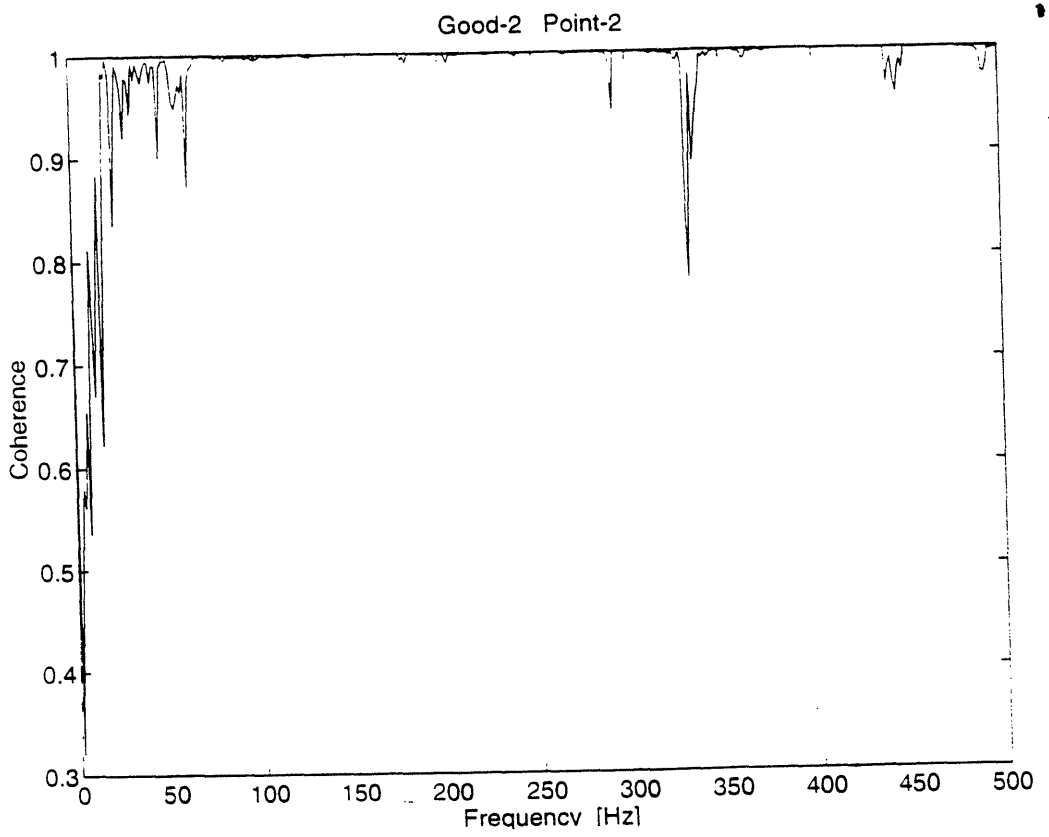

Figure 4.25 Coherence plot of good-2 point-1 and good-2 point-2

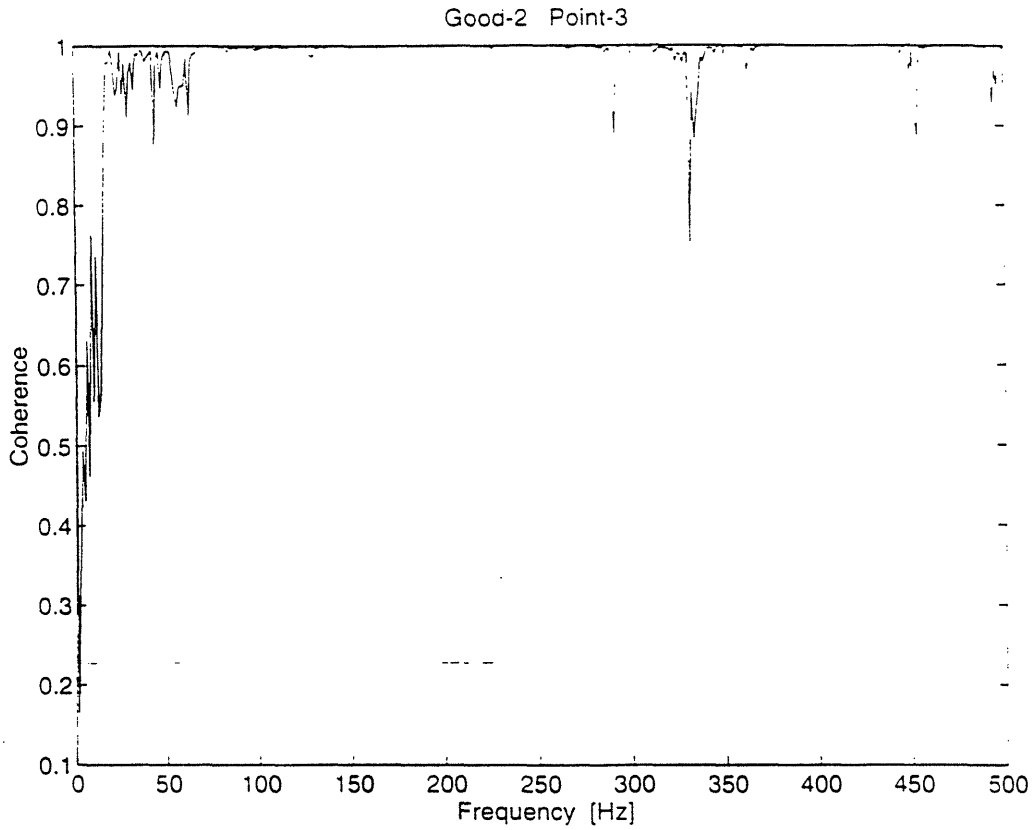

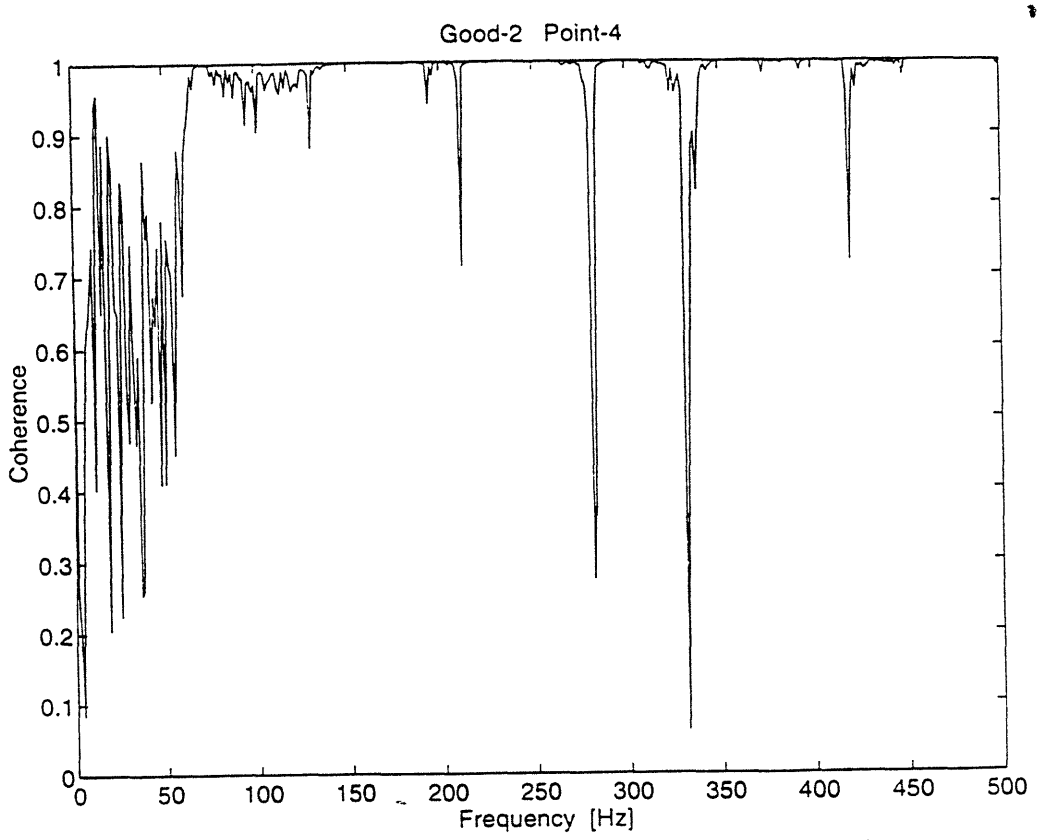

Figure 4.26 Coherence plot of good-2 point-3 and good-2 point-4

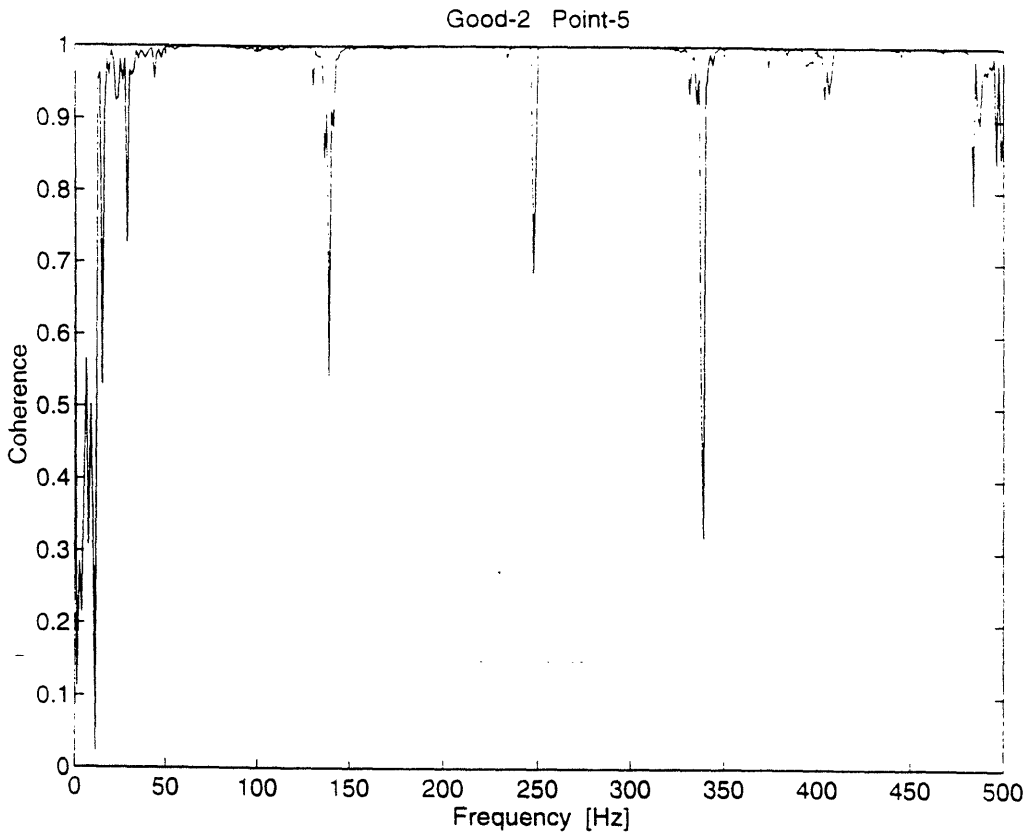

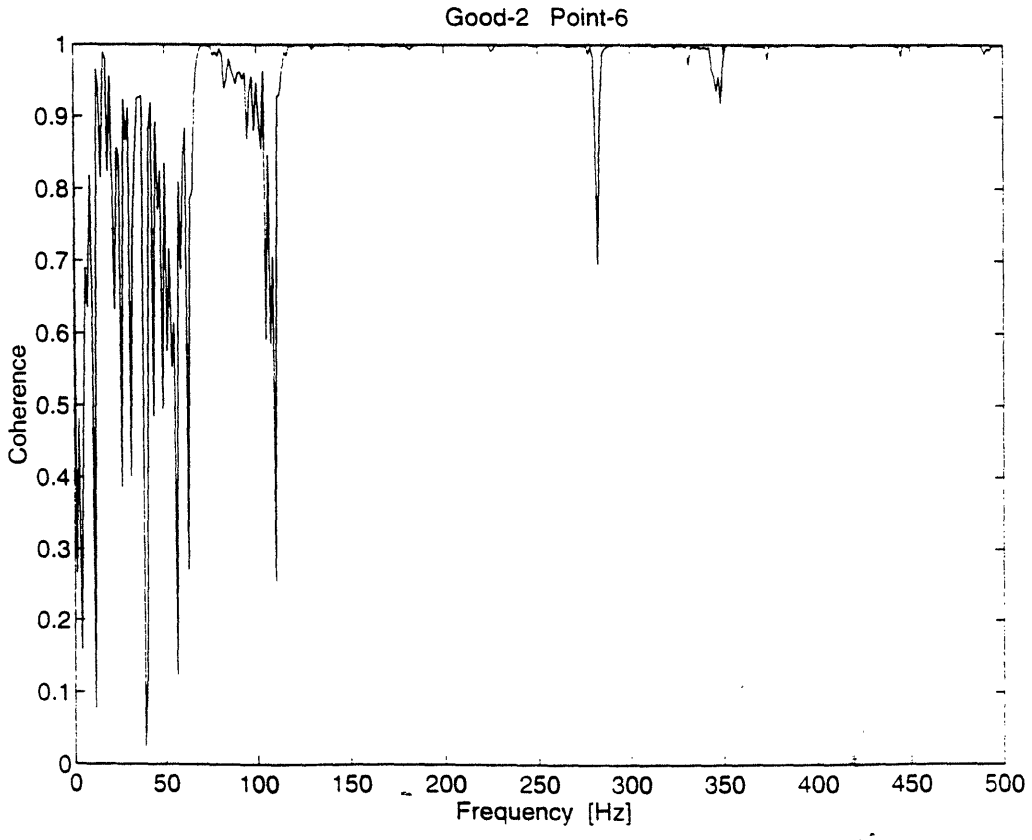

Figure 4.27 Coherence plot of good-2 point-5 and good-2 point-6

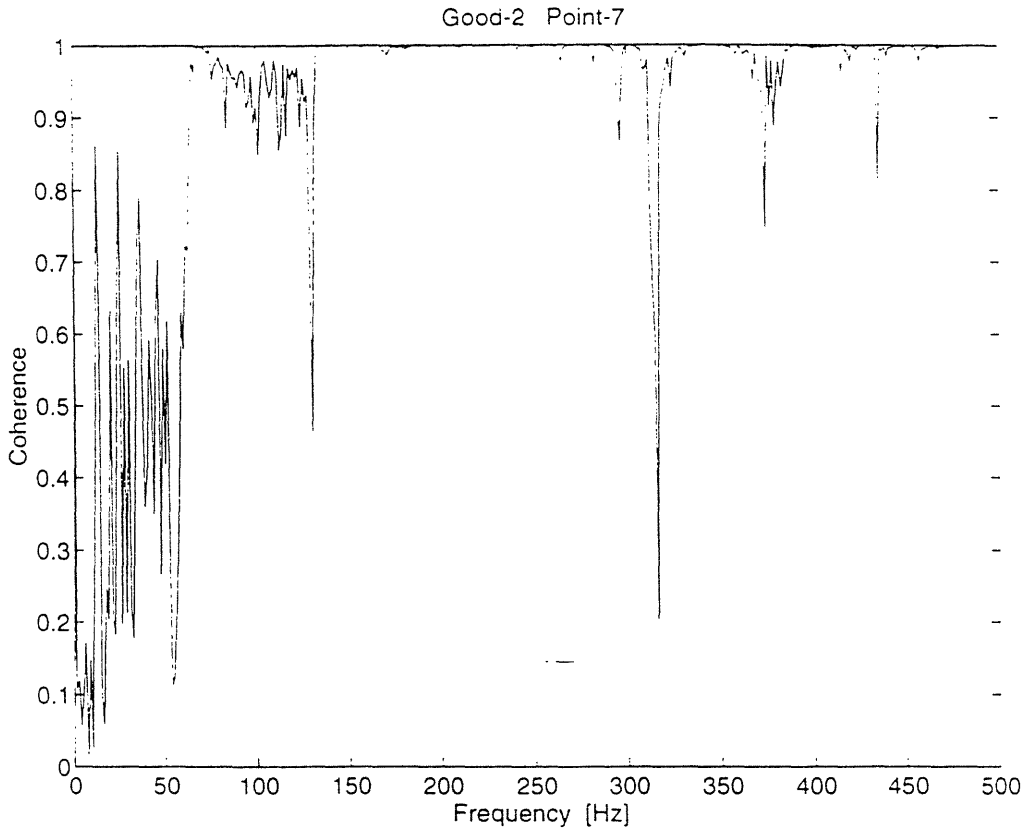

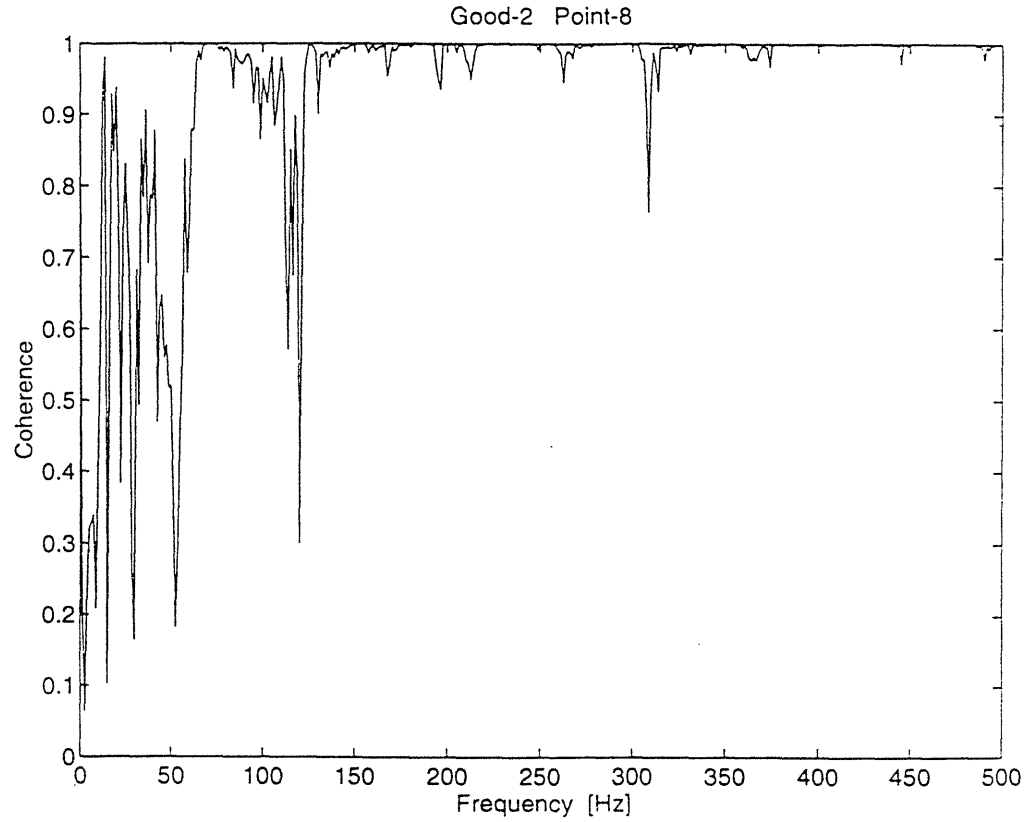

Figure 4.28 Coherence plot of good-2 point-7 and good-2 point-8

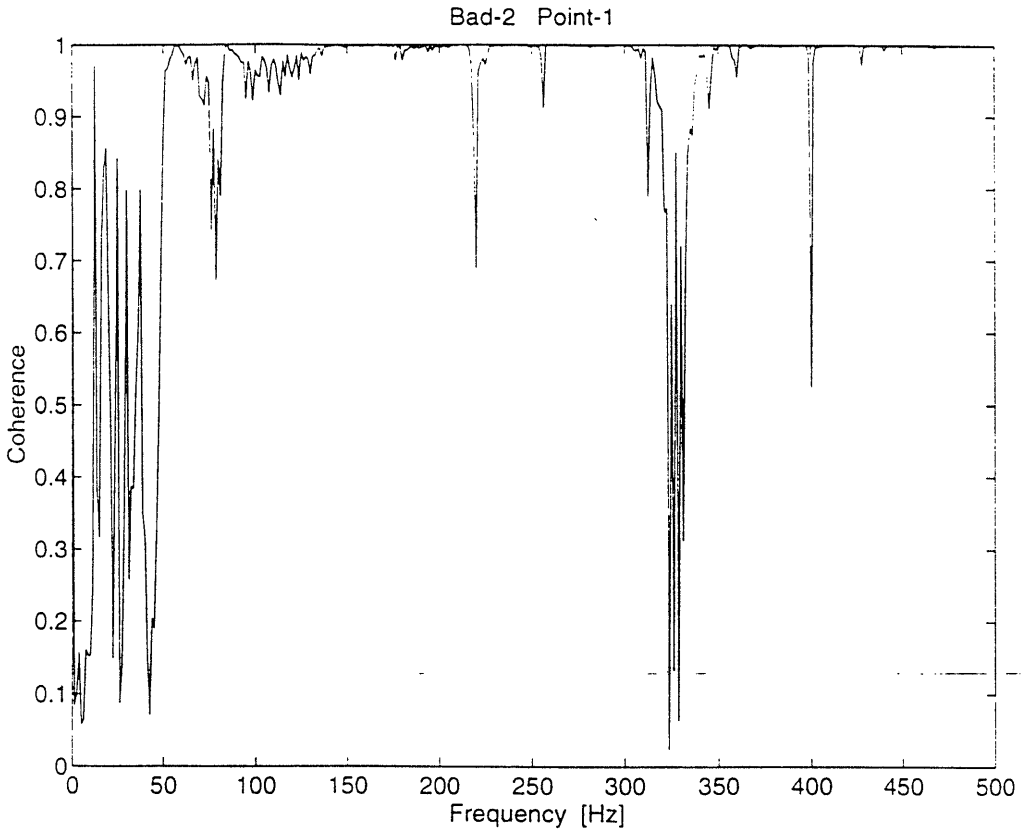

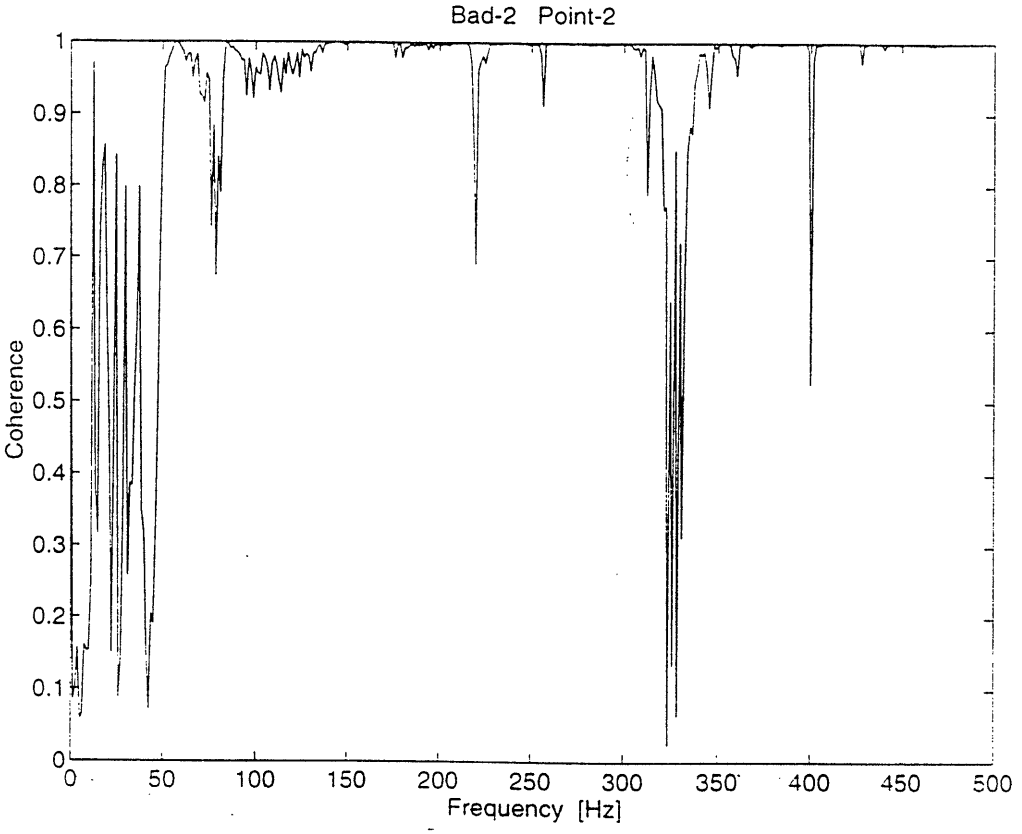

Figure 4.29 Coherence plot of bad-2 point-1 and bad-2 point-2

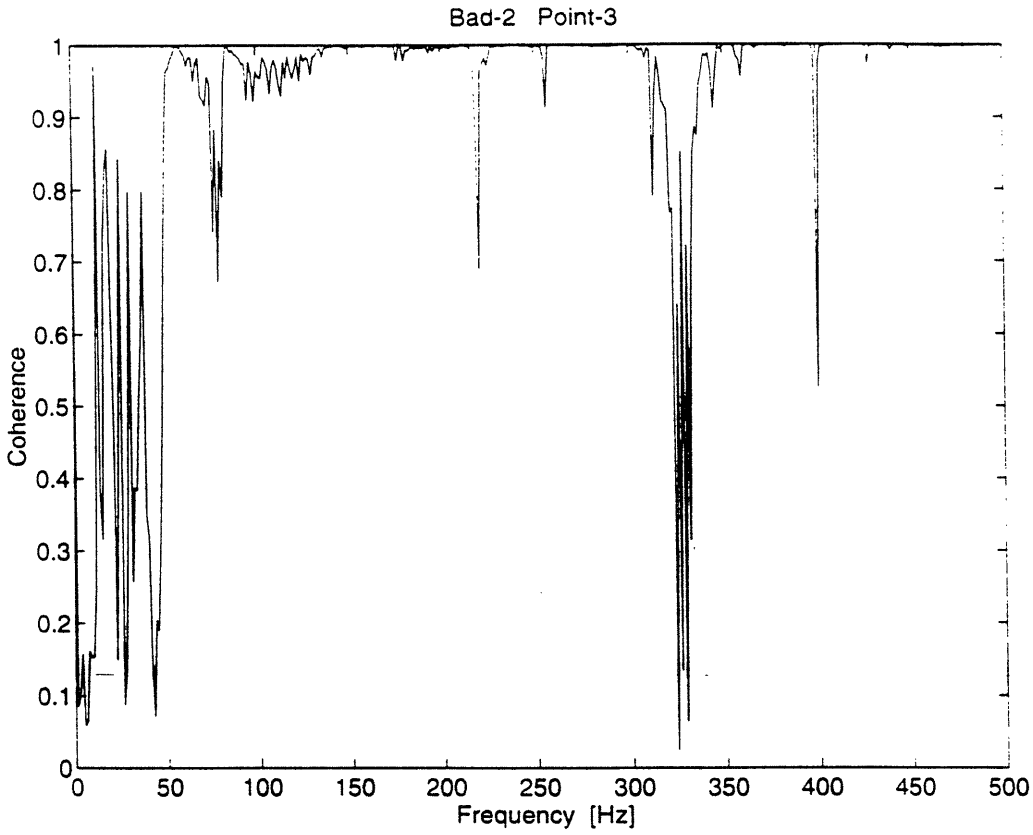

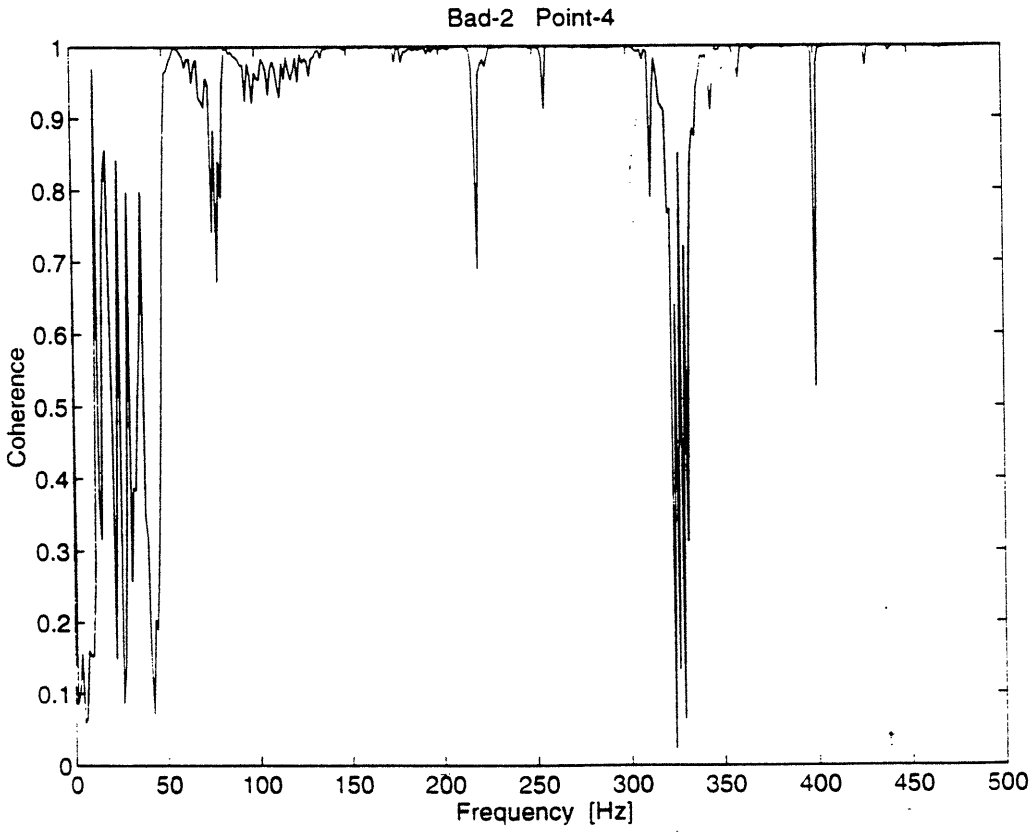

Figure 4.30 Coherence plot of bad-2 point-3 and bad-2 point-4

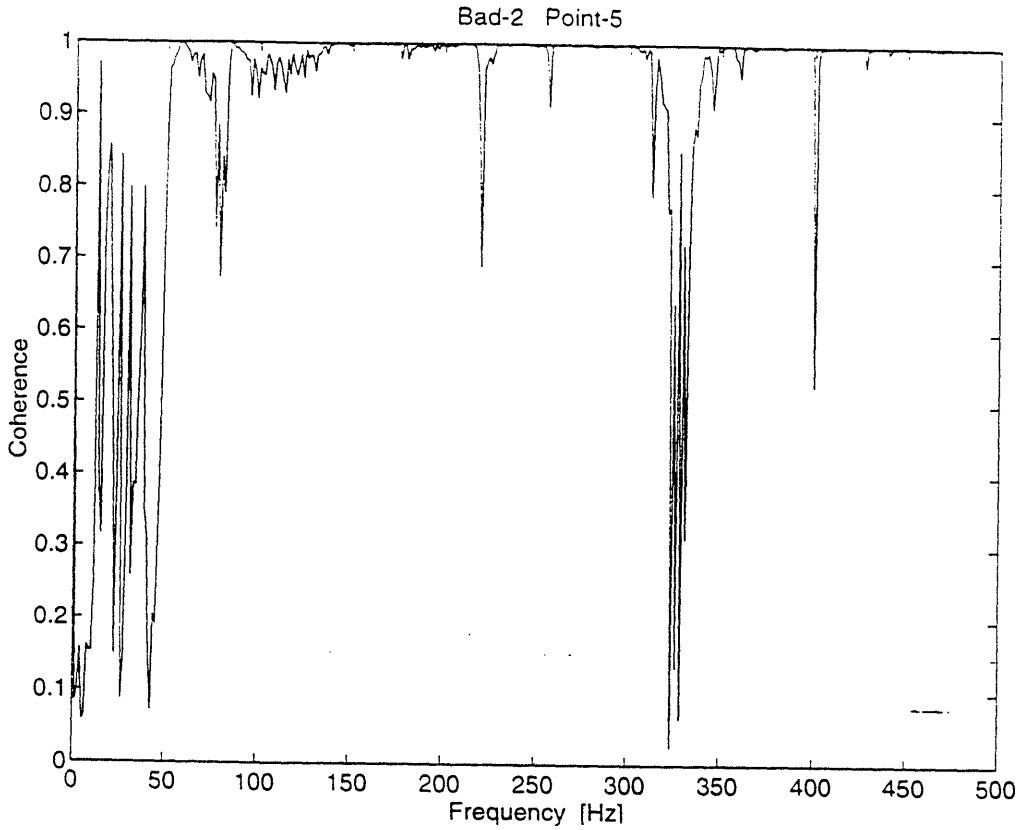

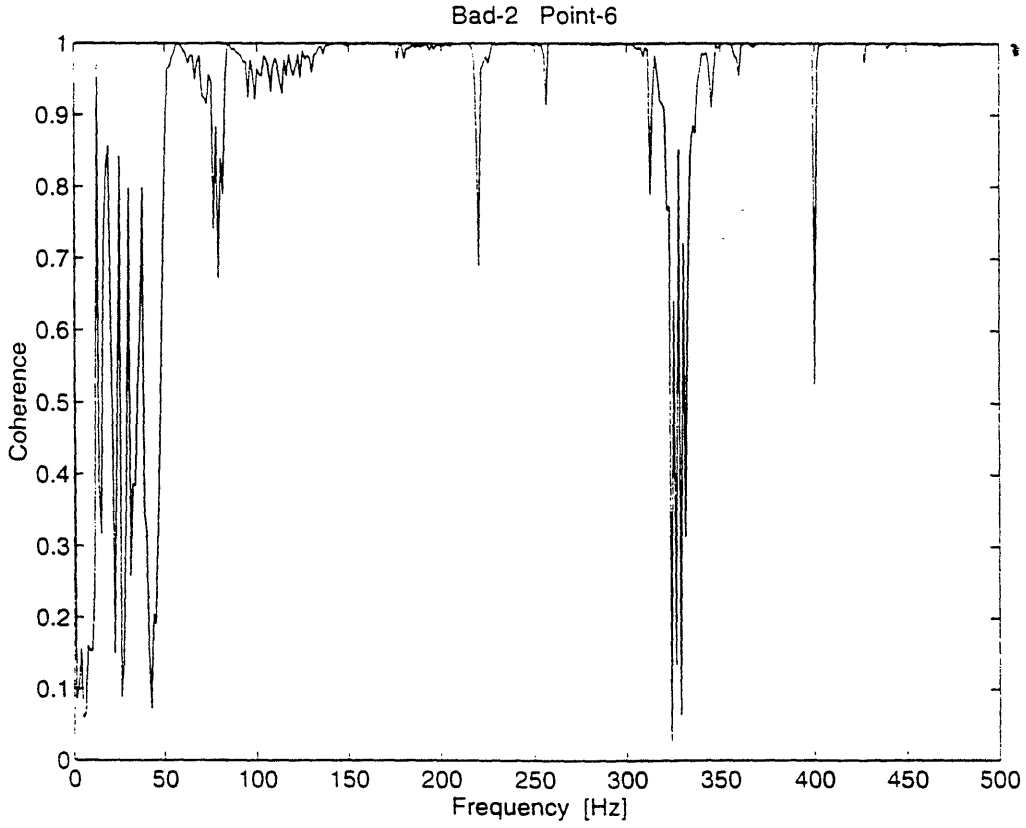

Figure 4.31 Coherence plot of bad-2 point-5 and bad-2 point-6

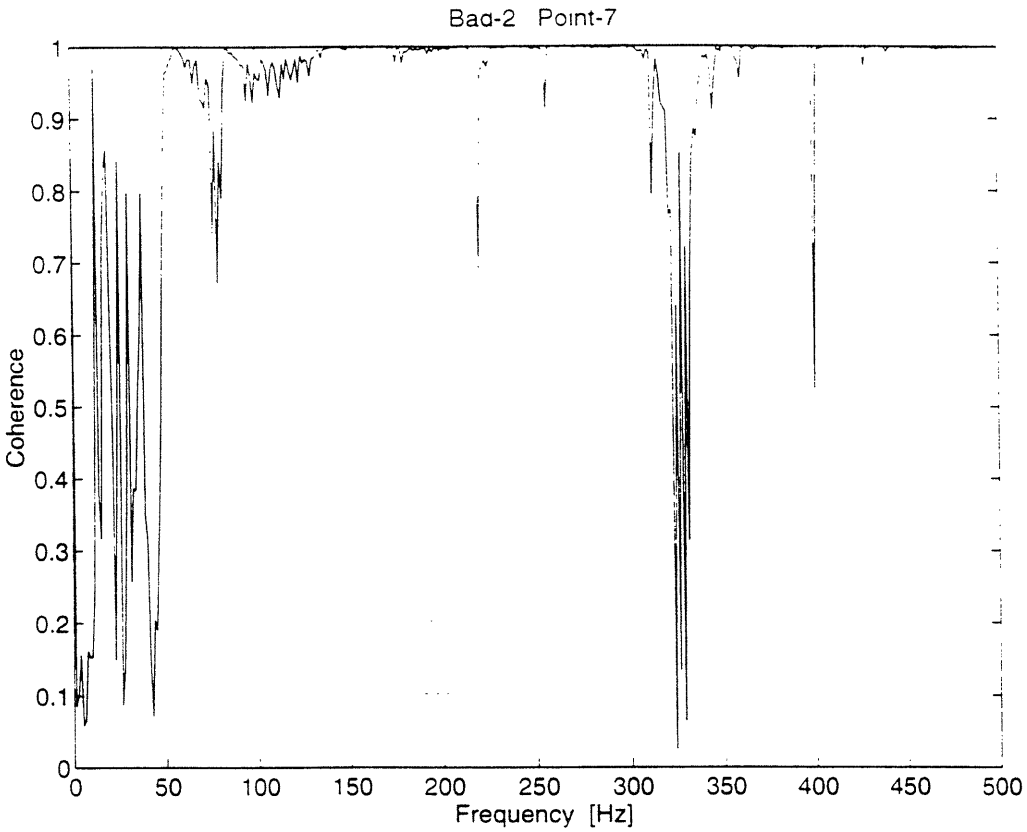

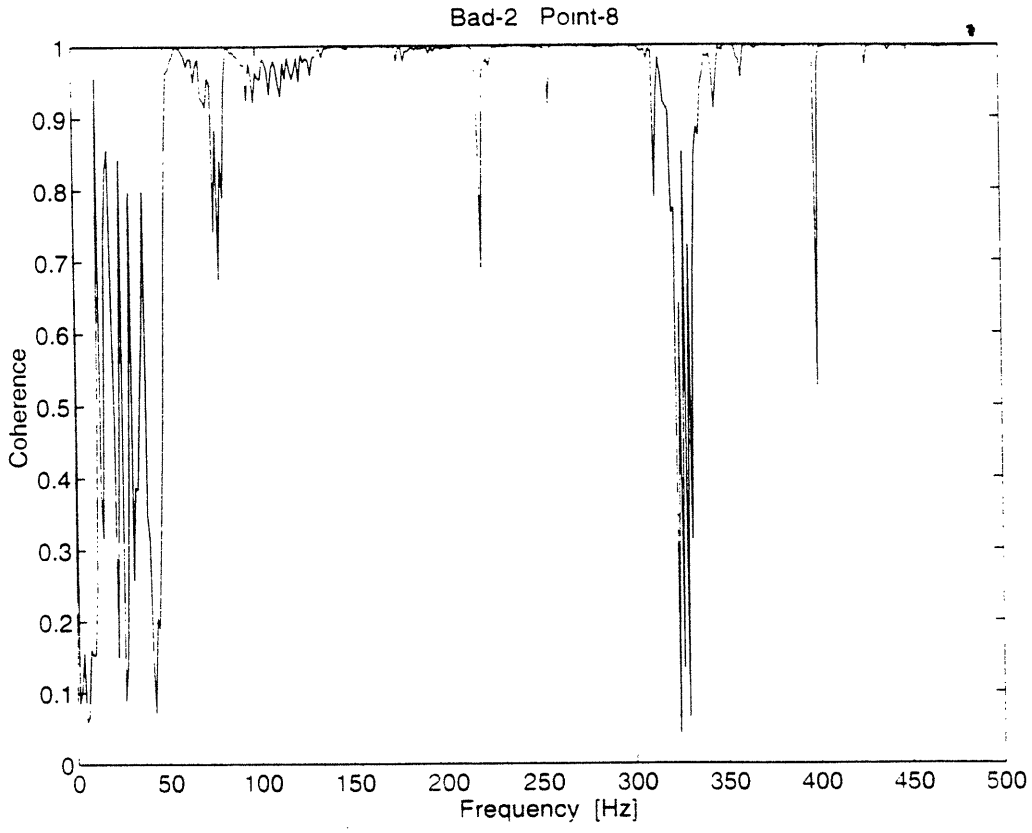

Figure 4.32 Coherence plot of bad-2 point-7 and bad-2 point-8

Chapter 5

Finite Element Analysis of the Test Piece

5.1 Methodology Used in Finite Element Analysis

Analytical study of the test piece is done by the Finite Element Analysis [1] technique. An existing FE model of the test piece, generated by Ford R&D, is used. First of all, the existing model is checked to incorporate the necessary details to represent the hardware properly. Since the test piece is fairly complicated, this step was necessary to gain confidence in the FE results. The FE model has about 9000 elements and each one is about $30mm * 30mm$ in size. Good welds are generated by connecting two nodes as one. Bad welds are modeled by introducing a spring element in between two nodes. The spring constant is set to be $3 * 10^5 N/mm$ for the bad weld. The *bad model* has 7 cold welds out of 80 with $3 * 10^5 N/mm$ as a spring constant and the rest of the welds are modeled as coincident nodes. The spring constant for bad weld $3 * 10^5 N/mm$ is obtained through Ford experiments and is considered to represent the spring constant of a cold weld[2].

The normal modes [3] are calculated on a Convex computer using Nastran FE software. This step is repeated two times, one for the model with 7 good welds and one for the model

[1] FEA
[2] Refer to section 2.1 for the explanation of a cold weld
[3] natural frequencies and mode shapes

with 7 bad welds. The outputs of these two runs were fed to a software called MAC [4] to compare the natural frequencies and mode shapes of the two separate runs.

5.2 Examination of Normal Mode Analysis

Natural frequencies and mode shapes are obtained from normal mode analysis. FEA calculated 35 bending modes in the frequency range of 0-500 Hz as shown in table 5.1. Note that in table 5.1 the 6 rigid body modes which are at 0 Hz aren't listed. The number of bending modes are also calculated analytically to check the FEA results. The test piece is modeled as a simply supported bending plate with surface area A_p and thickness h. Considering the modal density of the two-dimensional bending plate, the equation for the number of bending modes of the plate, which is taken from [11], can be derived. Given the frequency range of interest Δf, the number of bending modes N can be derived as follows :

$$\frac{\Delta f}{N} = \frac{2\kappa c_l}{A_p} \tag{5.1}$$

$$N = \frac{\sqrt{3} A_p \Delta f}{h c_l} \tag{5.2}$$

$$N = 42 \tag{5.3}$$

where,

A_p is the plate surface area : 0.4 m^2

Δf is the frequency range of interest : 0-500 Hz

h is the thickness of the plate : $1.6 * 10^{-3}$ mm

c_l is the longitudinal speed in steel : 5100 m/s

κ is the radius of gyration of the plate : $\frac{h}{2\sqrt{3}}$

The FEA calculation of the number of bending modes was 35 as shown in table 5.1 and the above equation gave 42 for the number of bending modes. They are fairly close to each other. When comparing the two numbers, limitations of the FE meshing has to be kept in

[4] Modal Assurance Criterion

mind. The finer the mesh, the more precise the estimate of the number of modes is, in the limit approaching to the actual number of modes of the test piece. So it is probable that the FEA missed some modes of the test piece, especially the very localized ones which can't be represented by the existing mesh size. As a consequence of this discussion, it is probable that the FEA calculation of the number of modes misses several very localized modes.

Due to complexity of the geometry and the size of the data, a software program, MAC, is used to compare mode shapes and natural frequencies for two separate runs. On the MAC output file as shown in table 5.2, the first two columns represent the bad test piece, called *trial*, and the next two columns represent the good test piece, called *basis*. Comparison of the mode shapes is symbolized by a single number under column *max mac*, which can be either *1* at the most representing identical mode shapes or *0* at the least representing completely different mode shapes. MAC matches the modes of the good and bad test pieces based on the mostly correlated mode shape pairs, not based on the mode sequence. For instance, MAC matches the 10^{th} mode of the good test piece to a specific mode of the bad test piece which gives the highest *max mac* number. As a result of this, the 29^{th} mode of the good test piece may not be matched to the 29^{th} mode of the bad test piece, which is the case in table 5.2.

The last column 2^{nd} *basis* gives the correlation between the *basis* mode and the second most closely correlated mode. It basically tells how unique the match between the *trial* and *basis* modes is. If the 2^{nd} *basis mac* value is close to *0*, the *trial* and *basis* mode match is unique and they don't resemble other modes of the test piece. The *rel phase* column gives the relative phase between the *trial* and *basis* mode shapes and it has very little importance for fault detection purposes. The fifth column demonstrates the Delta_f/f_ave ratio for the *trial* and *basis* modes' natural frequencies. Del_f represents the difference between the *trial* and *basis* modes natural frequencies, whereas the f_ave represents the average of the two natural frequencies. The ratio is an indication of the natural frequency shift of the *trial* mode as compared to the *basis* mode.

Reviewing table 5.2, the shift in natural frequencies of the good and bad test piece is found to be fairly small. The maximum Del_f/f_ave ratio is 4% and appears just once. For

the remaining 34 mode comparisons, the ratio is either 0% or 1%, indicating minute shifts in the natural frequencies of the good and bad test piece. For most of the modes, the shift in natural frequency is less than 3 Hz. There are only four modes which have more than 3 Hz shift in natural frequency: $27^{th}, 29^{th}, 33^{rd}, 35^{th}$ modes of the good test piece. The most drastic change is in the 29^{th} mode of the good test piece. The natural frequency of the 29^{th} mode of the good test piece 417.3 Hz shifted down to 398.9 Hz. Apparently, the 7 cold welds affect the modes around 400 Hz the most. This discovery is an important information to detect the spot-weld defects in the test piece under consideration. As the FE results suggest, any shift in the natural frequencies around 400 Hz can be used to locate the defective spot-weld combination of this research.

On the other hand, this information doesn't offer us clues about which natural frequencies can be affected for some other combination of the spot-weld defects. Another problem is the presence of the *experimental* and *structural variability.* As variability increases, any shift in the natural frequencies of the test pieces due to the fault scrambles with the shift in the natural frequencies due to the overall variability of the test pieces, lowering the detection rate of the fault detection technique. Thus, any successful and reliable fault detection technique has to address above mentioned problems to keep the detection rate high. Referring to figures 3.8 to 3.15, a detectable change in TF at around 400 Hz is noticed. As predicted by the FE results a concentration of resonances around 400 Hz can be seen at almost all the bad pieces, whereas there is relatively less resonant peaks around 400 Hz for the good test piece. But, similar differences also occur at other frequencies and can easily be interpreted as a indication of the fault. Thus, more rigorous understanding and processing of the TF measurements are required.

Another interesting observation is the direction of the natural frequency shifts due to 7 cold welds. All of the natural frequencies of the good test piece shifted *down* in frequency by small amounts. This is also indicated by the positive sign of the Del_f/Ave_f ratio.

The *max mac* value is almost *1* for the unaffected modes, whereas the *max mac* value is lowered considerably for the above mentioned 4 modes, having the minimum value of *0.538* for the 29^{th} mode of the good test piece. As indicated by the table 5.2, all the mode shapes

of the good test piece but four demonstrate very little change due to the 7 cold welds. Note that the 2^{nd} *basis mac* value is almost zero for the unaffected modes, whereas it increases up to *0.403* for the most affected 29^{th} mode. So, the mode shapes of the unaffected modes not only remain almost unchanged, but also preserve their unique shape without resembling any other mode. On the contrary, the mode shape of the affected modes become less distinguishable from the other modes. This information may be useful in the fault detection technique. Actually, the change in mode shapes due to the defect was exploited by some researchers to develop a successful fault detection technique [13,17].

FE results are also useful for checking the experimental results. Comparing theoretical and experimental natural frequencies, one can get a good feel for the reliability of experimental results. So, especially for the global modes, one should observe the peaks in TF magnitude at the calculated natural frequencies, unless the specific measurement point lies on or close to a node line. The first mode is at 57 Hz as calculated by FEA. Reviewing figures 3.8 through 3.15, the first mode is not observed clearly. As explained in section 4.2, the shaker used in the experiment was not capable of supplying enough energy up to about 50 Hz. As a result of this experimental limitation, the first bending mode at 57 Hz couldn't be observed clearly. On the contrary, the second bending mode 76 Hz is very clear in the figures 3.8 through 3.15. The $6^{th}, 8^{th}$ and 9^{th} modes, which are at 126 Hz, 146 Hz and 154 Hz respectively do appear in figures 3.8 through 3.15. Thus, FE results demonstrate good agreement with the measured natural frequencies, increasing the confidence in the experimentation.

But as the test frequency increases, it becomes more cumbersome to compare measured and calculated natural frequencies. Especially the FE meshing of the test piece is an important limitation. As the test frequency increases, finer meshing of the test piece is required to represent the higher frequency modes. Equivalently given the mesh size of the test piece, the FEA results become less reliable as the test frequency is increased.

Modes	Nat'l Freq. of good piece [Hz]	Nat'l Freq. of bad piece [Hz]
1^{th} mode	57	57
2^{th} mode	76	76
3^{th} mode	95	94
4^{th} mode	111	110
5^{st} mode	115	115
6^{nd} mode	127	127
7^{rd} mode	136	136
8^{th} mode	147	147
9^{th} mode	155	154
10^{th} mode	169	169
11^{th} mode	181	181
12^{th} mode	190	189
13^{th} mode	196	195
14^{th} mode	198	198
15^{st} mode	206	204
16^{nd} mode	226	225
17^{rd} mode	251	251
18^{th} mode	253	253
19^{th} mode	264	263
20^{th} mode	268	268
21^{th} mode	281	280
22^{th} mode	297	296
23^{th} mode	312	312
24^{th} mode	324	324
25^{st} mode	334	330
26^{nd} mode	362	359
27^{rd} mode	392	383
28^{th} mode	408	399
29^{th} mode	417	408
30^{th} mode	428	427
31^{th} mode	444	441
32^{th} mode	459	457
33^{th} mode	472	461
34^{th} mode	476	473
35^{th} mode	493	487

Table 5.1 Results of Normal Mode Analysis for three runs

Geometry Correlation

COMP. OF MUSTANG REV BASELINE LATEST - NORMAL MODE ANALYSI
MODEL ANALYSIS OF NEW DYNAMIC TESTING-LANCZOS METHOD.

NOV 3, 1993 -CONVEX

COMP. OF MUSTANG REV BASELINE WITH 7 COLD WELDS - NORMAL M
MODEL ANALYSIS OF NEW DYNAMIC TESTING-LANCZOS METHOD.

NOV 3, 1993 -CONVEX

TRIAL index	TRIAL id	BASIS index	BASIS id	minimum distance	
1	205	1	205	0.00e+00	SELECTED : biggest distance

---TRIAL V-- MODE#	FREQ	---BASIS V-- MODE#	FREQ	Del_f/ Ave_f	MAX MAC	|BV|**2/ |TV|**2	REL. PHASE	-2nd-BASIS MODE#	MAC
1	57.1	1	57.3	0.00	1.000	1.00e+00	0.0	2	0.044
2	75.9	2	76.0	0.00	1.000	1.00e+00	180.0	1	0.046
3	94.3	3	95.0	0.01	0.999	9.95e-01	0.0	2	0.027
4	110.3	4	111.2	0.01	0.994	9.90e-01	0.0	5	0.018
5	114.7	5	115.2	0.00	0.994	1.01e+00	0.0	6	0.025
6	126.6	6	126.8	0.00	0.999	1.03e+00	180.0	7	0.262
7	135.5	7	135.7	0.00	0.999	9.78e-01	180.0	6	0.298
8	146.6	8	146.6	0.00	1.000	1.00e+00	0.0	10	0.007
9	153.9	9	154.6	0.00	0.999	9.98e-01	180.0	6	0.046
10	168.6	10	168.8	0.00	1.000	1.00e+00	0.0	8	0.008
11	180.8	11	181.4	0.00	0.998	9.97e-01	0.0	15	0.013
12	189.3	12	190.0	0.00	0.992	9.96e-01	180.0	9	0.012
13	194.9	13	196.1	0.01	0.972	9.98e-01	0.0	14	0.037
14	197.9	14	198.4	0.00	0.972	1.01e+00	180.0	11	0.017
15	204.3	15	206.2	0.01	0.995	1.01e+00	180.0	11	0.003
16	225.2	16	225.5	0.00	1.000	1.00e+00	0.0	21	0.023
17	250.8	17	250.9	0.00	1.000	1.00e+00	0.0	18	0.006
18	252.9	18	252.9	0.00	1.000	9.98e-01	0.0	17	0.008
19	263.1	19	263.6	0.00	0.997	1.02e+00	0.0	20	0.068
20	267.7	20	267.7	0.00	1.000	9.91e-01	180.0	19	0.098
21	280.4	21	281.2	0.00	0.999	9.94e-01	0.0	16	0.025
22	296.4	22	297.2	0.00	0.999	1.00e+00	180.0	20	0.015
23	311.7	23	312.1	0.00	0.998	9.85e-01	180.0	24	0.052
24	323.7	24	324.2	0.00	0.997	1.01e+00	180.0	23	0.028
25	330.4	25	333.5	0.01	0.987	9.59e-01	180.0	26	0.091
26	359.1	26	361.6	0.01	0.989	1.05e+00	180.0	30	0.052
27	383.3	27	391.7	0.02	0.701	1.16e+00	180.0	30	0.062
28	398.9	29	417.3	0.04	0.538	1.06e+00	0.0	27	0.403
29	408.3	28	407.5	0.00	0.887	8.92e-01	0.0	29	0.270
30	427.0	30	428.0	0.00	0.957	9.46e-01	180.0	29	0.138
31	441.3	31	444.0	0.01	0.940	9.64e-01	180.0	35	0.057
32	457.3	32	458.6	0.00	0.932	1.03e+00	0.0	34	0.179
33	461.2	33	471.9	0.02	0.396	2.17e+00	180.0	32	0.119
34	473.4	33	471.9	0.00	0.765	1.07e+00	180.0	34	0.409
35	486.8	35	493.0	0.01	0.879	8.68e-01	0.0	33	0.296

Table 5.2 MAC output for good piece and bad piece

Chapter 6

Fault Detection and Feature Selection

The key goal in fault diagnosis is to find a feature which will reveal the fault at once, while suppressing the variations which occur during the operation of the machine. As discussed earlier, nominally identical structures don't have identical vibration characteristics [1]. Additionally, experimental variation, such as the impulse response truncation, is another source of variability.

Consequently, any fault detection method should suppress these variations whilst preserving the changes caused by the fault. Having defined the problem, it reduces to finding a suitable domain [2], such as TF magnitude, TF phase etc., and a suitable fault detection method, which will reveal the fault.

6.1 Feature Selection

To increase diagnosibility, a proper feature satisfying the above requirements should be selected. This will not only increase diagnosibility but also decrease the number of measurements. Any output signal measured at the surface of the structure contains information about both the input signal and the structure itself. Consequently, the measured output

[1] Refer to chapter 3

[2] The domain will be referred to as *feature* in this chapter

signal contains information about any fault in the structure. When the fault is a minute one such as the spot-weld defect, any change in the output signal due to the fault becomes less detectable. Furthermore, taking the changes in the output signal due to the *experimental variability* and *structural variability* [3] into account, the detection of fault signature becomes more problematic. Actually the experiments showed the *structural* and *experimental variability* are dominant over the fault signature due to several faulty spot-welds. As explained in chapters 2 and 3, the *experimental* and *structural variability* constitutes big portion of the signature change in the output signal. Thus, the fault signature gets buried in the output signal change due to the *experimental* and *structural variability.*

Another consideration is the attenuation of the fault signature on its way to the accelerometer. The fault signature which is already difficult to detect attenuates due to structural damping and measurement noise. So in practice, it is advantageous to locate the accelerometer in the vicinity of the fault. On the other hand, approximate fault location is generally unknown.

So any fault detection technique has to address above mentioned problems in order to detect faults successfully. The fault detection technique is nothing but the fault detection strategy. Beside a powerful fault detection technique, a feature which reduces the adverse effects of *experimental* and *structural variability* is necessary too. Moreover, the quantitative formulation of the problem is helpful in deciding the most suitable feature and the fault detection technique among many possible selections. Such a quantitative formulation may also give insight to the physics of the problem, revealing which features are affected the most due to the fault.

6.1.1 Separability Measure and Confidence Level

At this point of the discussion, it is necessary to formulate the problem of optimum feature selection, or at least obtain an analytical feel for different features' conformity with requirements. For each feature, the degree of separability of two different fault cases is a function of the distance between two measurements, the good test piece and the bad test piece.

[3] Refer to chapter 2 and chapter 3 for detailed discussion

Refer to figure 6.1 to visualize the idea. As the distance between the two measurements increases the probability of correct diagnosis increases. Ideally, every good test piece has to be represented by a single curve and the same should hold true for the bad test piece. But in practice, the good and the bad test pieces form a set of curves around a mean due to the *experimental* and *structural variability.* Thus, in order to increase diagnosibility, the distance between the good and bad test piece has to be as much as possible and features with high separability have to be selected. The formulation is simply,

$$d(k,l) = \sqrt{\sum_{i=1}^{M}(x_{ik} - x_{il})^2} \tag{6.1}$$

where,

k represents the curve for the good test piece,

l represents the curve for the bad test piece,

M represents the number of discrete samples,

x_{ik} represents each element of recognition matrix,

$\tau = (x_{ik} - x_{il})$ is the normalized distance between two curves at the i^{th} discrete sample,

$d(k,l)$ represents separability measure.

Figure 6.1 illustrates the idea.

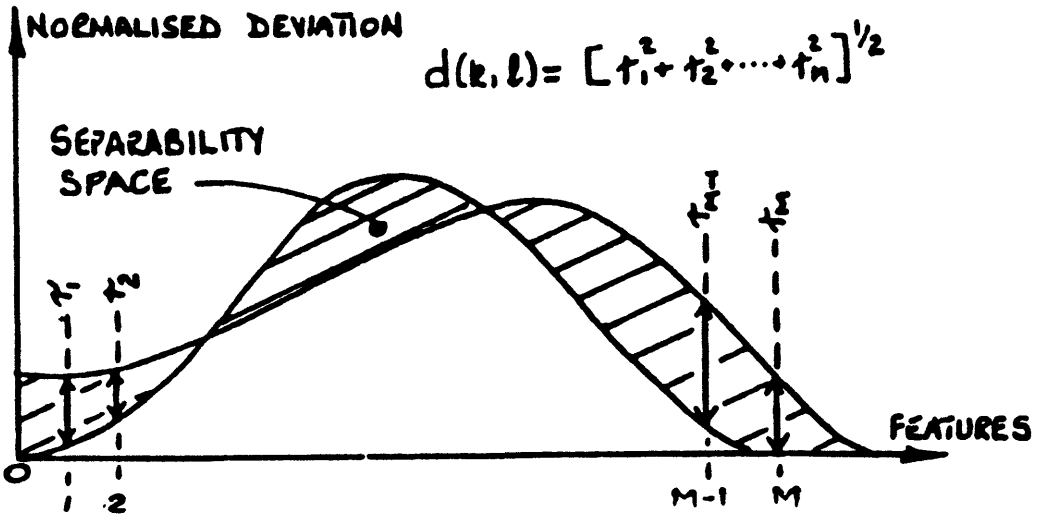

Figure 6.1 Separability Space

Furthermore, the formulation can be improved to incorporate the inherent variability of non-faulty components. A measure to judge the merit of a set of features is required. Confidence level serves to this purpose. By means of calculating confidence level of each feature, it becomes possible to select the feature which satisfies the above mentioned diagnosis requirements the most. Confidence level calculation basically relies on the separability measure, equation 6.1. In addition, an algorithm that accounts for the *inherent structural* and *experimental variability* is added. For each feature, separability measure and percent separability measure are calculated. A confidence level of *1* is assigned to the measurements with percent separability measure of 50% or more. Measurements with percent separability measure less than 50% retain their value. Then, the overall percentage of confidence level becomes,

$$C = [\frac{C1 + C2}{\frac{N(N-1)}{2}}] * 100 \tag{6.2}$$

where,

N is the number of distinctive fault cases,

C1 and C2 are intermediate variables in the confidence level calculation, as shown in figure 6.2.

In this research there are only the good test piece and the bad test piece. So $N = 2$ as far as this research is concerned. 50% represents the margin of separability measure and basically accounts for the overall variability in the measurement and structure. Confidence level of a set of features can be increased by lowering the 50% requirement, but this will increase the adverse effect of variations in non-faulty parts. The flow-chart of the computer program written to test the confidence level of different features is shown in figure 6.2. The confidence levels obtained for different sets of features are presented in tables 6.1 through 6.4. Thus, given the margin of separability measure, confidence level indicates the degree of the feature's conformity with the fault detection requirements. Confidence level of a feature can vary between *0* and *1*. Given the margin of separability measure, *0* indicates exact similarity between the two distinct faults under consideration [4], whereas *1* indicates

[4] In this research the two distinct faults correspond to the good test piece and the bad test piece

maximum possible distance [5] between the two distinct faults under consideration, the good test piece and the bad test piece.

6.2 Fault Detection Technique

Having decided on the suitable feature based on the confidence levels, a suitable fault detection technique is to be established. But the key step is to pick a simple yet effective scheme, since the fault detection technique has to provide quick and reliable answers.

6.2.1 The Recognition Matrix

In order to formulate the problem of optimum fault detection technique selection, a mathematical tool is used. All samples representative of distinct faults are arranged into a matrix called the *recognition matrix*. A sample recognition matrix is shown in figure 6.3. Each row of the recognition matrix contains samples of the selected feature for each fault case. The number of samples determine the number of columns of a recognition matrix, whereas the number of simulated distinct faults determines the number of rows in the recognition matrix. Note that each row entry is a representative of a certain distinct fault. In order to reduce variability, the mean of each distinct fault is entered into the recognition matrix.

In this research, there are two simulated distinct fault cases, one of them being the good test piece, the other being the bad test piece. The mean of 9 identical test pieces is entered into the recognition matrix. The same is done for the bad test pieces. Note that the two good test pieces, which are out-of-population [6] are not included in the recognition matrix. The 9 good test pieces and 9 bad test piece are specially manufactured and have less structural variability than the test pieces manufactured at the plant. So the two out-of-population test pieces are tested against the recognition matrix to judge the applicability of the fault detection technique to real life production.

[5] Refer to figure 6.1 to visualize the distance between the two distinct faults
[6] Refer to section 2.1 for detailed explanation of the out-of-population test pieces

The next step is to simulate different possible faults and enter the samples of the selected feature into the recognition matrix. This step should be carried out in the laboratory. Given the knowledge of the most common faults occurring during the process, the test pieces with predetermined faults have to be manufactured and measurements have to be stored in the recognition matrix. This recognition matrix will form the basis for fault detection. Irrespective of consistency and reliability of the selected feature and the fault detection technique, the fault diagnosis will be as good as the recognition matrix. If the recognition matrix entries don't represent the common faults, the fault detection technique can't detect faults efficiently.

Once a recognition matrix of a certain test piece is available, the task reduces to the comparison of the recognition matrix with response data obtained from the test pieces. The aim is to describe the probable defects present in the test piece.

The technique used in this research does not look for an exact match between the recognition matrix entries and the sample measurement. It tries to find the closest recognition matrix entry. As a result, the most likely fault is detected. A list of the possible defects can be prepared among the simulated faults which are already stored in the recognition matrix in order of decreasing likelihood.

The mathematical formulation is as follows :

$$F_j = \sum_{i=1}^{M} x_{ij} y_i \qquad j = 1, 2, ...N \tag{6.3}$$

where,

i indicates number of discrete samples, there are M of them in total,

j indicates the number of distinct faults, there are N of them in total,

x_{ij} indicates each element of recognition matrix ,

y_i indicates the discrete samples of the test piece to be diagnosed.

F_j indicates the correlation coefficient between the j^{th} row of recognition matrix and the discrete samples of the test piece to be diagnosed y_i where i = 1..M

$$\tau_2 = -\frac{\phi(n) - \phi(n-2)}{2\Delta w} \tag{6.5}$$

Then, to eliminate the problems related to impulse response truncation, exponential windowing is applied to the original data. The same features are tried for exponentially windowed data. In addition, the minimum phase part and all-pass part decomposition is carried out. The same features of the minimum phase and all-pass part are fed to the calculation scheme. The minimum phase part of the signal eliminates problems related to *non-minimum phase zero shifts* [5], whereas all-pass part incorporates *non-minimum phase zero shifts* and reverberation in the structure [7,15]. Although these are not the only characteristics of the minimum phase and the all-pass part of a signal, these are the ones of concern to us.

Examining the tables 6.1 through 6.4, the TF magnitude is observed to have a relatively high confidence level both for the original and windowed data. There are 12 misjudged measurement points for the original data and 24 for the windowed data out of 160 measurement points. Today, most of the commercially available fault diagnosis techniques make use of the TF magnitude, but in a different way. On the other hand, group delay and group delay-2 [9] prove to be much better than the TF magnitude. In general, group delay seems to be better than the rest of the features. All group delay calculations give the same satisfactory result, but group delay of the original data failed in only 2 points out of 160, which is the best result among of all the features. Another thing to notice is the improvement obtained by eliminating low frequency data which has low coherence. This is represented by (125:500) in the tables 6.1 through 6.4. The rationale for eliminating the low frequency data and the adverse effects of low coherence at low frequencies has already been explained in section 4.2.

As mentioned above, 144 measurement points out of 160 measurement points belong to test pieces manufactured under controlled manufacturing environment. In real life, subassemblies do have larger structural variability. So it is a question whether the recognition matrix formed from specially manufactured test pieces will work for the real life subassem-

[9] group delay calculated according to equation 6.5

The above calculation is done for each recognition matrix row [7]. The outcome is N number of F_j values. The largest F_j value, F_J indicates that the test piece which is to be diagnosed is the most highly correlated to that specific row, indicating that the possible fault of the test piece is the J^{th} fault. The computation is straightforward and takes little time.

6.3 Discussion of Experimental Results

Having explained the logic behind feature selection and fault detection technique, we move onto the application of these concepts to the experimental data collected. The first step is to find the confidence level of possible features in order to decide on one of them. Then, the fault detection technique is applied.

On each of the 20 test pieces[8], there are 8 measurement points. This makes 160 total measurement points, which implies that the fault detection technique can be tested 160 times. The confidence level of each feature and the number of misjudged measurement points are listed in Tables 6.1 through 6.4. To eliminate problems due to low coherence at low frequencies, frequency samples below 125 Hz are rejected and this is, in some sense, equivalent to coherence weighting. Referring to figures 4.25 through 4.32, the low coherence at low frequencies can be observed.

Firstly, the original data is fed into the calculation scheme. Different features such as impulse response, TF magnitude, TF phase, group delay etc. are tried. Group delay is defined to be the frequency derivative of the unwrapped phase. Numerically,

$$\tau = -\frac{\phi(n) - \phi(n-1)}{\Delta w} \tag{6.4}$$

For noisy systems, it is recommended to use [12],

[7] ie. for each distinct fault
[8] including the 2 out-of population test pieces

blies, which have higher variability. The two out-of-population test pieces are useful for checking this. Results show that features like group delay and group delay-2 are found to be successful in detecting the two out-of-population test pieces. The two out-of-population good test pieces are judged to be good by group delay, group delay-2 and by some other features.

Moreover, all but one of the 8 measurement points on each test piece are far away from the defective spot-welds. Intuitively, the change in the vibration signal due the defect attenuates on the way to the measurement point. So the feature must be capable of detecting the attenuated signal change due to the defect. On the other hand, in real life applications, it is unlikely that the transducer will be placed right next to the defect. So, any successful feature must minimize the stated problem. Group delay seems to satisfy the requirement best.

As defined in this section, group delay is the first derivative of the unwrapped phase. Basically, group delay tells about the reverberations in the structure. It is known that the defect changes the stiffness matrix the most [13]. On the other hand, the experimental data at hand aren't enough to bring a crystal-clear explanation to the question of why the group delay is the best feature to diagnose the test piece. The explanation may be related to the change of reverberations in the presence of the fault. The reverberations, which are small fluctuations superposed on π shifts of unwrapped phase may be the indication of structural changes in the test piece.

original data	Confidence Level	# of misjudged pts out of 160
TF magnitude	0.62	12
TF magnitude (125:500)	0.63	11
Wrapped phase	1	35
Wrapped phase (125:500)	1	36
Unwrapped phase	0.04	73
Unwrapped phase (125:500)	0.04	59
Group delay	1	7
Group delay (125:500)	1	2
Group delay-2	0.99	8
Group delay-2 (125:500)	1	3
Impulse Response	1	35

Table 6.1 Number of misjudged points for original data

win'd data	Confidence Level	# of misjudged pts out of 160
TF magnitude	0.49	24
TF magnitude (125:500)	0.50	12
Wrapped phase	0.59	28
Wrapped phase (125:500)	0.93	29
Unwrapped phase	0.03	70
Group delay	0.78	5
Group delay (125:500)	0.93	4
Group delay-2	0.74	9
Group delay-2 (125:500)	0.89	9
Impulse Response	0.93	35

Table 6.2 Number of misjudged points for exponentially windowed data

min ph part of win'd data	Confidence Level	# of misjudged pts out of 160
TF magnitude	0.49	24
TF magnitude (125:500)	0.50	24
Wrapped phase	0.61	22
Wrapped phase (125:500)	0.71	22
Unwrapped phase	0.52	29
Unwrapped phase (125:500)	0.59	29
Group delay	1	6
Group delay (125:500)	1	3
Group delay-2	1	8
Group delay-2 (125:500)	1	6
Impulse Response	0.75	33

Table 6.3 Number of misjudged points for minimum phase part of exponentially windowed data

all-pass part of win'd data	Confidence Level	# of misjudged pts out of 160
Wrapped phase	1	58
Wrapped phase (125:500)	1	56
Unwrapped phase	0.14	82
Group delay	0.85	35
Group delay (125:500)	1	32
Group delay-2	0.83	38
Group delay-2 (125:500)	0.94	30

Table 6.4 Number of misjudged points for all-pass part of exponentially windowed data

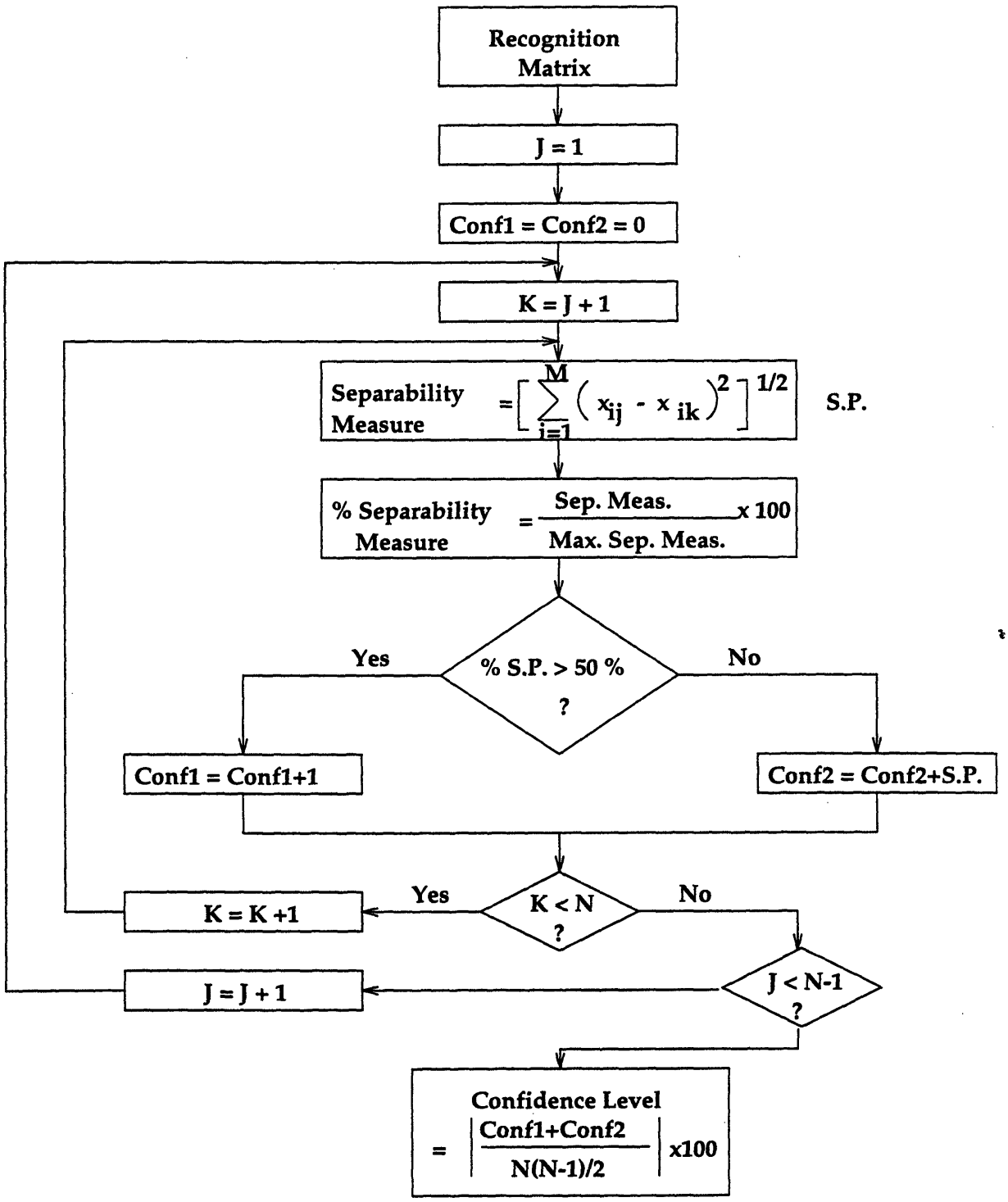

Figure 6.2 Flow-chart of *confidence level* program

$$R = \begin{pmatrix} x_{11} & x_{12} & x_{13} & x_{14} & \cdots & x_{1M} \\ x_{21} & x_{22} & x_{23} & x_{24} & \cdots & x_{2M} \\ x_{31} & x_{32} & x_{33} & x_{34} & \cdots & x_{3M} \\ x_{41} & x_{42} & x_{43} & x_{44} & \cdots & x_{4M} \\ \vdots & \vdots & \vdots & \vdots & \ddots & \vdots \\ \vdots & \vdots & \vdots & \vdots & \ddots & \vdots \\ x_{N1} & x_{N2} & x_{N3} & x_{N4} & \cdots & x_{NM} \end{pmatrix}$$

where,

N is the number of distinct faults

M is the number of discrete samples

Figure 6.3 The Recognition Matrix

Chapter 7

Conclusion

One of the aims of this research was to understand the nature of the structural variability phenomena and ways to minimize its adverse effect on the structural fault detection and inverse filtering methods. After completing this step, a structural fault detection method was developed to monitor the spot-weld defects of car body structure. From the results presented, the following conclusions can be drawn.

The experimentation and the design of certain instruments have considerable contribution to the overall variability of the transfer function. Experiments proved that certain parameters such as proper shaker attachment and design of the stinger are essential to minimize the *experimental variability.*

The measured structural variability of the good and bad test pieces were found to be considerably high despite all efforts to reduce the overall variability of the structure. Apparently, the measured variability is mainly due to the structural differences among the nominally identical test pieces. The transfer function is found to be sensitive to small changes in the structure. This feature of the TF is a disadvantage for fault diagnosis. Any successful fault detection technique has to reduce the *inherent structural variability* via proper processing of the TF measurements. Recall that several research efforts arrive at the same conclusion as it was discussed in section 3.1.

The careful analysis of the transfer function revealed that even the signal processing

scheme can introduce some amount of error in the transfer function measurements, especially in the total accumulated phase of the structure. The time record of the measurement should be long enough to capture the whole impulse response of the structure. Otherwise, the impulse response truncation effect artificially increases the total accumulated phase of the structure.

Comparison of natural frequencies obtained from the FEA and experimentation very well matched especially below 300 Hz, demonstrating the reliability of the TF measurements. FEA results indicated that the spot-weld defects under consideration affected the modes around 400 Hz, especially the 29^{th} mode of the good test piece. Only 4 modes were found to be affected by the spot-weld defect, whereas the remaining 31 modes' natural frequencies and mode shapes didn't change significantly. This piece of information about the spot-weld defect's effect on the test piece can be used to diagnose the spot-weld defects. On the other hand, the TF measurements showed that the overall variability of the test piece veils the effect of spot-weld defect on the TF, lowering the detection rate.

A structural fault detection technique based on the recognition matrix method is developed to address the variability problem, while maintaining a high detection rate. The recognition matrix technique failed only in 2 measurement points out of 160 when group delay is used as a feature. The developed method overcame the structural variability problem for the two distinct test piece case, namely the good test piece and bad test piece.

The physical interpretation of group delay's superiority over the other tried features hasn't been understood thoroughly. The explanation may be related to the sensitivity of reverberations to the changes in the spot-weld quality. But there aren't enough experiment data to give a complete physical interpretation of group delay's superiority over the other tried features.

7.1 Suggested Further Research

The recognition matrix technique worked for the two distinct test piece case. But in practice, there are many possible faults.

Taking manufacturer's recommendations on common faults, a new experiment with more distinct faults has to be carried out. For instance, 5 distinct faults can be simulated. This requires 50 test pieces. Once this proposed experiment is successfully completed, the effectiveness of the recognition matrix method in practice can be assessed more thoroughly.

Additional experiments should be carried out to understand the group delay's superiority as a feature. The physical interpretation as well as the possible applications of group delay should be investigated. The more we learn about the structural changes the fault causes, the better and more reliable fault detection algorithms we can develop.

References

[1] - D. J. Ewins, J. Griffin, "A state-of-the-art Assessment of Mobility Measurement Techniques", J. Sound & Vibr., 78(2), 1981

[2] - D. J. Ewins, " Modal Testing : Theory and Practice ", Research Studies Press, 1984

[3] - D. E. Newland, " An Introduction to Random Vibrations and Spectral Analysis ", Longman Group Limited, 1984

[4] - R. G. Gibson, " Phase Variability of Structural Transfer Functions ",M. Sc. thesis, MIT, Dept. of Mech. Eng., 1986

[5] - D. J. McCarthy and H. A. Gaberson, " Condition Monitoring and Diagnostics of a Reciprocating Compressor ", MFPG 47, April,1993

[6] - M. S. Kampella and R. J. Bernhard, " Measurement of Statistical Variation of Structural-acoustic Characteristics of Automotive Vehicles ", Purdue University, Internal-200, March 1993

[7] - R. H. Lyon, " Diagnostic Signature Recovery in Reverberant Systems ", Korea-US Vibration Symposium, March 1993

[8] - D. Boulahbal, " Investigations on Group Delay in Structures and Acoustical Spaces", M. Sc. thesis, MIT, Dept. of Mech. Eng., 1988

[9] - M. Tohyama, R. H. Lyon, " Transfer Function Phase and Truncated Impulse Response ", J. Acoust. Soc. Am. 86(5), Nov. 1989

[10] - G. C. Strang, " Introduction to Applied Mathematics ", Wellesley-Cambridge Press, 1986.

[11] - R. H. Lyon, " Machinery Noise and Diagnostics ", Butterworth Publishing, 1987

[12] - M. Tohyama, R. H. Lyon, T. Koike, " Phase Variabilities and Zeros in a Reverberant Transfer Function ", J. Acoust. Soc. Am.

[13] - M. H. Richardson, " Using Modal Parameters for On-line Structural Fault Detection ", Korea-US Vibration Symposium, March 1993

[14] - G. M. Hieber, " Non-Toxic Stingers ", Proc. of 6^{th} International Modal Analysis Con., 1988

[15] - M. Tohyama, R. H. Lyon, T. Koike, " Inverse Filtering for Reverberant Transfer Functions ", IUTAM Meeting, May 1992

[16] - M. Murville, " The Design of a Robust Inverse Filter for High Level Diagnostics ",M. Sc. thesis, MIT, Dept. of Mech. Eng., 1984

[17] - F. Shahrivar, J. G. Bouwkamp, "Damage Detection in Offshore Platforms Using Vibration Information", J. Energy Resources Technology, 108/97, June 1986

[18] - Unpublished data taken on 40 hp Ingersall Rand reciprocating compressor at MIT

[19] - S. Haran, S. M. Rocha, R. D. Finch, "Evaluation of a Prototype Acoustic Signature Inspection System Railroad Wheels", Federal Railroad Administration Office of Research and Development, FRA/ORD - 84/19, May 1985

3090-24